Simulating the field-line random walk process

JVA Joubert

orcid.org 0009-0000-6881-4420

Dissertation accepted in partial fulfilment of the requirements for the degree *Master of Science in Astrophysical Sciences* at the North-West University

Supervisor: Prof RDT Strauss

Co-supervisor: Dr J Light

Graduation: November 2025

From here it's, um... left.
Oh, no. No, it's to the right. My mistake.
No! No, no, no! Not the right!
Why would I have ever said it was to the right?
What was I thinking?

∼The narrator,
The Stanley Parable

Abstract

The nature and structure of the heliospheric magnetic field play an important role in the transport of energetic particles throughout the heliosphere. In order to further knowledge about turbulence-particle interactions, especially the diffusive motion of charged particles perpendicular to the mean field, a greater understanding of the field-line random walk process is needed. This study summarises the fundamental physics encapsulating the meandering of magnetic field-lines due to turbulence within the solar wind, and develops a numerical model with which to simulate the turbulent heliospheric magnetic field. This is done by employing stochastic differential equations to numerically solve the convection-diffusion equation for field-line diffusion, which is derived from the focused transport equation for particles. Assuming purely 2D turbulence and adopting turbulence quantities derived from observations, the numerical model is applied to the Parker heliospheric magnetic field. The model results show a probability distribution possessing a near-Gaussian shape, which is narrower when close to the Sun and grows wider with the increase in radial distance. The most likely path of the heliospheric magnetic field is calculated from the probability distribution for different field-line diffusion coefficients. Comparing the model results with the turbulence-free Parker heliospheric magnetic field shows that the calculated most likely paths are similar to the turbulence-free Parker heliospheric magnetic field model for smaller diffusion coefficients, while becoming more underwound as the diffusion coefficient increases. This corresponds well with recent observations.

Keywords: field-line diffusion; heliospheric magnetic field; turbulence; numerical methods; stochastic differential equations.

Opsomming

Die aard en struktuur van die heliosferiese magneetveld speel 'n belangrike rol in die transport van energieke deeltjies regdeur die heliosfeer. Om kennis rakende turbulensie-deeltjie interaksies, veral die diffusiewe beweeging van gelaaide deeltjies loodreg tot die gemiddelde veld, te bevorder, is 'n beter begrip van die ewekansige loop van veldlyne benodig. Hierdie studie som die fundamentele fisika op wat die lukrake wandel van magneetveldlyne as gevolg van die turbulente sonwind saamvat en ontwikkel 'n numeriese model om die turbulente heliosferiese magneetveld te simuleer. Hierdie word gedoen deur gebruik te maak van stogastiese differensiaal-vergelykings om die konveksie-diffusie vergelyking vir veldlyne, afgelei vanaf die gefokusde transport-vergelyking vir deeltjies, numeries op te los. Die numeriese model word dan toegepas op die Parker heliosferiese magneetveld deur aan te neem dat die turbulensie slegs 2D is, en deur turbulensie waardes afgelei vanaf waarnemings te gebruik. Die resultate toon 'n waarskynlikheidsverdeling met 'n amper-Gaussiese vorm, wat nouer is vir klein radiale afstande vanaf die Son, en wat wyer word namate die radiale afstand toeneem. Vanaf die waarskynlikheidsverdeling word die mees waarskynlike pad wat die magneetveldlyn sou volg bereken vir verskeie diffusiekoëffisiënte. Die vergelyking tussen die modelresultate en die turbulensievrye Parker heliosferiese magneetveld model dui aan dat die mees waarskynlike pad wat bereken word baie na is aan die turbulensievrye Parker heliosferiese magneetveld vir klein diffusiekoëffisiënte, maar wat onderwond word soos wat die waarde van die diffusiekoëffisiënte toeneem. Hierdie bevindings stem ooreen met onlangse waarnemings.

Sleutelwoorde: veldlyndiffusie; heliosferiese magneetveld; turbulensie; numeriese metodes; stogastiese differensiaal-vergelykings.

Contents

1 Introduction **1**

2 The Turbulent Heliospheric Magnetic Field **3**

2.1 The Sun and solar wind 3

2.2 The heliospheric magnetic field 5

2.3 Turbulence 12

2.3.1 General background on turbulence 12

2.3.2 Turbulence models 15

2.3.3 Magnetic variance 17

2.3.4 Field-line random walk 18

2.4 Summary 19

3 Stochastic Differential Equations and the Field-line Random Walk Model **21**

3.1 Stochastic Differential Equations 21

3.1.1 Defining a Stochastic Differential Equation 21

3.1.2 Brownian Motion 24

3.2 A Stochastic FLRW Model 27

3.2.1 The convection-diffusion equation 27

3.2.2 Diffusion-free HMF 29

3.2.3 Added diffusion 33

3.3 Summary 39

4 A Random Walk Model for the Heliospheric Magnetic Field **40**

4.1 Construction of a Reference Scenario 40

4.2 Increased and Reduced Diffusion Values 52

4.3 Summary 56

5 Summary and Conclusions **57**

Table of abbreviations

1D	One-Dimensional
2D	Two-Dimensional
3D	Three-Dimensional
AU	Astronomical Units [1]
FLRW	Field-Line Random Walk
FISC	Field Intensity Solution Curve
FTE	Focused Transport equation
HCS	Heliospheric Current Sheet
HMF	Heliospheric Magnetic Field
PDE	Partial Differential Equation
SDE	Stochastic Differential Equations
SW	Solar Wind

[1] 1AU= 1.496×10^{11}m

Chapter 1

Introduction

The heliospheric magnetic field plays a fundamental role in the transport of charged particles, of both solar and galactic origin, throughout the heliosphere. The model presented by Parker (1958) has been observed to yield the most basic, but reasonably accurate, description for the heliospheric magnetic field within the ecliptic plane of the Sun. Smith and Bieber (1991) later suggest, from their observations on the 2D winding angle, the angle between the magnetic field and the radial direction, that the heliospheric magnetic field is more overwound at 1 AU than what the Parker model predicts. On the other hand, a recent study on the 3D winding angle conducted by Van Der Merwe and Engelbrecht (2025) suggests that the heliospheric magnetic field is underwound in actuality, which, according to the authors, corresponds with theory concerning the meandering of field-lines due to turbulence. The fluctuations in the field-lines caused by the turbulence in the solar wind can be estimated by the well-known field-line random walk (FLRW) approximation to a certain degree. While the FLRW approximation was studied in the past using simplified Cartesian geometries and homogeneous turbulence, very few theories account for the inhomogeneous nature of the Parker heliospheric magnetic field, and associated turbulence observed within the heliospheric magnetic field which often leads to deviations from the current analytical estimates. The purpose of this study is to investigate the effects of such a more realistic magnetic geometry.

The structure of the dissertation is as follows:

Chapter 2 will introduce concepts related to the Sun and its interplanetary extension through the solar wind and embedded magnetic field. The structure of the solar wind will first be discussed as well as its dependence on solar activity, radial distance and heliographic latitude, followed by an introduction on the frozen-in heliospheric magnetic field. It will also be shown how several authors derived models with which to describe the heliospheric magnetic field. The chapter will be concluded by introducing the basic concepts pertaining to turbulence theory.

Chapter 3 will give a brief introduction on stochastic differential equations (SDEs) by discussing the history of its discovery as well as the needed nomenclature and concepts relevant to this study. Following the discussion on SDEs, the SDE-based model for describing the field-line random walk process will be derived from the focused transport equation, following a similar approach to Jokipii (1966) to obtain field-line tracers that track the field-line probability distribution. Thereafter, the Fokker-Planck equation will be obtained and transformed into a set of SDEs, which describes the evolution of the magnetic field-line probability distribution.

In **chapter 4** a reference scenario will be establish by applying the SDE-based field-line random walk model to the Parker heliospheric magnetic field during solar minimum conditions. The reference scenario will then be compared to the turbulence-free Parker heliospheric magnetic field model. Finally, the model will again be applied to the Parker heliospheric magnetic field, but for more diffusive and less diffusive conditions, after which the results will again be compared to the turbulence-free Parker heliospheric magnetic field model.

The final chapter presents a summary of the content of each respective chapter as well as the conclusions drawn.

Chapter 2

The Turbulent Heliospheric Magnetic Field

This chapter introduces the key concepts and theory needed to understand the heliospheric magnetic field and the turbulence therein. The chapter starts off with an introduction to the Sun and solar wind, but mainly focuses on the solar wind, followed by a discussion on the heliospheric magnetic field as well as three different derivations thereof. The chapter concludes with the introduction of key concepts from turbulence theory relevant to the field-line random walk process.

2.1 The Sun and solar wind

The Sun, an ordinary yellow dwarf star located in the centre of the solar system at a distance of about $1\,\mathrm{AU} = 1.496 \times 10^{11}\,\mathrm{m}$ from the Earth, plays an important part in space physics as its periodic activity influences nearly all aspects of solar phenomena as well as phenomena elsewhere in the heliosphere, the main influence sphere of the Sun. A dominant periodic characteristic of the Sun is the Schwabe activity cycle, an ~ 11 year cycle which is also known as the solar cycle. During the solar cycle the Sun goes from a minimum activity phase, known as solar minimum, to a state of increased solar activity, known as solar maximum, back to a minimum activity phase. The principal measure with which to track the solar cycle is the number of irregularly shaped black spots, known as sunspots, on the solar surface. An aspect which is dramatically affected by the solar cycle is the solar wind (SW). The existence of the SW was first proposed by Biermann (1957) to explain his observations of the tail of a comet always pointing radially away from the Sun, regardless of its position. Biermann (1957) reasoned that the deflection of the ion tail of the comet was caused by a continuous outflowing plasma, seeing as it could not be explained by radiation pressure. Parker (1958) later built on the work of Biermann (1957) by using hydrodynamic equations to prove that it is not possible for the corona, the solar atmosphere, to be in complete hydrostatic equilibrium; this means that a continuous outward hydrodynamic expansion of ionised gas, or solar matter, possessing supersonic speeds is expected. Since then several spacecraft, including Mariner 2, Voyager 1 and Ulysses, have observed and confirmed the existence of the SW, with Ulysses being the first spacecraft to observe the SW around the polar regions. The observations made by these spacecraft revealed that the SW mainly consists of protons, electrons, and alpha particles, with a small percentage of ions belonging to other elements. These observations further found that the average proton speed of the outwards flowing plasma ranges from $\sim 400\,\mathrm{km.s^{-1}}$ to $\sim 800\,\mathrm{km.s^{-1}}$ and possesses an average density of ~ 7 particles.cm^{-3} that also changes with latitude (Phillips et al., 1995; McComas et al., 1998, 2003; Stix, 2004; Balogh et al., 2008; Smith, 2008; Cranmer et al., 2017).

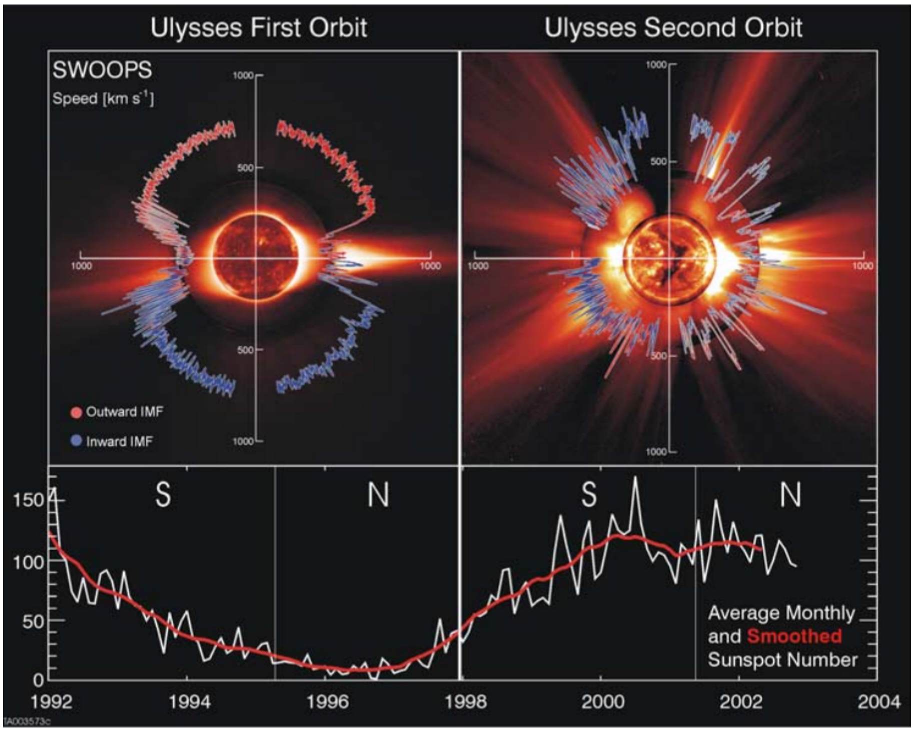

Figure 2.1: Top panels: Polar plots of the SW speed as observed by Ulysses during solar minimum (top left) and solar maximum (top right), with the colour of the curve indicating the magnetic polarity. Bottom panel: The average, along with the smoothed number of sunspots. The figure was taken from McComas et al. (2003).

Figure 2.1 shows data obtained by the Ulysses spacecraft during its first two orbits around the Sun. The top panels depict the SW speed and magnetic polarity measured during solar minimum and solar maximum respectively. The bottom panel shows the average and smoothed number of sunspots. The Ulysses spacecraft, which surveyed the Sun from heliographic latitudes of $-80.2°$ to $80.2°$, found that the SW is not constant over all latitudes. Rather, the SW speed is influenced close to the Sun by the Sun's magnetic field. Furthermore, Ulysses observed that the slow SW streams, which typically possess speeds of $\sim 400\,\mathrm{km.s^{-1}}$, generally originate near the solar equator, while the fast SW streams, with typical speeds of $\sim 800\,\mathrm{km.s^{-1}}$, mainly originate from the large coronal holes which cover the heliographic poles of the Sun. Coronal holes are regions of low plasma density in the solar corona with predominantly open magnetic fields. It should be mentioned that open magnetic fields mentioned here refer to field-lines that only appear to be open within the heliosphere since these field-lines stretch to distances greater than 100 AU and, at some point, will close to form a closed loop. The large coronal holes covering the heliographic poles are only present during solar minimum; as solar activity increases, the coronal holes start to fragment and shrink, which is to say, smaller coronal holes are located all over the Sun during solar maximum. The coronal holes during solar maximum are normally short-lived, causing the solar wind to rarely be fast; rather, the solar wind is a mixture of slow and fast wind at all heliographic latitudes. Furthermore, the solar wind speed evolves dynamically during both solar maximum and minimum as the different wind streams interact with one another (Phillips et al., 1995; Stix, 2004; Balogh et al., 2008; Cranmer, 2009; Cranmer et al., 2017).

For this study the observations on the heliospheric magnetic field (HMF) are confined to the ecliptic plane, therefore it will be assumed that the SW is slow and constant over the considered temporal and spatial scales. Excluding the regions near the Sun where the SW is in a state of acceleration, the SW will therefore be modelled by

$$\underline{v}_{sw} = v_{sw}\hat{e}_r,$$

where $v_{sw} = 400\,\mathrm{km.s}^{-1}$ is the SW speed and $\hat{e}_r$ is the radial direction unit vector.

2.2 The heliospheric magnetic field

Parker (1958) reasons that since the Sun's magnetic field permeates the solar corona, the SW will consequently drag the magnetic field-lines into the heliosphere. As a consequence of the high conductivity of the SW, the magnetic field are embedded into the SW and are carried off into heliosphere, thereby forming the HMF (Hathaway and Suess, 2008; Owens and Forsyth, 2013). The ratio of plasma pressure to magnetic pressure is known as the plasma-β. A low plasma-β and sub-Alfvénic flow generally implies a solar corona which is strongly structured by the magnetic field. It is therefore assumed that the plasma-β is below unity throughout the lower solar corona. As the SW moves through the Alfvén transition zone, located at a radial distance of $\sim 10 - 40\,\mathrm{r}_\odot$, the SW flow transitions to supersonic and super-Alfvénic, and the plasma-β moves towards unity; subsequently the SW becomes dominated by the flow of plasma (Chhiber et al., 2018a,b, 2024).

During solar minimum the magnetic field and corona become more organised, although not symmetrical about the solar rotation axis, such that the open magnetic field-lines are mainly located at polar coronal holes, with opposite polarities in the different hemispheres, and that the closed magnetic field-lines are generally found within the ecliptic plane. Therefore, the Sun's magnetic field can be approximated as dipolar with the magnetic dipole axis slightly tilted with respect to the solar rotation axis throughout solar minimum and most of the solar cycle. This angle between the rotation axis and the magnetic dipole axis is known as the tilt angle and plays an important part in both the large scale magnetic field and solar dynamo (Hoeksema, 1992; Alanko-Huotari et al., 2007). As mentioned, the magnetic dipole axis is slightly tilted with respect to the solar rotation axis throughout solar minimum, but as the solar cycle transition from solar minimum to solar maximum the tilt angle increases, causing the magnetic dipole axis to become almost equatorial at solar maximum Hoeksema (1992). During solar maximum the solar magnetic field is at its most dynamic, therefore it needs to be emphasised that aim of this study is to investigate the effect of turbulence on the HMF strictly under solar minimum conditions. As mentioned previously, the polar coronal holes shrink and fragment as the solar cycle approaches solar maximum; consequently small coronal holes can be found almost uniformly across the entire corona, the magnetic field intensity increases and open magnetic fields of both polarities can be found in both hemispheres (Weber and Davis, 1967; Chhiber et al., 2018b). Figure 2.2 shows the monthly and yearly averaged number of sunspots in the top panel to indicate solar minimum and solar maximum, while the bottom panel shows the 27-day averaged HMF intensity. By comparing the number of sunspots with the HMF intensity, it can be seen that the HMF intensity is highest during solar maximum and lowest during solar minimum.

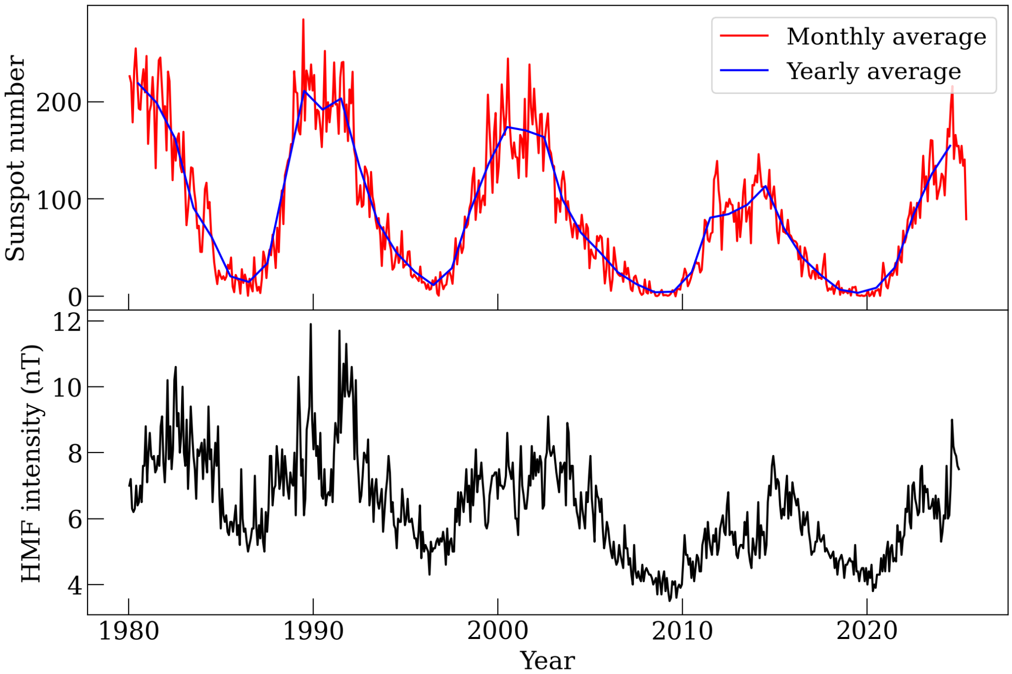

Figure 2.2: Monthly and yearly averaged sunspot number (top panel), and the 27-day averaged heliospheric magnetic field intensity near Earth (bottom panel). Data for the number of sunspots obtained from http://sidc.be/silso/ and heliospheric magnetic field intensity data obtained from https://omniweb.gsfc.nasa.gov/.

The opposite polarities of the dipole are separated by a thin boundary which encircles the Sun and extends throughout the heliosphere known as the heliospheric current sheet (HCS). Since the HMF is dipole-like, the HCS is unique and represents a boundary perpendicular to the opposite polarity fields. If the HMF were more complex, then several current sheets would exist and the HCS would be less distinctive. An essential feature of the HCS is the tilted magnetic dipole axis, which causes the HCS to oscillate about the heliographic equator, giving the appearance of a ballerina's skirt or a flying carpet, as can be seen in figure 2.3. During solar minimum the HCS lies near the heliographic equator, but with the increase of solar activity the HCS becomes more warped and appears to pass directly over the poles (Smith et al., 2001; Hathaway and Suess, 2008; Smith, 2008; Owens and Forsyth, 2013).

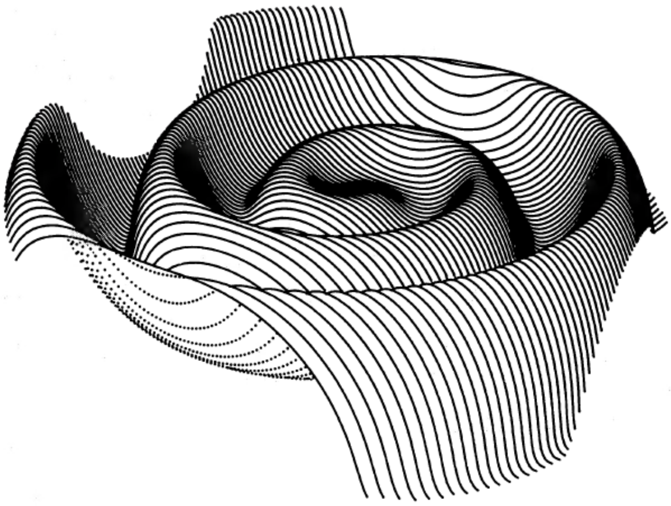

Figure 2.3: Depiction of the heliospheric current sheet. Image taken from Jokipii and Thomas (1981).

Several derivations exist for the HMF, but for this study only the derivations of Parker (1958), Gleeson and Webb (1980) and Steenkamp (1995) will be discussed. The most basic version of the HMF was derived by Parker (1958), and it holds quite well on average. To derive an equation for the HMF, Parker (1958) used magnetohydrodynamics, but ignored all electric currents and fields. The author further assumed that the outflow of gas from the Sun was spherically symmetric and that both the outward acceleration of the SW and the solar gravitation could be ignored beyond a radius $r = r_0$, so as to obtain a constant solar wind velocity, $\underline{v}_{sw}$, which is given in spherical coordinates by

$$v_r = v_{sw}, \quad v_\theta = 0, \quad v_\phi = \Omega(r - r_0)\sin\theta \tag{2.1}$$

when viewed from a co-rotating reference frame, where Ω is the rotation rate of the Sun and θ is the polar angle. Parker (1958) further states that a streamline possessing an azimuthal angle, ϕ_0, at $r = r_0$, can therefore be given by

$$\frac{r}{r_0} - 1 - \ln\left(\frac{r}{r_0}\right) = \frac{v_{sw}}{r_0\Omega}\left(\phi - \phi_0\right).$$

Since only steady-state conditions are considered and keeping in mind that one end of each line of force of the magnetic field is fixed in the Sun, it can be concluded that the magnetic field-lines coincide with the streamlines of the SW. If there is net flux being transported out of the Sun, then it follows that $\underline{B} = \alpha\underline{v}_{sw}$, where α is some scalar function. Considering that $\underline{\nabla}\cdot\underline{B} = 0$, as stated by Gauss' law for magnetism, a partial differential equation for α

can be obtained, where the characteristic curves are equation 2.1 which yields $\alpha = (a/r)^2$ along all such curves. Therefore the magnetic field at the point (r, θ, ϕ) is given by

$$B_r(r,\theta,\phi) = B_0 \left(\frac{r_0}{r}\right)^2$$
$$B_\theta(r,\theta,\phi) = 0$$
$$B_\phi(r,\theta,\phi) = B_0 \left(\frac{\Omega}{v_{sw}}\right)(r - r_0)\left(\frac{r_0}{r}\right)^2 \sin\theta,$$

where $B_0 = B(\theta, \phi_0)$ represents the magnetic field at $r = r_0$ and ϕ is related to ϕ_0 by equation 2.1. Since the SW expands radially outward from the Sun, it follows that the magnetic field-lines are directed radially outward as well. However, due to the field-lines being anchored to the Sun and solar rotation, the field-lines will form an Archimedean spiral. Figure 2.4 depicts the Parker HMF at polar angles of $\theta = \frac{\pi}{2}$, $\theta = \frac{\pi}{3}$ and $\theta = \frac{\pi}{4}$. In the equatorial plane ($\theta = \frac{\pi}{2}$) a simple Archimedean spiral is formed, but at higher latitudes the HMF forms a spiral with a constant half opening angle θ. It is therefore expected that the HMF will point radially away at the poles.

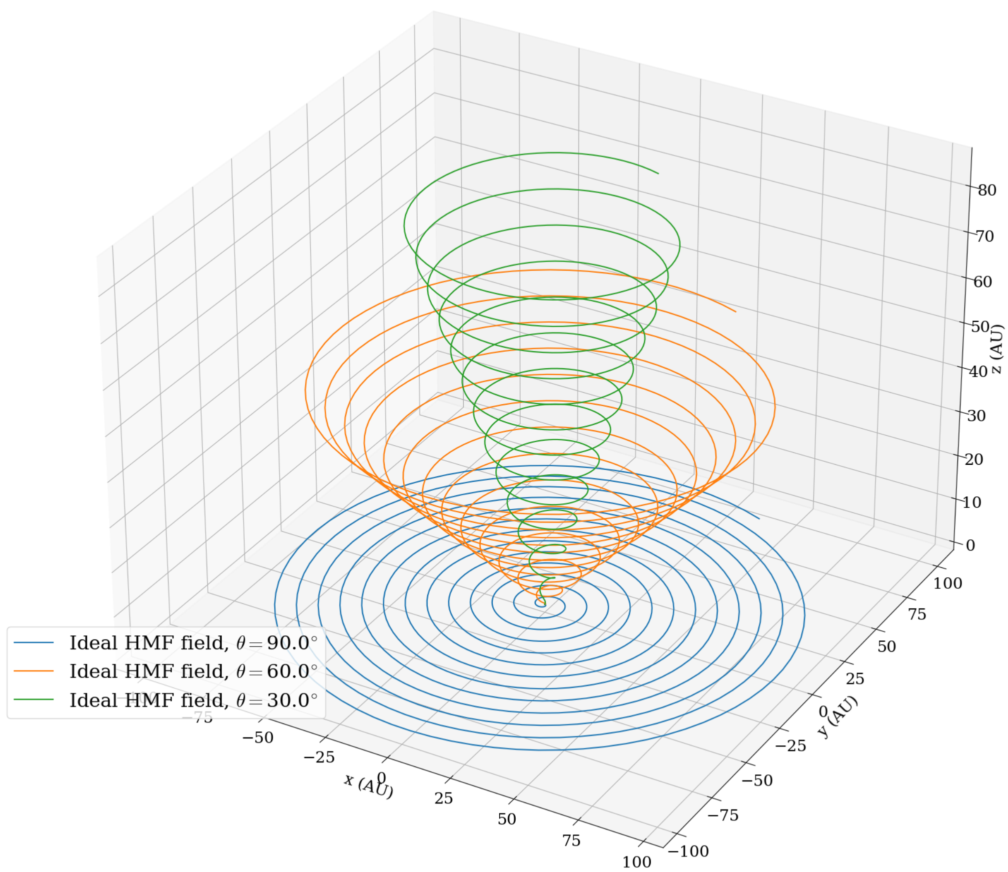

Figure 2.4: A representation of the ideal Parker HMF for $\theta = \frac{\pi}{2}$ (blue), $\theta = \frac{\pi}{3}$ (orange) and $\theta = \frac{\pi}{4}$ (green).

Gleeson and Webb (1980) took a different approach to Parker (1958) with the derivation of the HMF. Where Parker (1958) used magnetohydrodynamics, these authors utilised the Maxwell equations

$$\underline{\nabla} \cdot \underline{B} = 0 \tag{2.2}$$

$$\underline{\nabla} \times \underline{B} = \mu_0 \underline{J} \tag{2.3}$$

$$\underline{\nabla} \times \underline{E} = -\frac{\partial \underline{B}}{\partial t} \tag{2.4}$$

along with the equation for currents induced by the Lorentz force

$$\underline{J} = \sigma \left(\underline{E} + \underline{V} \times \underline{B} \right). \tag{2.5}$$

Similar to Parker (1958), these authors assumed that the magnetic field moves outward with the SW due to the magnetic field being frozen in to the SW. Substituting equation 2.3 into equation 2.5, thus eliminating $\underline{J}$, yields the electric field generated by the moving plasma and magnetic field, which is given by

$$\underline{E} = \frac{1}{\sigma \mu_0} (\underline{\nabla} \times \underline{B}) - \underline{V} \times \underline{B}. \tag{2.6}$$

On the right-hand side, the ratio of terms is $R_m = V \mu_0 \sigma L$, which is the magnetic Reynolds number with L a typical length and $\partial B / \partial x \sim B/L$. Assuming interplanetary space is an infinitely conductive plasma, meaning $\sigma \to \infty$, thus $R_m \gg 1$, from which it follows

$$\underline{E} = -\underline{V} \times \underline{B}. \tag{2.7}$$

Equation 2.7 can in turn be used to eliminate $\underline{E}$ from equation 2.4 to obtain the equation

$$\frac{\partial \underline{B}}{\partial t} = \underline{\nabla} \times \left(\underline{V} \times \underline{B} \right), \tag{2.8}$$

which governs the magnetic field. Considering that the HMF is frozen in the solar wind it follows that equations 2.2 and 2.6 need to be satisfied. For $\underline{V} = v_{sw} \hat{e}_r$, with v_{sw} constant, it follows

$$\begin{aligned} \underline{V} \times \underline{B} &= v_{sw} \hat{e}_r \times \left(B_r \hat{e}_r + B_\theta \hat{e}_\theta + B_\phi \hat{e}_\phi \right) \\ &= -v_{sw} \left(B_\phi \hat{e}_\theta - B_\theta \hat{e}_\phi \right) \end{aligned}$$

subsequently

$$\begin{aligned} \underline{\nabla} \times (\underline{V} \times \underline{B}) = & \frac{1}{r \sin\theta} \left[\frac{\partial}{\partial \theta} (v_{sw} B_\theta \sin\theta) + \frac{\partial}{\partial \phi} (v_{sw} B_\phi) \right] \hat{e}_r \\ & - \frac{1}{r} \left[\frac{\partial}{\partial r} (r v_{sw} B_\theta) \right] \hat{e}_\theta - \frac{1}{r} \left[\frac{\partial}{\partial r} (r v_{sw} B_\phi) \right] \hat{e}_\phi. \end{aligned}$$

When substituting the above equation into equation 2.8 the following is obtained

$$\frac{\partial B_r}{\partial t} = \frac{v_{sw}}{r \sin\theta} \left[\frac{\partial}{\partial \theta} (B_\theta \sin\theta) + \frac{\partial B_\phi}{\partial \phi} \right] \tag{2.9}$$

$$\frac{\partial B_\theta}{\partial t} = -\frac{v_{sw}}{r} \frac{\partial}{\partial r} (r B_\theta) \tag{2.10}$$

$$\frac{\partial B_\phi}{\partial t} = -\frac{v_{sw}}{r} \frac{\partial}{\partial r} (r B_\phi). \tag{2.11}$$

Using equations 2.9, 2.10, 2.11 and

$$\underline{\nabla} \cdot \underline{B} = \frac{1}{r^2}\frac{\partial}{\partial r}(r^2 B_r) + \frac{1}{r\sin\theta}\frac{\partial}{\partial\theta}(B_\theta \sin\theta) + \frac{1}{r\sin\theta}\frac{\partial}{\partial\phi}B_\phi = 0$$

it follows that

$$r^2 B_r = f_1(r - v_{sw}t, \theta, \phi) \tag{2.12}$$

$$r B_\theta = f_2(r - v_{sw}t, \theta, \phi) \tag{2.13}$$

$$r B_\phi = f_3(r - v_{sw}t, \theta, \phi). \tag{2.14}$$

For steady-state conditions at the surface of the Sun at $r = r_0$ and solar rotation rate Ω, it follows that

$$\underline{B} = B_0(r_0, \theta, \phi - \Omega t)\left(\hat{e}_r - \frac{\Omega r_0 \sin\theta}{v_{sw}}\hat{e}_\phi\right),$$

which, when utilised with equations 2.12, 2.13 and 2.14, give

$$\begin{aligned}
f_1(r_0 - v_{sw}t, \theta, \phi) &= r_0^2 B_0(r_0, \theta, \phi - \Omega t) \\
f_2(r_0 - v_{sw}t, \theta, \phi) &= 0 \\
f_3(r_0 - v_{sw}t, \theta, \phi) &= -\frac{r_0^2 \Omega \sin\theta}{v_{sw}} B_0(r_0, \theta, \phi - \Omega t),
\end{aligned}$$

which becomes

$$\begin{aligned}
f_1(r - v_{sw}t, \theta, \phi) &= r_0^2 B_0(r_0, \theta, \phi - \Omega t + \frac{\Omega}{v_{sw}}(r - r_0)) \\
f_2(r - v_{sw}t, \theta, \phi) &= 0 \\
f_3(r - v_{sw}t, \theta, \phi) &= -\frac{r_0^2 \Omega \sin\theta}{v_{sw}} B_0(r_0, \theta, \phi - \Omega t + \frac{\Omega}{v_{sw}}(r - r_0)),
\end{aligned}$$

when making the replacement $t \to t + (r_0 - r)/v_{sw}$. Therefore the HMF is given by

$$\begin{aligned}
\underline{B} &= B_r \hat{e}_r + B_\theta \hat{e}_\theta + B_\phi \hat{e}_\phi \\
&= \frac{1}{r^2} f_1(r - v_{sw}t, \theta, \phi) e_r + \frac{1}{r} f_2(r - v_{sw}t, \theta, \phi)\hat{e}_\theta + \frac{1}{r} f_3(r - v_{sw}t, \theta, \phi)\hat{e}_\phi \\
&= \left(\frac{r_0}{r}\right)^2 B_0\left(r_0, \theta, \phi - \Omega t + \frac{\Omega}{v_{sw}}(r - r_0)\right)\left[\hat{e}_r - \frac{\Omega r \sin\theta}{v_{sw}}\hat{e}_\phi\right]
\end{aligned}$$

which is similar to Parker's equation.

Similar to Gleeson and Webb (1980), Steenkamp (1995) starts with equations 2.2, 2.3, 2.4 and 2.5 to obtain partial differential equations, which produce a vector expression for the HMF when solved using the SW flow. From equation 2.7 it follows that equation 2.4 can be written as

$$\underline{\nabla} \times \underline{E} = \underline{\nabla} \times \underline{V} \times \underline{B} = 0 \tag{2.15}$$

when considering a steady-state. If the heliosphere is axisymmetric, i.e. $\partial/\partial\phi = 0$, the polar and radial components of the above equation yield

$$V_r B_\theta - V_\theta B_r = \frac{f_1(r)}{\sin\theta}$$

and

$$V_r B_\theta - V_\theta B_r = \frac{f_2(\theta)}{r}.$$

Together, these conditions yield

$$V_r B_\theta - V_\theta B_r = \frac{C}{r \sin\theta}, \tag{2.16}$$

where C is a constant. Assuming that the SW is constant over all heliographic latitudes, it follows from equations 2.2 and 2.16 that

$$0 = \frac{1}{r^2}\frac{\partial}{\partial r}\left(r^2 B_r\right) = -\frac{1}{\sin\theta}\frac{\partial}{\partial\theta}\left(r\sin\theta B_\theta\right) = -\frac{1}{\sin\theta}\frac{\partial}{\partial\theta}\left(\frac{C}{V_r}\right),$$

with V_r independent of the polar angle. Therefore

$$B_r = B_\odot\left(\frac{r_\odot}{r}\right)^2,$$

where $\odot$ denotes the values on the solar surface. Assuming that $B_{\phi\odot} = 0$, the azimuthal component of equation 2.15 gives

$$r(V_\phi B_r - V_r B_\phi) = r_\odot V_{\phi\odot} B_{r\odot}. \tag{2.17}$$

The conservation of angular momentum density, given by $\underline{L} = \underline{r} \times \rho\underline{V}$, of the SW yields

$$rV_\phi = r_\odot V_{\phi\odot},$$

assuming ρ is constant, where $V_{\phi\odot}$ is the co-rotating velocity on the solar surface. Therefore equation 2.17 becomes

$$B_\phi = -B_{r\odot}\left(\frac{r_\odot}{r}\right)^2 \tan\psi\left[1 - \left(\frac{r_\odot}{r}\right)^2\right], \tag{2.18}$$

where

$$\tan\psi = \frac{\Omega r \sin\theta}{V_r}.$$

Note that the last term in equation 2.18 becomes negligible beyond a few solar radii. When normalising equation 2.18 in terms of the average magnetic field intensity, $B_e \approx 5 - 10\,\mathrm{nT}$, and average winding angle, $\psi_e \approx 45^\circ$, at a radial distance of $r_e = 1\,\mathrm{AU}$ equation 2.18 becomes

$$\underline{B} = B_e\left(\frac{r_e}{r}\right)^2 \cos\psi_e\left[\hat{e}_r - \tan\psi\hat{e}_\phi\right], \tag{2.19}$$

which possesses a magnitude of

$$B = B_e\left(\frac{r_e}{r}\right)^2 \frac{\cos\psi_e}{\cos\psi}$$

and where

$$\tan\psi = \frac{\Omega r \sin\theta}{V},$$

with $V = V_r$ denoting the radial SW velocity.

When the solar rotation rate is considered to be $\theta-$dependent, rather than constant over all heliographic latitudes, the derivation done by Steenkamp (1995) yields a different HMF model known as Fisk-type HMF (see, e.g. Fisk, 1996). Seeing as the main focus of this study is the effect of the field-line random walk process, which is discussed later within this chapter, on a Parker-type HMF, the Fisk-type HMF is not pertinent to this study. For a more detailed derivation of the Parker spiral away from the ecliptic plane, the reader is referred to Jokipii and Kóta (1989). For the purpose of this study a highly detailed HMF model is not needed, therefore it is sufficient to utilise the basic Parker HMF model derived by Parker (1958).

2.3 Turbulence

2.3.1 General background on turbulence

It was realized from early *in situ* observations that the SW is permeated by continuous fluctuations in the flow velocity, particle density, and the magnetic field. Furthermore, these fluctuations occur on all temporal and spatial scales, from the minute kinetic scales of particle gyromotion to the vast dimensions of the inner heliosphere (Marsch, 1991). It was later concluded by authors such as Coleman (1968) and Montgomery (1983) that the HMF is turbulent by proving that the spectrum of the HMF fluctuations is similar to the spectrum of speed fluctuations in a turbulent fluid (Burlaga, 1991). What follows is a brief introduction on the fundamental mathematical concepts of the power spectrum of the HMF fluctuations.

The total HMF, denoted by $\underline{B}$, can be decomposed into a mean magnetic field, $\underline{B}_0$, and magnetic field fluctuations, $\underline{b}$, so that

$$\underline{B} = \underline{B}_0 + \underline{b}, \tag{2.20}$$

with $\langle \underline{B} \rangle = \underline{B}_0$ and $\langle \underline{b} \rangle = 0$, where the angle brackets denote an ensemble average. The SW density and flow velocity can be decomposed in a similar fashion, although for the purpose of this study it is assumed that the local SW is incompressible (see, e.g. Matthaeus et al., 1990; Breech et al., 2008). To describe the evolution of a turbulent magnetic field, knowledge on how the $\underline{B}$ values at different times are related is needed, therefore a function needs to be defined with which to obtain the correlation of the fluctuations between two points. The correlation tensor for two points a distance $\underline{r}$ apart is represented by

$$R_{ij}(\underline{r}) = \langle \underline{b}_i(\underline{x}) \underline{b}_j(\underline{x} + \underline{r}) \rangle,$$

assuming that the turbulence is spatially homogeneous. By assuming that the turbulence is homogeneous, it follows that

$$R_{ij}(\underline{r}) = R_{ij}(-\underline{r})$$

and that $R_{ij}(\underline{r})$ is independent of $\underline{x}$. Using Gauss' law for magnetism it follows that

$$\frac{dR_{ij}(\underline{r})}{dx_i} = 0. \tag{2.21}$$

It is also important to mention that $R_{ii}(0) = \delta B_i^2$ when evaluating the correlation function at zero separation, where δB_i^2 is the mean square amplitude of the i-th fluctuating component (Batchelor, 1953; Tennekes and Lumley, 1972; Davidson, 2004).

Using the transform pair

$$S_{ij}(\underline{k}) = \left(\frac{1}{2\pi}\right)^3 \int d^3r R_{ij}(\underline{r}) e^{-i\underline{k}\cdot\underline{r}} \tag{2.22}$$

$$R_{ij}(\underline{r}) = \int d^3k S_{ij}(\underline{k}) e^{i\underline{k}\cdot\underline{r}} \tag{2.23}$$

yields the homogeneous symmetric spectral tensor,

$$S_{ij}(\underline{k}) = \left(\delta_{ij} - \frac{k_i k_j}{k^2}\right) S(\underline{k}),$$

as is given by Batchelor (1953), where $S(\underline{k})$ is the modal spectral density and the δ_{ij} is the Kronecker symbol. From equations 2.21 and 2.23 it follows that

$$\int d^3k k_i S_{ij}(\underline{k}) e^{i\underline{k}\cdot\underline{r}} = 0,$$

which holds for all k-space, therefore $k_i S_{ij} = 0$. The Fourier transform of $R_{ij}(\underline{r})$ is known as the power spectral density, or the power spectrum, and represents a cascade of energy from large scales to smaller scales. Note that it is possible for energy to cascade from smaller to larger scales as well. Thus $E(k)$ is the amount of energy contained in the $\underline{k}$-th mode of $\underline{b}(\underline{k})$. Several ranges of interest exist within this energy spectrum, due to the various interactions between the fluctuations and the processes which drive the turbulence. A few of these ranges are indicated in figure 2.5 which displays the turbulent spectrum $E(k)$. The first of the subranges is the energy containing scales. The energy containing scales possess the lowest wavenumbers and are the range where most of the energy is added to the spectrum, thereby providing a source of energy for the turbulent cascade. For wavenumbers beyond the turnover scale a range known as the universal equilibrium range exists, which is further divided into the inertial subrange and the dissipation subrange. Within the inertial subrange the transfer of energy is dominated by inertial forces, while the dissipation range is the range in which the fluctuations are converted to thermal energy, and thereby heating the background plasmas (Batchelor, 1953; Tennekes and Lumley, 1972; Frisch and Kolmogorov, 1995; Goldstein et al., 1995; Davidson, 2004; Matthaeus et al., 2007).

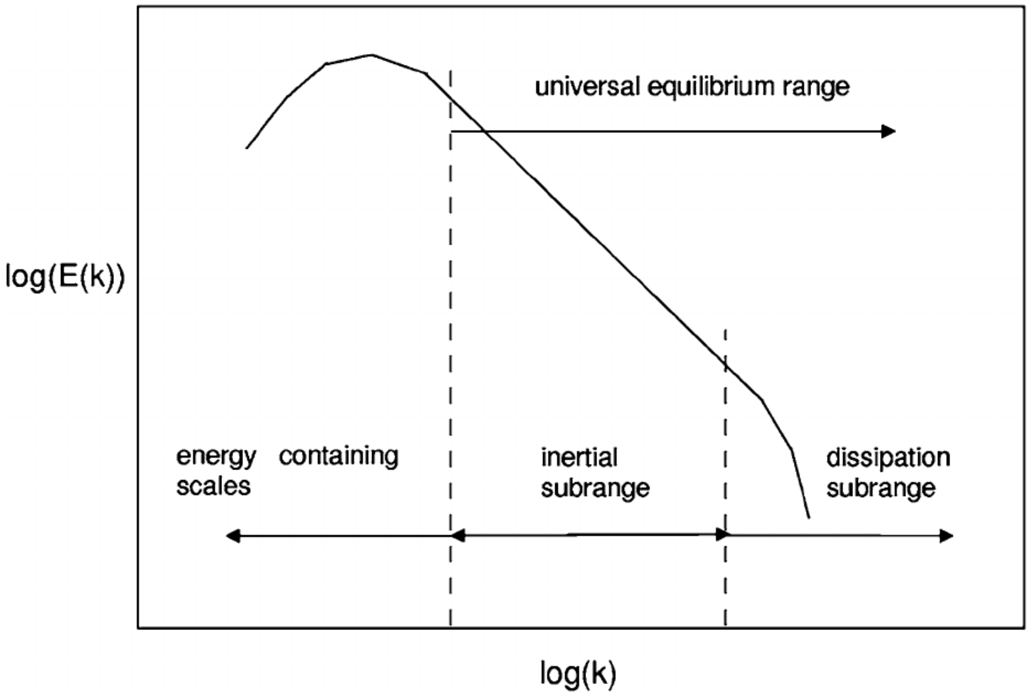

Figure 2.5: Depiction of the wavenumber dependence of the fully developed turbulence power spectrum with its various subranges. Image taken from Petrosyan et al. (2010)

Observations of the magnetic power spectra found that the spectral density of the inertial and dissipation subranges varied according to a power-law (Coleman, 1968). By using dimensional analysis Kolmogorov (1941) predicted an associated exponent, also known as a spectral index, of $-\frac{5}{3}$ for the inertial range. Within the dissipation range, the power-law dependence is determined by the type of turbulent fluctuation, causing the power-law dependence to be highly variably, although the spectral index for the dissipation range usually remains around -3 (Leamon et al., 1998; Smith et al., 2006a). From the observations of the magnetic power spectra, some studies have found that the energy containing scales possess a flat wavenumber dependence (see, e.g. Hedgecock, 1975), while other authors found a wavenumber dependence of k^{-1} (see, e.g. Marsch, 1991; Goldstein and Roberts, 1999). There are several lengthscales associated with the power spectrum. The lengthscales used usually depend on the turbulence model which is being utilised. The lengthscales relevant to this study are the ultrascale, the correlation length, and outerscale. The ultrascale is a lengthscale which is associated with the curvature of the correlation function, $R_{ij}(\underline{r})$, at zero separation. The ultrascale is often used in the 2D turbulence model, discussed in the next section, to determine the field-line diffusion and particle transport properties. The correlation length, also known as the integral scale, is associated with the area under $R_{ij}(\underline{r})$ and represents the lag at which the autocorrelation function$R_{ij}(\underline{r})$ drops to $1/e$ of its initial zero lag value, where $e \sim 2.71828$ is Euler's number. The outerscale, in this case, characterises the onset of the energy containing scales, and should not be confused with the Kolmogorov outerscale which describes the energy cascade within the inertial subrange (Batchelor, 1953; Tennekes and Lumley, 1972; Choudhuri, 1998; Ruffolo et al., 2004; Matthaeus et al., 2007).

Various models exist with which to simulate turbulence and the processes thereof. The turbulence model used within this study is the 2D turbulence model, although the slab turbulence model will also be discussed.

2.3.2 Turbulence models

For the discussion on turbulence models a right-handed coordinate system is assumed, with $\underline{B}_0$ oriented along the unit vector $\hat{e}_z$. Furthermore, the spectra are described in terms of wavenumbers which are parallel to the unit vector $\hat{e}_z$, denoted by k_z, and wavenumbers perpendicular to the unit vector, denoted by k_x and k_y. For perpendicular fluctuations, the notation $k_\perp = (k_x^2 + k_y^2)^{1/2}$ is utilised, assuming that the fluctuations are axisymmetric. Finally, the root mean square amplitudes for the various fluctuations are denoted by δB, with a subscript to indicate the type of fluctuation which is considered.

Slab turbulence

Jokipii (1966) proposed that the turbulent fluctuations in HMF could be described using a slab turbulence model. The slab turbulence model assumes that the perpendicular fluctuations of the mean magnetic field vary purely along the mean magnetic field, that is to say along the z-coordinate, such that equation 2.20 can be written as

$$\underline{B} = B_0\hat{e}_z + b_{slab,x}(z)\hat{e}_x + b_{slab,y}(z)\hat{e}_y,$$

assuming that the fluctuations are axisymmetric, that is $b_{slab,x}(z)\hat{e}_x = b_{slab,y}(z)\hat{e}_y$. Moreover, it is assumed that the fluctuations propagate along the $\hat{e}_z$-direction, therefore the slab turbulence model describes the Alfvén type fluctuations within the SW. Therefore, a mean magnetic field which experiences purely slab turbulence will wander along the x- and y-axis as the value along the z-axis increases. However, field-lines which start at the same z-coordinate, but at different x- and y-coordinates, will wander in the exact same way, as can be seen in figure 2.6 (Goldstein et al., 1995; Osman and Horbury, 2007).

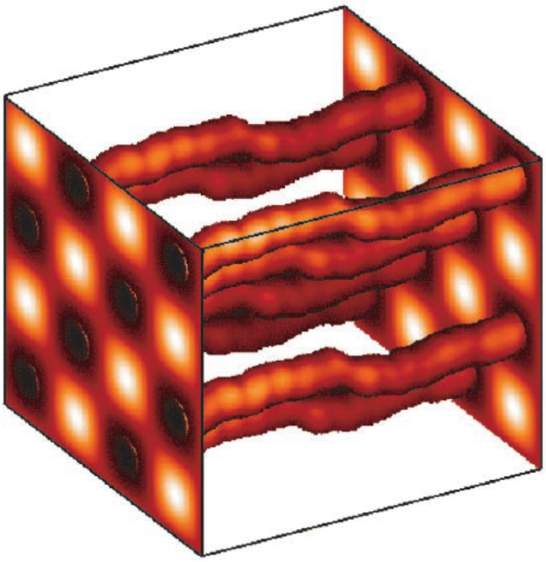

Figure 2.6: Depiction of the magnetic flux tubes for a purely slab turbulence model. Image taken from Matthaeus et al. (2003).

2D turbulence

On the other hand, the 2D turbulence model assumes that the fluctuations are functions of the transverse coordinates, namely x and y, such that equation 2.20 can be written as

$$\underline{B} = B_0\hat{e}_z + b_{2D,x}(x,y)\hat{e}_x + b_{2D,y}(x,y)\hat{e}_y.$$

Furthermore, it is assumed that the fluctuations are perpendicular to the mean magnetic field, meaning that $\underline{B}_0 \cdot \underline{b} = 0$, and that the wave vectors associated with the fluctuations remain in the (k_x,k_y) plane. Seeing as the fluctuations are divergence-free, the fluctuating component can be rewritten as

$$\underline{b}(x,y) = \underline{\nabla} \times a(x,y)\hat{e}_z, \tag{2.24}$$

where $a(x,y)$ is some vector potential and is assumed to take a form where no large spatial gradients are present. From equation 2.24 it follows that the fluctuations will be perpendicular to $a(x,y)$, which implies that a magnetic field-line will follow a path where $a(x,y)$ remains constant (Matthaeus et al., 1995; Ruffolo et al., 2004; Chuychai et al., 2007).

Figure 2.7 illustrates magnetic field-lines experiencing purely 2D turbulence. The magnetic field-lines which originate from the same z value, but different x and y values all follow different individual paths, essentially independent of one another, according to the respective fluctuations being sampled (Matthaeus et al., 1995).

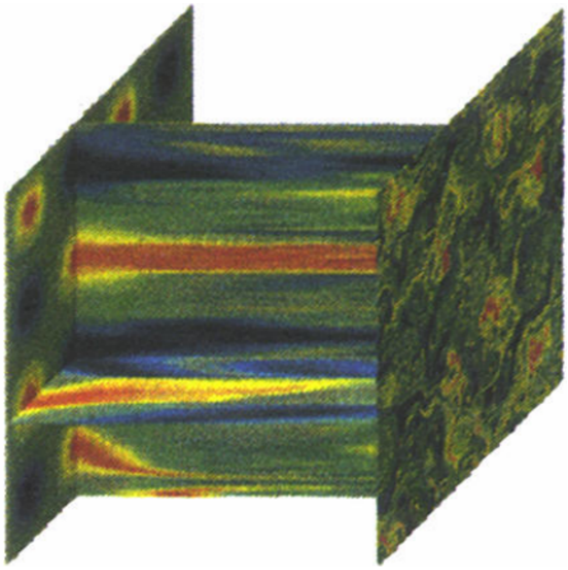

Figure 2.7: Depiction of the magnetic surfaces for a purely 2D turbulence model. Image taken from Matthaeus et al. (1995).

Although several other turbulence models exist, such as the composite turbulence model, these models are beyond the scope of this study which utilizes a purely 2D turbulence model; the other models will therefore not be discussed.

2.3.3 Magnetic variance

The magnetic variance, denoted by δB^2, can be calculated from the root-mean-square amplitude of the HMF fluctuations. Figure 2.8 shows the observed total magnetic variance in the ecliptic plane for various radial distances. Moreover, the figure depicts the de-normalised Voyager 2 data presented by Zank et al. (1996) and Smith et al. (2006b). To de-normalize the Voyager 2 data, Engelbrecht (2013) utilized a solar minimum value of 5 nT for the average HMF intensity at Earth. From the figure it can be seen that the magnetic variance decreases as the radial distance increases, where, according to Burger and McKee (2023), the radial dependence of the magnetic variance is around $r^{-2.4}$. It has also been found, by authors such as Smith and Bieber (1991) and Erdős and Balogh (2005), that the magnetic variance has a heliographic latitude dependency; such that the magnetic variance is greater at higher latitudes, which implies higher levels of turbulence within the SW over the polar regions. Similar measurements and analyses can be used to determine all relevant lengthscales and spectral indices, and their radial dependence, needed to describe SW turbulence.

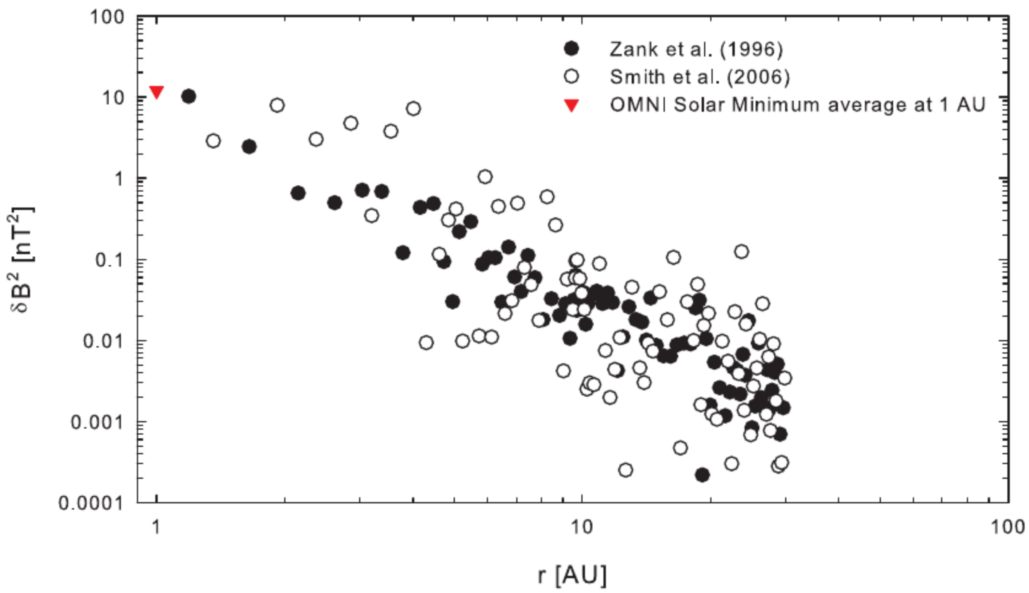

Figure 2.8: Total magnetic variance as a function of radial distance. Figure taken from Engelbrecht (2013).

2.3.4 Field-line random walk

As a consequence of the turbulent and stochastic nature of the HMF, individual magnetic field-lines often deviate from the ideal Parker HMF, as illustrated by figure 2.9. These erratic movements, which came to be known as the field-line random walk (FLRW), are brought about by the turbulent fluid motions within the solar wind, as mentioned previously, as well as by the motions in the photosphere. Observations of the solar wind indicate that it is these motions of the photosphere which generate most of the FLRW during quiet times. Furthermore, it is found that the FLRW dominates the perpendicular diffusion of particles in interplanetary space. Another consequence of the FLRW is the increase and decrease of magnetic field path lengths depending on the fluctuations. The FLRW can even lead to the twisting and interlacing of adjacent field-lines (Jokipii and Parker, 1969; Jokipii, 1973; Shalchi and Weinhorst, 2009; Shalchi, 2019; Chhiber et al., 2021).

Jokipii and Parker (1969) found that the FLRW can be related to the power spectrum of the magnetic field and that the FLRW dominates the particle diffusion perpendicular to the mean HMF. Therefore, the understanding of the FLRW process can be considered a key aspect of turbulence theory and space science as the transport and diffusion of energetic particles are directly influenced by the stochastic wandering of the HMF (see, e.g. Shalchi and Kourakis, 2007; Weinhorst et al., 2008).

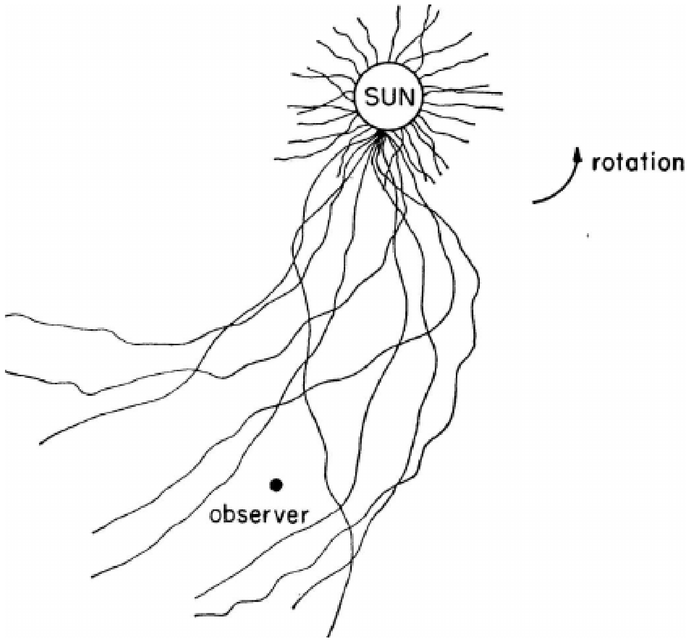

Figure 2.9: Illustration of the field-line random walk of the heliospheric magnetic field. Figure taken from Jokipii and Parker (1969).

2.4 Summary

In this chapter the concepts necessary for the rest of the study were introduced. These include the dynamic nature of the Sun, caused by the increase and decrease of solar activity over a period of ~ 11 years, which influences almost all of the structures and processes present within the heliosphere. This was followed by a discussion on the continuous supersonic outflow of solar matter known as the solar wind. During solar minimum, the solar wind possesses a strong heliographic latitudinal dependency, such that slow solar wind is most often observed within the ecliptic plane, while fast solar wind is mostly observed over the polar coronal holes. During solar maximum the heliographic latitudinal dependency of the solar wind disappears and both slow and fast solar wind can be observed over all latitudes.

The heliospheric magnetic field, which is frozen into the solar wind, along with the neutral current sheet which separates the opposite polarities of the heliospheric magnetic field were discussed as well. Furthermore, during solar minimum the heliospheric magnetic field has an approximate dipole structure, while during solar maximum the structure becomes much more complex. Within the discussion of the heliospheric magnetic field, the Parker model was introduced as well as several derivations for the model. According to the Parker model, the heliospheric magnetic field is in the form of Archimedian spirals.

Lastly, the basic concepts of turbulence theory were introduced. These concepts include the correlation tensor used to describe the evolution of a magnetic field within homogeneous turbulence, and the turbulence power spectrum, which represents the cascade of energy from large wavenumbers to smaller wavenumbers. The subranges of the power spectrum, namely the inertial and the dissipation range, vary according to a power-law with spectral indices of $-\frac{5}{3}$ and -3 respectively. The energy containing scales has a wavenumber dependence of k^{-1}, although some studies have reported a flat wavenumber dependence. The power spectrum is also associated with various lengthscales, albeit only the ultrascale, the outerscale and the correlation length were mentioned within this chapter as these are the only lengthscales relevant to this study. The slab turbulence and the 2D turbulence models used to simulate turbulence were discussed. The slab model is mainly used to simulate Alfvén type fluctuations, while the 2D model is mostly used to simulate the transverse fluctuations within a magnetic field-line. The magnetic variance was found to be dependent on both the radial distance and heliographic latitude, such that the variance decreases with radial distance, while increasing with latitude. Finally, the field-line random walk was introduced. The field-line random walk directly influences particle transport within the heliosphere, therefore a greater understanding of the field-line random walk process is needed to further knowledge about turbulence-particle interactions.

Chapter 3

Stochastic Differential Equations and the Field-line Random Walk Model

Chapter 3 gives a brief introduction on stochastic differential equations (SDEs), as well as a discussion on the newly constructed SDE-based field-line random walk model. To start with, a definition of an SDE is introduced and the history thereof is given. This is followed by a discussion and illustration of the similarity between Fokker-Planck equations and SDEs through the use of Brownian motion as an example. Once an equivalence has been established, the field-line diffusion equation is derived from the particle transport equation and then solved numerically for both a non-diffusive and diffusive magnetic field by transforming the equation into a set of SDEs.

3.1 Stochastic Differential Equations

3.1.1 Defining a Stochastic Differential Equation

Several textbooks deal with the study of stochastic calculus and the applications, derivations and mathematical formalism thereof (e.g. Gardiner (1985), Kloeden et al. (1994), Kloeden and Platen (1999), Øksendal (2000), van Kampen (2007)). For the interested reader new to the world of stochastic calculus, Lemons (2002) and Strauss and Effenberger (2017) are recommended. The discussion on SDEs is based on these sources and only the most relevant aspects will be presented. For the purpose of this study it is sufficient to define an SDE as any differential equation that possesses the form

$$\frac{dx(t)}{dt} = a(x,t) + b(x,t)\zeta(t) \tag{3.1}$$

for the one-dimensional case, where $a(x,t)$ and $b(x,t)$ are continuous functions and $\zeta(t)$ is a rapidly varying stochastic function, also known as the noise term. The noise term, generally assumed to be a Markov process, is required to have an average of zero, otherwise the mean can be absorbed into the definition of $a(x,t)$. $x(t)$ represents a stochastic process, which is the time evolution for some random variable X. A random variable, also known as a stochastic variable, is a quantity which can assume any value from a set of possible values. The first and second term on the right hand side of equation 3.1 are respectively referred to as the drift term and the diffusion term. The drift term is a slowly varying continuous function representing the deterministic behaviour of a system, while the diffusion term is a rapidly varying continuous random function which represents the stochastic nature of a system, these terms should not be confused with the physical drift and diffusion terms used in the particle transport equation (Gardiner, 1985; Kloeden and Platen, 1999; Lemons, 2002; van Kampen, 2007; Strauss and Effenberger, 2017).

For this study only Itō type SDEs are considered, where equation 3.1 can be written as

$$dx(t) = a(x,t)dt + b(x,t)dW(t) \tag{3.2}$$

where $dW(t) = \zeta(t)dt$, which represents the Wiener process, can also be understood as the integral of the stochastic function in equation 3.1. The Wiener process is a time stationary stochastic Lévy process with the time increments possessing a Gaussian or normal distribution with a variance of dt on the mean of zero. This means that $dW(t) = W(t+dt) - W(t) \sim \mathcal{N}(0, dt)$. Equation 3.2 can be integrated as

$$x(t) = x_0 + \int_0^t a(x,t')dt' + \int_0^t b(x,t')dW(t') \tag{3.3}$$

where the second term on the right hand side is a normal (Riemann or Lebesgue) integral and the third term is an Itō type stochastic integral. Note that various different types of SDEs exist in addition to the Itō types, such as the Stratonovich stochastic formulation, and that the numerical methods described in this study may not be applicable to solve SDEs that do not belong to the Itō type, since the SDE formulations use different temporal discretizations. Unfortunately, there are only a few scenarios for which analytical solutions exist for SDEs, thus equation 3.3 must be integrated numerically (Gardiner, 1985; Kloeden and Platen, 1999; Øksendal, 2000; Lemons, 2002; van Kampen, 2007).

Most commonly, the SDEs are integrated using the Euler-Maruyama numerical scheme. By choosing a finite time step, denoted as Δt, equation 3.2 can be solved iteratively using

$$x^{t+\Delta t} = x^t + a(x,t)\Delta t + b(x,t)\Delta W(\Delta t) \tag{3.4}$$

from an initial position $x = x_0$ at time $t = 0$. This process continues until either a temporal integration limit is reached at $t = t_N$, or a boundary is reached at $x = x_e$ at a time $t = t_e$. The Wiener process is represented by $\Delta W(\Delta t)$ and is discretized as

$$\Delta W(\Delta t) = \sqrt{\Delta t} \cdot \Lambda(t)$$

where $\Lambda(t)$ is a pseudo-random number sampled from a Gaussian distribution. This temporal evolution of x is widely referred to as the trajectory of a pseudo-particle, although this term is a bit of a misnomer, since a pseudo-particle should not be considered to be a physical particle or even the guiding centre of a particle. The SDE model solves for $f(\underline{x}, t)$, meaning that a pseudo-particle represents a realization of $f(\underline{x}, t)$, therefore a more accurate term for a pseudo-particle would be a *phase space density element*. While the term pseudo-particle is not entirely accurate, it is still widely used within the field of SDE based modulation models. Integrating equation 3.4 for only a single pseudo-particle is meaningless, since the integration must be performed over all possible trajectories, or a large number thereof, thus equation 3.4 is usually integrated $N >> 1$ number of times (Maruyama, 1955; Kloeden and Platen, 1999; Kopp et al., 2012; Strauss and Effenberger, 2017).

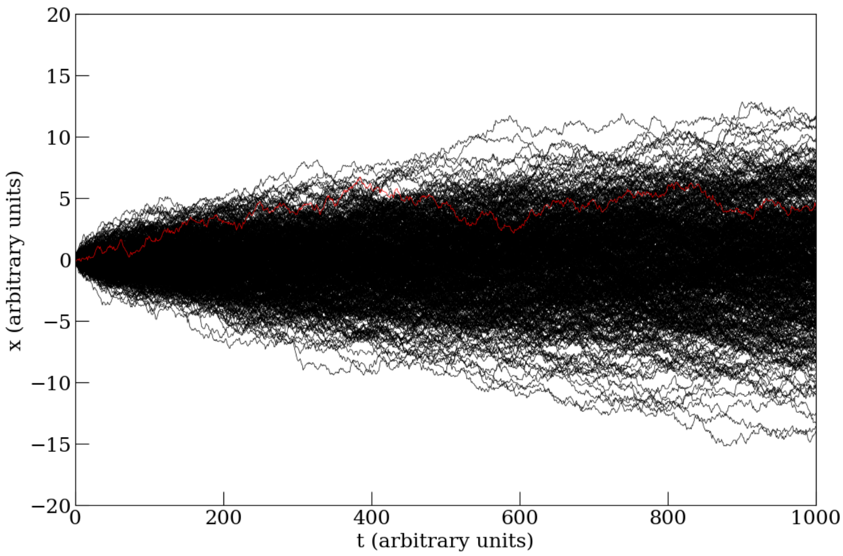

(a)

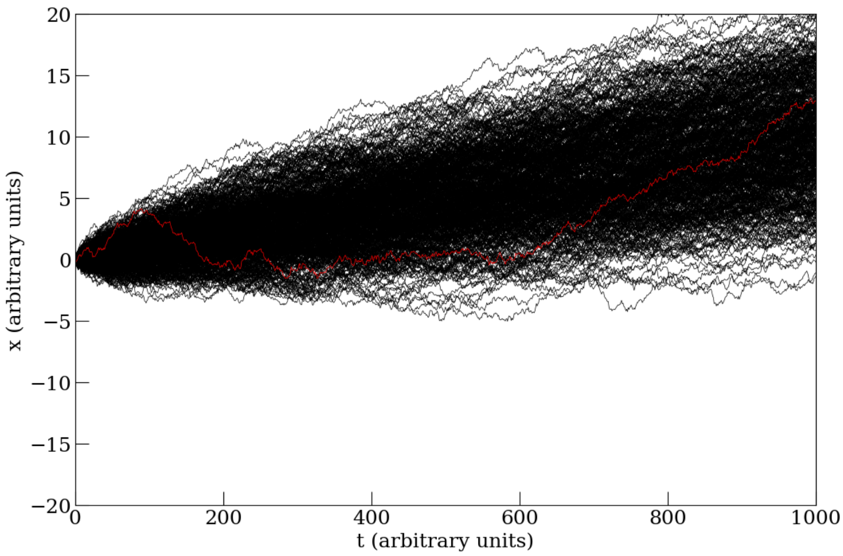

(b)

Figure 3.1: Solutions of equation 3.4 using $a(x,t) = 0$ and $b(x,t) = \sqrt{2}$ (panel a), and $a(x,t) = 1$ and $b(x,t) = \sqrt{2}$ (panel b). The integration is repeated for 10000 pseudo-particles for both cases, with the last pseudo-particle trajectory coloured red.

Figure 3.1 shows the pseudo-particle trajectories of 10000 pseudo-particles determined through the use of equation 3.4 for $a(x,t) = 0$ and $b(x,t) = \sqrt{2}$ (3.1a) and for $a(x,t) = 1$ and $b(x,t) = \sqrt{2}$ (3.1b). All of the pseudo-particle trajectories start at the same x-position, for figure 3.1 an initial x-position of $x_0 = 0$ is used, and continue on until a final time-step of $t_N = 1000$ is reached. The last pseudo-particle trajectory is coloured red in order to better depict the behaviour of a single pseudo-particle. The interpretation of figure 3.1 is given in the following section; at present it is sufficient to note that all of the pseudo-particles start at the exact same position and that, on average, the pseudo-particles move to larger values of $|x|$ as t increases. Furthermore, a normalized probability density, denoted by $\rho'(x,t)$, can be determined using the pseudo-particle trajectories, such that

$$\int_{\Omega} \rho'(x,t) d\Omega = 1 \tag{3.5}$$

where Ω represents the entire integration space, in this case, the spatial coordinate x. This is done numerically by dividing the variable values, in this case the values of x, into a series of bins. The number of pseudo-particles in each bin is then calculated. Finally, the number of pseudo-particles in each bin is divided by the total number of particles. Let N denote the total number of pseudo-particles, N' the number of intervals of width Δx and N_i the number of particles in bin i, thus equation 3.5 can be discretized as

$$\sum_{i=1}^{N'} \rho_i'(x,t)\Delta x = \sum_{i=1}^{N'} \frac{N_i}{N} = 1 \tag{3.6}$$

The solutions shown in figure 3.1 are binned at two different times as an example, the results are shown and discussed in the following section.

3.1.2 Brownian Motion

Brownian motion, one of the best known examples of a Markov process, is named after the British cleric and biologist Robert Brown, who, in the early nineteenth century, first systematically investigated the irregular and animated motions that small pollen grains suspended in water possess. An example of such motion is shown in figure 3.2a. This irregular movement was at first thought to be organic in origin and that these motions might indicate some vitality manifestation common in all forms of life; this hypothesis was later ruled out as particles obtained from non-living materials, such as ground glass and various metals, showed similar irregular motions. Einstein (1905) later proved that the random motions which Brown observed were caused by a series of collisions between the pollen grain and the water molecules through the use of thermodynamics. This led to the conclusion that the molecules and atoms that make up a fluid medium, such as air or water, move around randomly due to the thermal energy which they possess. If a particle were to be suspended within said fluid, then the atoms and molecules of the fluid would collide with the particle in arbitrary numbers from different directions at any given time. Due to the complexity of the motion of these molecules and atoms, the effect they have on the particle has to be described probabilistically (Gardiner, 1985; Lemons, 2002; van Kampen, 2007).

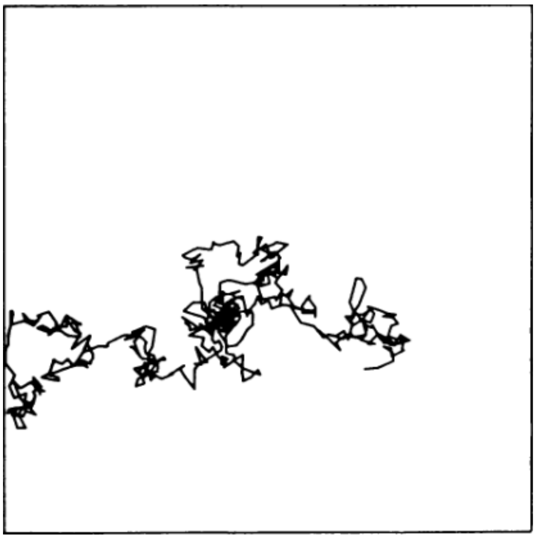

(a) Motion of a single point experiencing Brownian motion (Gardiner, 1985).

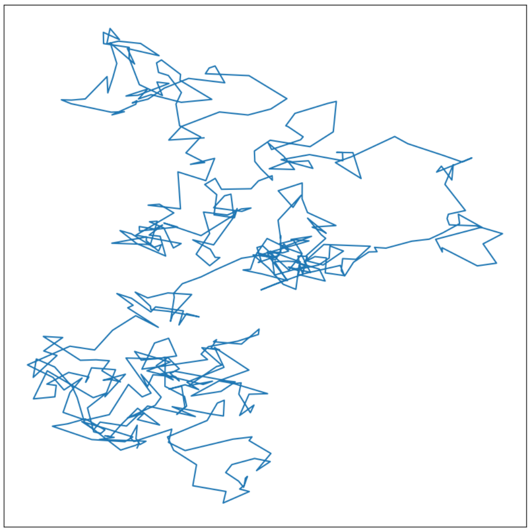

(b) Simulation of 2D Brownian motion using equation 3.7.

Figure 3.2

For an n-dimensional set of SDEs equation 3.2 can be generalized as

$$dx_i = a_i(x_i, s)ds + \sum_{j=1}^{n} b_{ij}(x_i, s)dW_i(s) \tag{3.7}$$

with a an n-dimensional vector and b a $n \times n$ matrix. Figure 3.2b depicts a Brownian motion simulation which utilized equation 3.7 for two dimensions where $a_1 = 0$, $b_{1,1} = \sqrt{2}$, $a_2 = 0.5$ and $b_{2,1} = \sqrt{2.5}$. It is apparent that figure 3.2b shows a remarkably similar motion to that of the single particle shown in figure 3.2a. Through the use of Itō's lemma it can be shown that for every SDE, or set of SDEs, an equivalent Fokker-Planck formulation exists. Generally these SDEs can be thought of as being integrated either forwards or backwards in time. When integrating equation 3.7 forwards in time the equation is equivalent to

$$\frac{\partial \rho(x_i, s)}{\partial s} = -\sum_{i=1}^{n} \frac{\partial}{\partial x_i}\left[a_i(x_i, s)\rho(x_i, s)\right] + \frac{1}{2}\sum_{i=1}^{n}\sum_{j=1}^{n} \frac{\partial^2}{\partial x_i \partial x_j}\left[C_{ij}(x_i, s)\rho(x_i, s)\right] + \mathcal{L}(x_i, s)\rho(x_i, s) \tag{3.8}$$

which is known as the time forward Kolmogorov equation; $\rho(x_i, s)$ represents a conditional probability density which depends on the various values of (x_i, s) and some final condition for ρ at a time T. It should also be mentioned that the variable s is a new time-marching coordinate that differs from actual time, this value signifies an independent parameter which increases at a constant rate. C_{ij} is the diffusion tensor and is given by

$$C_{ij}(x_i, s) \equiv \left(b_{ij}(x_i, s) \cdot b_{ji}(x_i, s)\right). \tag{3.9}$$

If equation 3.7 were to be integrated backwards in time, the time backwards Kolmogorov equation given by

$$-\frac{\partial \rho(x_i, s)}{\partial s} = \sum_{i=1}^{n} \tilde{a}_i(x_i, s)\frac{\partial \rho(x_i, s)}{\partial x_i} + \frac{1}{2}\sum_{i=1}^{n}\sum_{j=1}^{n} \tilde{C}_{ij}(x_i, s)\frac{\partial^2 \rho(x_i, s)}{\partial x_i \partial x_j} + \mathcal{L}(x_i, s)\rho(x_i, s) \tag{3.10}$$

is obtained. It is important to mention that $a \neq \tilde{a}$ and $C \neq \tilde{C}$ for most cases. Any linear terms produced by the transformation from a Fokker-Planck formulation to an SDE formulation is represented by $\mathcal{L}$. When $\mathcal{L}$ is present in either equation 3.8 or equation 3.10, it is also required to solve the auxiliary term

$$\frac{d\alpha}{ds} = \mathcal{L}\alpha(s)$$
$$\Rightarrow \alpha(s) = \alpha_0 \int_0^s e^{\mathcal{L}ds},$$

where $\alpha_0 = \alpha(s = 0)1$ and α represents a weighting factor which is applied to each pseudo-particle (Strauss and Effenberger, 2017). The two methods, time forwards and time backwards, are equivalent with both approaches describing the same process. The difference is that for the time forwards method the integration is started at a "source" and traced forwards towards an "observer", while for the time backwards method the integration is started at the observer and traced back in the direction of the source until the model boundaries are reached. The time backwards method is a much more efficient approach if the aim of the model is the evaluation of spectra, such as cosmic ray spectra, at a single point. Since the aim of this study is to simulate the diffusion of a singular field-line, it is required that each trajectory originates from the same position, therefore the main method used throughout the study is the time forwards method. The time backwards method is briefly presented as well to showcase similarities as well as differences between the two methods. Therefore any partial differential equation can be rewritten as set of SDEs and vice versa (Gardiner, 1985; Kloeden and Platen, 1999; Kopp et al., 2012; Bobik et al., 2016; Strauss and Effenberger, 2017).

As stated previously, Einstein (1905) proved that the irregular and animated motions of pollen grains suspended in water are caused by collisions between the water molecules and the pollen grains; furthermore he proved that the evolution of the probability distribution of the pollen grains is given by Fick's law, which is given by

$$\frac{\partial \rho(x,t)}{\partial t} = -V\frac{\partial \rho(x,t)}{\partial x} + \kappa \frac{\partial^2 \rho(x,t)}{\partial x^2}$$

assuming that V, the convective speed of the medium, and κ, the diffusion coefficient, are constant. By utilizing the initial condition $\rho(x,t) = \delta(x-0, t-0)$ and the absorbing boundary $\rho(x \to \infty, t) = 0$, the above equation can be analytically solved to obtain

$$\rho(x,t) = \frac{1}{\sqrt{4\pi\kappa t}} e^{-(x-Vt)^2/4\kappa t}. \tag{3.11}$$

Figure 3.3 shows the above analytical solution, with $\kappa = 1$, $V = 0$ (panel a) and with $\kappa = 1$, $V = 1$ (panel b), at times $t = 10$ and $t = 500$, depicted by the blue and orange lines respectively, as dashed lines compared to calculated $\rho(x,t)$ obtained from figure 3.1, shown as solid lines, which represents the SDE solution. Both of the solutions start with a very narrow Gaussian distribution and becomes broader over time, which corresponds to the characteristic Brownian diffusion. When including convection in the diffusion process, the distributions remain Gaussian, with the only difference being that $\rho(x,t)$ shifts either left or right depending on the convection. Clearly equation 3.4 and equation 3.11 describe the same process, since the SDE solution and the analytical solution yield similar results for $\rho(x,t)$ when $a(x,t) = V$ and $b(x,t) = \sqrt{2\kappa}$. It can therefore be concluded that if if the coefficients and boundary conditions used in both the partial differential equations (PDE) approach and SDE approach are equivalent, then the two approaches will yield the same results.

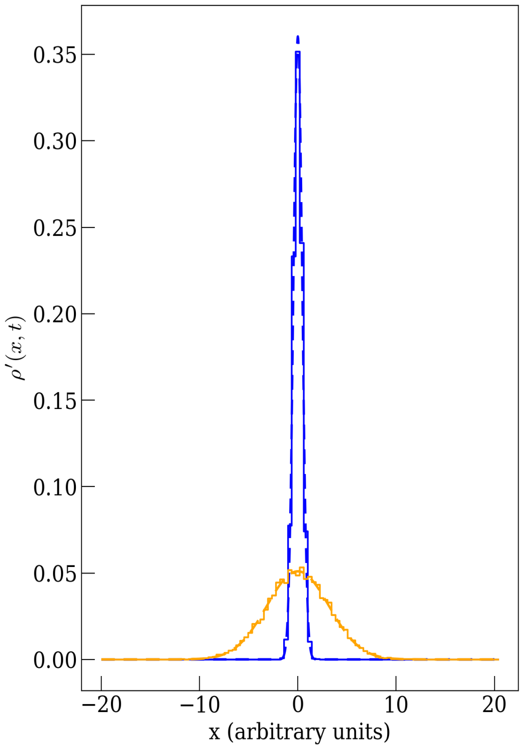

(a)

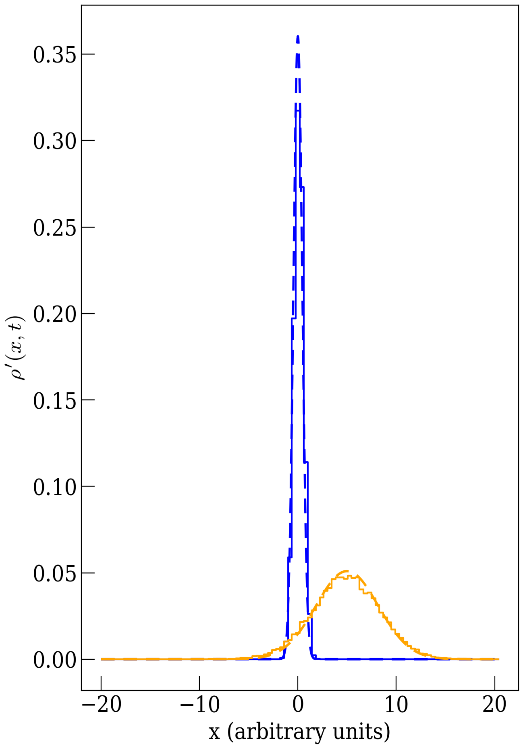

(b)

Figure 3.3: Solutions of equation 3.11 (dashed lines) for $\kappa = 1$, $V = 0$ (panel a) and $\kappa = 1$, $V = 1$ (panel b) for $t = 10$, indicated by the blue lines, and $t = 500$, indicated by the orange lines, compared to $\rho(x,t)$ (solid line) calculated from the SDE approach. The calculated ρ of panel a corresponds with figure 3.1a while the calculated ρ of panel b corresponds with figure 3.1b.

3.2 A Stochastic FLRW Model

3.2.1 The convection-diffusion equation

The convection-diffusion equation is derived from the focused transport equation (FTE)

$$\frac{\partial f}{\partial t} + \underline{\nabla} \cdot (\mu v \hat{e}_b f) + \frac{\partial}{\partial \mu}\left(\frac{1-\mu^2}{2L} v f\right) = \frac{\partial}{\partial \mu}\left(D_{\mu\mu}\frac{\partial f}{\partial \mu}\right) + \underline{\nabla} \cdot \left(\mathbf{D}_{\perp}^{(x)} \cdot \underline{\nabla} f\right) \tag{3.12}$$

for particles as given by Skilling (1971), where $\mathbf{D}_{\perp}$ is the perpendicular spatial diffusion coefficient of the particles, μ is the pitch-angle cosine, L is the magnetic focusing length and $D_{\mu\mu}$ is the pitch-angle diffusion coefficient as a result of turbulent scattering. Following a similar approach to Jokipii (1966), it is assumed that $\mu = 1$ (zero gyro-radius) gives the guiding centre of particles which trace random walking field-lines. Substituting $\mu = 1$ into equation 3.12 yields

$$\frac{\partial f_m}{\partial s} + \underline{\nabla} \cdot (\hat{e}_b f_m) = \underline{\nabla} \cdot (\mathbf{D} \cdot \underline{\nabla} f_m) \tag{3.13}$$

which is the convection-diffusion equation, where $f_m = f(\mu = 1)$ is the distribution function of the HMF field-line tracers, $\hat{e}_b$ is the direction of the background magnetic field, in this case the HMF, and $\mathbf{D} = \mathbf{D}_\perp(\mu = 1)/v_{||}$ is the field-line diffusion tensor, therefore it is important to note that $\mathbf{D}_\perp(\mu = 1) \neq \mathbf{D}_\perp^{(x)}$. Additionally, $ds = vdt$ is the distance along the HMF line. This should not be confused with the ds, which represents a time coordinate specifically, that was used in the previous section. Rather, the ds used in equation 3.13 represents a value of distance which varies with small increments. A simple representation of the HMF is given by

$$\underline{B}(r, \theta) = B_0 \left(\frac{r_0}{r}\right)^2 (\hat{e}_r - \tan\psi \hat{e}_\phi),$$

where r is the radial distance from the Sun, B_0 is the HMF intensity at the point of origin, $\hat{e}_r$ and $\hat{e}_\phi$ are the unit vectors in the direction of r and ϕ respectively and ψ is the winding angle (the angle between $\hat{e}_b$ and $\hat{e}_r$). It is assumed that the Parker field emanates from the source surface which is located at a radial distance $r = r_0$ from solar surface (Parker, 1958; Bian et al., 2024). Furthermore $\tan\psi$ is given by

$$\tan\psi = \frac{\Omega(r - r_0)\sin\theta}{v_{sw}}$$

with Ω representing the equatorial sidereal rotation rate of the Sun, v_{sw} the solar wind speed and θ the polar angle. Using $\sec^2\psi = 1 + \tan^2\psi$ it follows that

$$\begin{aligned}
\frac{1}{\cos^2\psi} &= 1 + \left(\frac{\Omega(r - r_0)\sin\theta}{v_{sw}}\right)^2 \\
\cos^2\psi &= \left[1 + \left(\frac{\Omega(r - r_0)\sin\theta}{v_{sw}}\right)^2\right]^{-1} \\
\cos\psi &= \left[1 + \left(\frac{\Omega(r - r_0)\sin\theta}{v_{sw}}\right)^2\right]^{-1/2}.
\end{aligned}$$

The equation for the direction of the background magnetic field, $\hat{e}_b$, can be determined using $\hat{e}_b = \frac{\underline{B}}{|\underline{B}|}$, thus an equation for the HMF intensity is first needed. The HMF intensity is calculated as follows

$$\begin{aligned}
|\underline{B}| &= \sqrt{B_r^2 + B_\phi^2} \\
&= \left[\left(B_0\left(\frac{r_0}{r}\right)^2\right)^2 + \left(B_0\left(\frac{r_0}{r}\right)^2\right)^2 \tan^2\psi\right]^{1/2} \\
&= B_0\left(\frac{r_0}{r}\right)^2 \sqrt{1 + \tan^2\psi} \\
&= B_0\left(\frac{r_0}{r}\right)^2 \sec\psi, \qquad (3.14)
\end{aligned}$$

from which $\hat{e}_b$ can be determined as a function of ψ, i.e.

$$\begin{aligned}\hat{e}_b &= \frac{B_0\left(\frac{r_0}{r}\right)^2(\hat{e}_r - \tan\psi\hat{e}_\phi)}{B_0\left(\frac{r_0}{r}\right)^2\sec\psi} \\ &= \frac{\hat{e}_r - \tan\psi\hat{e}_\phi}{\sec\psi} \\ &= \cos\psi\hat{e}_r - \sin\psi\hat{e}_\phi. \end{aligned} \tag{3.15}$$

Equation 3.15 can in turn be used to show that there is no change in the polar angle of the Parker field. Taking the cross product of $d\underline{l}$ and $\underline{B}$, where $d\underline{l} = dr\hat{e}_r + rd\theta\hat{e}_\theta + r\sin\theta d\phi\hat{e}_\phi$, gives

$$d\underline{l} \times \underline{B} = -B_0 r_0^2\frac{\Omega\sin\theta}{v_{sw}}d\theta\hat{e}_r + \left[B_0\frac{r_0^2\Omega\sin\theta}{rv_{sw}}dr + \sin\theta B_0\frac{r_0^2}{r}d\phi\right]\hat{e}_\theta - B_0\frac{r_0^2}{r}d\theta\hat{e}_\phi$$

Since the line element $d\underline{l}$ and the magnetic field are parallel to each other the cross product has to equal zero, therefore

$$\underline{0} = -B_0 r_0^2\frac{\Omega\sin\theta}{v_{sw}}d\theta\hat{e}_r + \left[B_0\frac{r_0^2\Omega\sin\theta}{rv_{sw}}dr + \sin\theta B_0\frac{r_0^2}{r}d\phi\right]\hat{e}_\theta - B_0\frac{r_0^2}{r}d\theta\hat{e}_\phi$$

meaning that

$$0 = -B_0 r_0^2\frac{\Omega\sin\theta}{v_{sw}}d\theta \tag{3.16}$$

$$0 = B_0\frac{r_0^2\Omega\sin\theta}{rv_{sw}}dr + \sin\theta B_0\frac{r_0^2}{r}d\phi \tag{3.17}$$

$$0 = -B_0\frac{r_0^2}{r}d\theta. \tag{3.18}$$

From equations 3.16 and 3.18 it can be concluded that $d\theta = 0$, meaning that the polar angle, θ, stays constant. Furthermore from equation 3.17 it follows that

$$\begin{aligned}-B_0\frac{r_0^2\Omega\sin\theta}{rv_{sw}}dr &= \sin\theta B_0\frac{r_0^2}{r}d\phi \\ \int d\phi &= -\frac{\Omega}{v_{sw}}\int dr \\ \phi &= -\frac{\Omega}{v_{sw}}r + const.\end{aligned}$$

Substituting $\phi = \phi_0$ and $r = 0$ yields $\phi_0 = const.$, thus

$$\phi = -\frac{\Omega}{v_{sw}}r + \phi_0,$$

which is the expression for a Parker HMF line.

3.2.2 Diffusion-free HMF

Assuming a diffusion-free Parker HMF implies that $\mathbf{D} = 0$. Substituting $\mathbf{D} = 0$ into the convection-diffusion equation yields

$$\frac{\partial f_m}{\partial s} + \underline{\nabla}\cdot(\hat{e}_b f_m) = 0 \tag{3.19}$$

where

$$\underline{\nabla} \cdot (\hat{e}_b f_m) = \frac{1}{r^2}\frac{\partial}{\partial r} r^2 f_m \cos\psi - \frac{1}{r\sin\theta}\frac{\partial}{\partial \phi} f_m \sin\psi. \tag{3.20}$$

Combining equations 3.19 and 3.20 gives

$$\begin{aligned}
0 &= \frac{\partial f_m}{\partial s} + \frac{1}{r^2}\frac{\partial}{\partial r} r^2 f_m \cos\psi - \frac{\sin\psi}{r\sin\theta}\frac{\partial f_m}{\partial \phi} \\
0 &= \frac{\partial f_m}{\partial s} + \frac{2}{r} f_m \cos\psi + \cos\psi \frac{\partial f_m}{\partial r} + f_m \frac{\partial \cos\psi}{\partial r} - \frac{\Omega\cos\psi}{v_{sw}}\frac{\partial f_m}{\partial \phi} \\
\frac{f_m \cos\psi}{r}\left[\frac{2+\tan^2\psi}{1+\tan^2\psi}\right] &= \frac{\partial f_m}{\partial s} + \cos\psi\frac{\partial f_m}{\partial r} - \frac{\Omega\cos\psi}{v_{sw}}\frac{\partial f_m}{\partial \phi}
\end{aligned}$$

which is in the form $a\frac{\partial f_m}{\partial s} + b\frac{\partial f_m}{\partial r} + c\frac{\partial f_m}{\partial \phi} = d$, which according to the characteristic equations of the quasilinear partial differential equation means that $\frac{ds}{dr} = \frac{a}{b}$, $\frac{df_m}{dr} = \frac{d}{b}$, etc. Therefore

$$\begin{aligned}
\frac{df_m}{dr} &= \frac{f_m \cos\psi}{r\cos\psi}\left[\frac{2+\tan^2\psi}{1+\tan^2\psi}\right] \\
\int \frac{1}{f_m} df_m &= \int \frac{1}{r}\left[\frac{2+\tan^2\psi}{1+\tan^2\psi}\right] dr \\
\ln f_m &= 2\ln r - \frac{1}{2}\ln(\tan^2\psi + 1) + const. \\
\ln f_m^2 &= \ln\left[\frac{\tan^2\psi+1}{r^4}\right] + const. \\
f_m &= \frac{const.}{r^2}\sqrt{\tan^2\psi + 1}
\end{aligned}$$

thus $f_m \propto B$, which implies that the distribution function is proportional to the Parker HMF strength.

Time-forwards ideal HMF

Using equation 3.19, which assumes a diffusion free HMF, and keeping the derivatives in the equation in "conservative" form yields

$$\begin{aligned}
\frac{\partial f_m}{\partial s} &= -\underline{\nabla}\cdot(\hat{e}_b f_m) \\
&= -\frac{1}{r^2}\frac{\partial}{\partial r} r^2 f_m \cos\psi + \frac{1}{r\sin\theta}\frac{\partial}{\partial \phi} f_m \sin\psi \\
&= -\frac{1}{r^2}\left[2r f_m \cos\psi + r^2 \frac{\partial}{\partial r}(f_m\cos\psi)\right] + \frac{1}{r\sin\theta}\frac{\partial}{\partial\phi} f_m \sin\psi
\end{aligned}$$

therefore equation 3.19 can be written as

$$\frac{\partial f_m}{\partial s} = -\frac{\partial}{\partial r} f_m \cos\psi + \frac{\partial}{\partial \phi}\frac{f_m \Omega}{v_{sw}}\cos\psi - \frac{2 f_m}{r}\cos\psi \tag{3.21}$$

where $\sin\psi$ is given by

$$\begin{aligned}
\sin\psi &= \tan\psi\cos\psi \\
&= \frac{\Omega(r-r_0)\sin\theta}{v_{sw}}\left[1 + \frac{\Omega(r-r_0)\sin\theta}{v_{sw}}\right]^{-1/2}.
\end{aligned}$$

From equation 3.21 it follows that

$$a_r = -\cos\psi$$
$$a_\phi = \frac{\Omega}{v_{sw}}\cos\psi$$
$$\mathcal{L} = -\frac{2}{r}\cos\psi$$

where $\mathcal{L}$ is the linear term which was mentioned in section 3.1.2. Therefore the set of SDE equations for the diffusion free HMF is

$$r(s+ds) = r(s) + \cos\psi ds$$
$$\phi(s+ds) = \phi(s) - \frac{\Omega}{v_{sw}}\cos\psi ds.$$

The combination of the two equations above give

$$\phi = -\frac{\Omega}{v_{sw}}r,$$

which is the Parker spiral. The linear term, $\mathcal{L}$, is solved iteratively by using

$$\alpha(s+ds) = \alpha(s)e^{\mathcal{L}(x(s))ds}, \text{ with } \alpha(s=0) = 1$$

Substituting $\mathcal{L}$ into the above equation yields

$$\alpha(s+ds) = \alpha(s)e^{-\frac{2}{r}\cos\psi ds}. \tag{3.22}$$

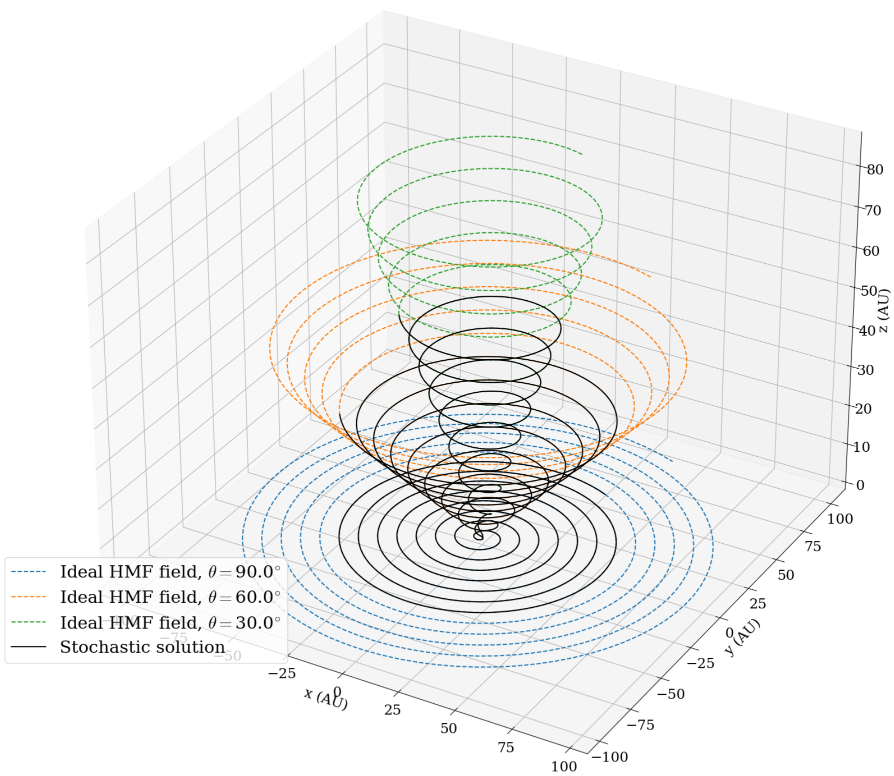

Figure 3.4: Comparison between the ideal Parker spiral and the SDE solution for $\theta = \frac{\pi}{6}$, $\frac{\pi}{3}$, $\frac{\pi}{2}$

Figure 3.4 shows the ideal Parker spiral at three different polar angles. The spiral at $\theta = \frac{\pi}{2}$ remains in the equatorial plane, while the spirals at $\theta = \frac{\pi}{3}$ and $\theta = \frac{\pi}{6}$ are more cone-shaped, with the spiral at $\theta = \frac{\pi}{3}$ having a larger slant angle than that of the spiral at $\theta = \frac{\pi}{6}$. Also shown in figure 3.4 are the SDE solutions for equation 3.21 for $\theta = \frac{\pi}{2}$, $\frac{\pi}{3}$, $\frac{\pi}{6}$. By comparing SDE solutions with the ideal Parker spirals it is clear that the SDE solutions follow the exact same trajectories as the ideal spirals. As such it would seem that the SDE solution yields results that appear to be akin to the Parker spiral. From $\frac{d\alpha}{ds} = \mathcal{L}\alpha$, it follows

$$\begin{aligned}
\frac{d\alpha}{\alpha} &= \mathcal{L}ds \\
\int d\ln\alpha &= -\int \frac{2}{r}\cos\phi ds \\
\int d\ln\alpha &= -\int \frac{2}{r}dr \\
\ln\alpha &= -2\ln r + const. \\
\alpha &= \frac{const.}{r^2} \\
\Rightarrow \alpha &\propto \frac{1}{r^2},
\end{aligned}$$

therefore α solves the probability density along each trajectory and not the magnetic field intensity. Another way to obtain the time-forward stochastic ideal magnetic field is by multiplying equation 3.19 with r^2, i.e.

$$\begin{aligned}
0 &= \frac{\partial f_m}{\partial s} + \underline{\nabla}\cdot(\hat{e}_b f_m) \\
0 &= \frac{\partial f_m}{\partial s} + \frac{1}{r^2}\frac{\partial}{\partial r}\left[r^2 f_m\cos\psi\right] - \frac{1}{r\sin\theta}\frac{\partial}{\partial\phi}\left[f_m\sin\psi\right] \\
0 &= r^2\frac{\partial f_m}{\partial s} + \frac{\partial}{\partial r}\left[r^2 f_m\cos\psi\right] - \frac{\partial}{\partial\phi}\left[\frac{r f_m\sin\psi}{\sin\theta}\right]
\end{aligned}$$

Let $g_m = r^2 f_m$, thus

$$\frac{\partial g_m}{\partial s} = -\frac{\partial}{\partial r}\left[g_m\cos\psi\right] + \frac{\partial}{\partial\phi}\left[\frac{g_m\Omega}{v_{sw}}\cos\psi\right] \tag{3.23}$$

From which it follows

$$\begin{aligned}
a_r &= -\cos\psi \\
a_\phi &= \frac{\Omega}{v_{sw}}\cos\psi.
\end{aligned}$$

Both methods yield the same equations for the integration paths, but to obtain the weight of the solution curves for the second method, which was calculated previously by using $\mathcal{L}$, the density at each point needs to be divided by the square of the radial distance to transform g_m back to f_m.

Time-backwards ideal HMF

The second term of the diffusion free convection–diffusion equation, written out, is

$$\begin{aligned}
\underline{\nabla} \cdot (\hat{e}_b f_m) &= \frac{1}{r^2}\frac{\partial}{\partial r} r^2 f_m \cos\psi - \frac{1}{r\sin\theta}\frac{\partial}{\partial\phi} f_m \sin\psi \\
&= \frac{1}{r^2}\left[r\cos\psi\left(2f_m + r\frac{\partial f_m}{\partial r}\right) + r^2 f_m \frac{\partial\cos\psi}{\partial r}\right] - \frac{1}{r\sin\theta}\left[\sin\psi\frac{\partial f_m}{\partial\phi} + f_m\frac{\partial\sin\psi}{\partial\phi}\right] \\
&= \cos\psi\left(\frac{2}{r}f_m + \frac{\partial f_m}{\partial r}\right) - f_m\frac{\tan^2\psi}{r}\left[1 + \left(\frac{\Omega r\sin\theta}{v_{sw}}\right)^2\right]^{-3/2} - \frac{\Omega}{v_{sw}}\cos\psi\frac{\partial f_m}{\partial\phi},
\end{aligned}$$

which gives

$$\frac{\partial f_m}{\partial s} = \cos\psi\left(\frac{\Omega}{v_{sw}}\frac{\partial f_m}{\partial\phi} - \frac{\partial f_m}{\partial r}\right) - f_m\frac{2+\tan^2\psi}{r\left[1+\tan^2\psi\right]^{3/2}} \tag{3.24}$$

when substituted back into equation 3.19, thus the drift terms and the linear terms for the time-backwards methods are given by

$$\begin{aligned}
a_r &= -\cos\psi \\
a_\phi &= \frac{\Omega}{v_{sw}}\cos\psi
\end{aligned}$$

and

$$\mathcal{L} = -\frac{2+\tan^2\psi}{r\left[1+\tan^2\psi\right]^{3/2}}.$$

Evidently, both equations 3.21 and 3.24 produce the same equations for the integration paths in space. The only difference between the two equations is the linear term. Seeing as how the main method of integration for this study is the time-forwards method, the solving of α for the time-backwards is left as a future endeavour. It is interesting to note that $\mathcal{L} = \underline{\nabla} \cdot \hat{e}_b$ and is thus the inverse of the HMF focusing length.

3.2.3 Added diffusion

The previously neglected term in equation 3.13 contains the diffusion tensor, which is usually defined as

$$\mathbf{D} = \begin{bmatrix} D_{||} & 0 & 0 \\ 0 & D_{\perp\theta} & 0 \\ 0 & 0 & D_{\perp r} \end{bmatrix}$$

in terms of HMF aligned coordinates while assuming a Parker field, with the first axis ($\hat{e}_{||}$) parallel to the mean HMF in the $r\phi$-plane, the second axis ($\hat{e}_1$) perpendicular to $\hat{e}_{||}$ and the last axis ($\hat{e}_2$) lying in the $r\phi$-plane. The coordinate system is related to the spherical coordinate as

$$\begin{aligned}
\hat{e}_{||} &= \cos\psi\hat{e}_r - \sin\psi\hat{e}_\phi \\
\hat{e}_1 &= \hat{e}_\theta \\
\hat{e}_2 &= \hat{e}_{||} \times \hat{e}_1 \\
&= \sin\psi\hat{e}_r + \cos\psi\hat{e}_\phi
\end{aligned}$$

through the HMF winding angle ψ. Therefore the transformation matrix is given by

$$\mathbf{T} = \begin{bmatrix} \cos\psi & 0 & \sin\psi \\ 0 & 1 & 0 \\ -\sin\psi & 0 & \cos\psi \end{bmatrix}$$

with $\det(\mathbf{T}) = 1$. Meaning that $\mathbf{D}$ can be written in spherical coordinates as

$$\begin{aligned}
\begin{bmatrix} D_{rr} & D_{r\theta} & D_{r\phi} \\ D_{\theta r} & D_{\theta\theta} & D_{\theta\phi} \\ D_{\phi r} & D_{\phi\theta} & D_{\phi\phi} \end{bmatrix} &= \mathbf{T}\,\mathbf{D}\,\mathbf{T}^T \\
&= \begin{bmatrix} \cos\psi & 0 & \sin\psi \\ 0 & 1 & 0 \\ -\sin\psi & 0 & \cos\psi \end{bmatrix} \begin{bmatrix} D_{||} & 0 & 0 \\ 0 & D_{\perp\theta} & 0 \\ 0 & 0 & D_{\perp r} \end{bmatrix} \begin{bmatrix} \cos\psi & 0 & -\sin\psi \\ 0 & 1 & 0 \\ \sin\psi & 0 & \cos\psi \end{bmatrix} \\
&= \begin{bmatrix} D_{||}\cos^2\psi + D_{\perp r}\sin^2\psi & 0 & (D_{\perp r} - D_{||})\cos\psi\sin\psi \\ 0 & D_{\perp\theta} & 0 \\ (D_{\perp r} - D_{||})\cos\psi\sin\psi & 0 & D_{||}\sin^2\psi + D_{\perp r}\cos^2\psi \end{bmatrix} \quad (3.25)
\end{aligned}$$

where $\mathbf{T}^T$ is the transpose of the transformation matrix.

Time-forwards formulation with added diffusion

The dot product of the diffusion tensor in spherical coordinates, $\mathbf{D} = \begin{bmatrix} D_{rr} & D_{r\theta} & D_{r\phi} \\ D_{\theta r} & D_{\theta\theta} & D_{\theta\phi} \\ D_{\phi r} & D_{\phi\theta} & D_{\phi\phi} \end{bmatrix}$, and the gradient of f_m, $\underline{\nabla} f_m = \left[\frac{\partial f_m}{\partial r}, \frac{1}{r}\frac{\partial f_m}{\partial \theta}, \frac{1}{r\sin\theta}\frac{\partial f_m}{\partial \phi}\right]$, yields

$$\mathbf{D} \cdot \underline{\nabla} f_m = \begin{bmatrix} D_{rr}\frac{\partial f_m}{\partial r} + \frac{D_{r\theta}}{r}\frac{\partial f_m}{\partial \theta} + \frac{D_{r\phi}}{r\sin\theta}\frac{\partial f_m}{\partial \phi} \\ D_{\theta r}\frac{\partial f_m}{\partial r} + \frac{D_{\theta\theta}}{r}\frac{\partial f_m}{\partial \theta} + \frac{D_{\theta\phi}}{r\sin\theta}\frac{\partial f_m}{\partial \phi} \\ D_{\phi r}\frac{\partial f_m}{\partial r} + \frac{D_{\phi\theta}}{r}\frac{\partial f_m}{\partial \theta} + \frac{D_{\phi\phi}}{r\sin\theta}\frac{\partial f_m}{\partial \phi} \end{bmatrix}$$

from which it follows

$$
\begin{aligned}
\underline{\nabla}\cdot(\mathbf{D}\cdot f_m) = &\frac{\partial}{\partial r}\left(\left[\frac{2D_{rr}}{r} - \frac{\partial D_{rr}}{\partial r} - \frac{\partial}{\partial \theta}\left(\frac{D_{r\theta}}{r}\right) - \frac{\partial}{\partial \phi}\left(\frac{D_{r\phi}}{r\sin\theta}\right) + \frac{D_{\theta r}}{r}\cot\theta\right] f_m\right) \\
&+ \frac{\partial}{\partial \theta}\left(\left[\frac{2D_{r\theta}+D_{\theta r}}{r^2} - \frac{1}{r}\frac{\partial D_{\theta r}}{\partial r} - \frac{\partial}{\partial \theta}\left(\frac{D_{\theta\theta}}{r^2}\right) + \frac{D_{\theta\theta}}{r^2}\cot\theta\right.\right. \\
&\left.\left. - \frac{\partial}{\partial \phi}\left(\frac{D_{\theta\phi}}{r^2\sin\theta}\right)\right] f_m\right) + \frac{\partial}{\partial \phi}\left(\left[\frac{2D_{r\phi}+D_{\phi r}}{r^2\sin\theta} + \left(\frac{D_{\theta\phi}+D_{\phi\theta}}{r^2\sin\theta}\right)\cot\theta\right.\right. \\
&\left.\left. - \frac{1}{r\sin\theta}\frac{\partial D_{\phi r}}{\partial r} - \frac{1}{r^2\sin\theta}\frac{\partial D_{\phi\theta}}{\partial \theta} - \frac{\partial}{\partial \phi}\left(\frac{D_{\phi\phi}}{r^2\sin^2\theta}\right)\right] f_m\right) \\
&+ \left[\frac{2D_{rr}}{r^2} - \frac{2}{r}\frac{\partial D_{rr}}{\partial r} - \frac{2}{r^2}\frac{\partial D_{r\theta}}{\partial \theta} - \frac{\partial}{\partial \phi}\left(\frac{2D_{r\phi}}{r^2\sin\theta}\right) + \cot\theta\left(\frac{D_{\theta r}}{r^2} - \frac{1}{r}\frac{\partial D_{\theta r}}{\partial r}\right.\right. \\
&\left.\left. - \frac{\partial}{\partial \theta}\left(\frac{D_{\theta\theta}}{r^2}\right) - \frac{\partial}{\partial \phi}\left(\frac{D_{\theta\phi}}{r^2\sin\theta}\right)\right) + \frac{D_{\theta\theta}}{r^2\sin\theta}\right] f_m + \frac{\partial^2}{\partial r^2}\left(D_{rr} f_m\right) \\
&+ \frac{\partial^2}{\partial \theta^2}\left(\frac{D_{\theta\theta}}{r^2} f_m\right) + \frac{\partial^2}{\partial \phi^2}\left(\frac{D_{\phi\phi}}{r^2\sin^2\theta} f_m\right) + \frac{\partial^2}{\partial r\partial\theta}\left(\frac{D_{r\theta}+D_{\theta r}}{r} f_m\right) \\
&+ \frac{\partial^2}{\partial r\partial\phi}\left(\frac{D_{r\phi}+D_{\phi r}}{r\sin\theta} f_m\right) + \frac{\partial^2}{\partial \theta\partial\phi}\left(\frac{D_{\theta\phi}+D_{\phi\theta}}{r^2\sin\theta} f_m\right) \qquad (3.26)
\end{aligned}
$$

combining equation 3.21 and equation 3.26, and substituting equation 3.25 gives

$$
\begin{aligned}
\frac{\partial f_m}{\partial s} = &\frac{\partial}{\partial r}\left(\left[\frac{2D_{rr}}{r} - \frac{\partial}{\partial r}\left(D_{rr}\right) - \cos\psi\right] f_m\right) \\
&+ \frac{\partial}{\partial \theta}\left(\left[-\frac{\partial}{\partial \theta}\left(\frac{D_{\theta\theta}}{r^2}\right) + \frac{D_{\theta\theta}}{r^2}\cot\theta\right] f_m\right) \\
&+ \frac{\partial}{\partial \phi}\left(\left[\frac{3D_{r\phi}}{r^2\sin\theta} - \frac{1}{r\sin\theta}\frac{\partial}{\partial r}\left(D_{r\phi}\right) + \frac{\Omega}{v_{sw}}\cos\psi\right] f_m\right) \\
&+ \left[\frac{2}{r^2}D_\perp\sin^2\psi - \frac{2}{r}\frac{\partial}{\partial r}\left(D_{rr}\right) - \frac{\partial}{\partial \theta}\left(\frac{D_\perp}{r^2}\right)\cot\theta + \frac{D_\perp}{r^2\sin\theta} - \frac{2}{r}\cos\psi\right] f_m \\
&+ \frac{\partial^2}{\partial r^2}\left(D_{rr} f_m\right) + \frac{\partial^2}{\partial \theta^2}\left(\frac{D_{\theta\theta}}{r^2} f_m\right) + \frac{\partial^2}{\partial \phi^2}\left(\frac{D_{\phi\phi}}{r^2\sin^2\theta} f_m\right) \\
&+ \frac{\partial^2}{\partial r\partial\theta}\left(\frac{D_{r\theta}+D_{\theta r}}{r} f_m\right) + \frac{\partial^2}{\partial r\partial\phi}\left(\frac{D_{r\phi}+D_{\phi r}}{r\sin\theta} f_m\right) + \frac{\partial^2}{\partial \theta\partial\phi}\left(\frac{D_{\theta\phi}+D_{\phi\theta}}{r^2\sin\theta} f_m\right).
\end{aligned}
$$

For the purpose of this study it is assumed that $D_{||} = 0$ and that $D_{\perp r} = D_{\perp\theta}$, therefore $D_\perp$ will be used instead of writing $D_{\perp r}$ or $D_{\perp\theta}$, thus the drift and linear terms simplify to

$$
\begin{aligned}
a_r &= \frac{2D_\perp\sin^2\psi}{r} - \frac{\partial}{\partial r}\left(D_\perp\sin^2\psi\right) - \cos\psi \\
&= \frac{2D_\perp\sin^2\psi}{r} - \left(\sin^2\psi\frac{\partial D_\perp}{\partial r} + \frac{2D_\perp}{r}\sin^2\psi\cos^2\psi\right) - \cos\psi \\
&= \sin^2\psi\left[\frac{2D_\perp}{r}\left(sin^2\psi\right) - \frac{\partial D_\perp}{\partial r}\right] - \cos\psi
\end{aligned}
$$

$$
\begin{aligned}
a_\theta &= -\frac{\partial}{\partial \theta}\left(\frac{D_\perp}{r^2}\right) + \frac{D_\perp}{r^2}\cot\theta \\
&= \frac{1}{r^2}\left(D_\perp\cot\theta - \frac{\partial D_\perp}{\partial \theta}\right)
\end{aligned}
$$

$$
\begin{aligned}
a_\phi &= \frac{3D_\perp \cos\psi \sin\psi}{r^2 \sin\theta} - \frac{1}{r\sin\theta}\frac{\partial}{\partial r}\left(D_\perp \cos\psi\sin\psi\right) + \frac{\Omega}{v_{sw}}\cos\psi \\
&= \frac{3D_\perp \cos\psi \sin\psi}{r^2 \sin\theta} - \frac{\cos\psi\sin\psi}{r\sin\theta}\left[\frac{\partial D_\perp}{\partial r} + \frac{D_\perp}{r}\left(\cos^2\psi - \sin^\psi\right)\right] + \frac{\Omega}{v_{sw}}\cos\psi \\
&= \frac{\cos\psi\sin\psi}{r\sin\theta}\left[\frac{D_\perp}{r}\left(3 - \cos^2\psi + \sin^2\psi\right) - \frac{\partial D_\perp}{\partial r}\right] + \frac{\Omega}{v_{sw}}\cos\psi
\end{aligned}
$$

$$
\begin{aligned}
\mathcal{L} &= \frac{2}{r^2}D_\perp\sin^2\psi - \frac{2}{r}\frac{\partial}{\partial r}\left(D_\perp\sin^2\psi\right) - \frac{\partial}{\partial\theta}\left(\frac{D_\perp}{r^2}\right)\cot\theta + \frac{D_\perp}{r^2\sin\theta} - \frac{2}{r}\cos\psi \\
&= \frac{1}{r}\left[\sin^2\psi\left(\frac{2D_\perp}{r} - \frac{2D_\perp}{r}\cos^2\psi - 2\frac{\partial D_\perp}{\partial r}\right) - \frac{\cot\theta}{r}\frac{\partial D_\perp}{\partial\theta} + \frac{D_\perp}{r\sin\theta} - 2\cos\psi\right] \\
&= \frac{1}{r^2}\left[2\left(\sin^2\psi\left(D_\perp\sin^2\psi - r\frac{\partial D_\perp}{\partial r}\right) - r\cos\psi\right) - \cot\theta + \frac{D_\perp}{\sin\theta}\right]
\end{aligned}
$$

with

$$
\Rightarrow \mathbf{C} = \begin{bmatrix} D_{rr} & \frac{D_{r\theta}}{r} & \frac{D_{r\phi}}{r\sin\theta} \\ \frac{D_{\theta r}}{r} & \frac{D_{\theta\theta}}{r^2} & \frac{D_{\theta\phi}}{r^2\sin\theta} \\ \frac{D_{\phi r}}{r\sin\theta} & \frac{D_{\phi\theta}}{r^2\sin\theta} & \frac{D_{\phi\phi}}{r^2\sin^2\theta} \end{bmatrix}.
$$

To calculate $\mathbf{b}$, the square root of $\mathbf{C}$ is needed since $\mathbf{C} = \mathbf{b}\cdot\mathbf{b}^T$. Let $\mathbf{b}$ be in the form $\mathbf{b} = \begin{bmatrix} b_{xx} & b_{xy} & b_{xz} \\ 0 & b_{yy} & b_{yz} \\ 0 & 0 & b_{zz} \end{bmatrix}$, through a few simple steps of algebra

$$
\mathbf{b} = \sqrt{2}
\begin{bmatrix}
\sqrt{\frac{D_{rr}D_{\theta\phi}^2 - D_{rr}D_{\theta\theta}D_{\phi\phi} - 2D_{r\phi}D_{\theta\phi}D_{r\theta} + D_{r\theta}^2 D_{\phi\phi} + D_{r\phi}^2 D_{\theta\theta}}{D_{\theta\phi}^2 - D_{\theta\theta}D_{\phi\phi}}} & \frac{D_{r\phi}D_{\theta\phi} - D_{r\theta}D_{\phi\phi}}{D_{\theta\phi}^2 - D_{\theta\theta}D_{\phi\phi}}\sqrt{D_{\theta\theta} - \frac{D_{\theta\phi}^2}{D_{\phi\phi}}} & \frac{D_{r\phi}}{\sqrt{D_{\phi\phi}}} \\
0 & \frac{1}{r}\sqrt{D_{\theta\theta} - \frac{D_{\theta\phi}^2}{D_{\phi\phi}}} & \frac{D_{\theta\phi}}{r\sqrt{D_{\phi\phi}}} \\
0 & 0 & \frac{\sqrt{D_{\phi\phi}}}{r\sin\theta}
\end{bmatrix}
$$

is obtained, which reduces to

$$
\mathbf{b} = \sqrt{2}\begin{bmatrix} 0 & 0 & \sqrt{D_\perp}\sin\psi \\ 0 & \frac{1}{r}\sqrt{D_\perp} & 0 \\ 0 & 0 & \frac{\sqrt{D_\perp}\cos\psi}{r\sin\theta} \end{bmatrix},
$$

when assuming a Parker field and $D_{\|} = 0$, therefore

$$
\begin{aligned}
\mathbf{b} \cdot d\underline{W} &= \sqrt{2} \begin{bmatrix} b_{rr} & b_{r\theta} & b_{r\phi} \\ b_{\theta r} & b_{\theta\theta} & b_{\theta\phi} \\ b_{\phi r} & b_{\phi\theta} & b_{\phi\phi} \end{bmatrix} \begin{bmatrix} dW_r \\ dW_\theta \\ dW_\phi \end{bmatrix} \\
&= \sqrt{2} \begin{bmatrix} b_{r\phi} dW_\phi \\ b_{\theta\theta} dW_\theta \\ b_{\phi\phi} dW_\phi \end{bmatrix} \\
&= \sqrt{2} \begin{bmatrix} \sqrt{D_\perp} \sin\psi dW_\phi \\ \\ \frac{1}{r}\sqrt{D_\perp} dW_\theta \\ \\ \frac{\sqrt{D_\perp}\cos\psi}{r\sin\theta} dW_\phi \end{bmatrix}
\end{aligned}
\tag{3.27}
$$

With $dW = [dW_r, dW_\theta, dW_\phi]$ representing the multidimensional Wiener process. As an alternative, the same method utilized to get equation 3.23 can also be used to obtain

$$
\begin{aligned}
\frac{\partial g_m}{\partial s} = &\frac{\partial^2}{\partial r^2}(D_{rr} g_m) + \frac{\partial^2}{\partial \theta^2}\left(\frac{D_{\theta\theta}}{r^2} g_m\right) + \frac{\partial^2}{\partial \phi^2}\left(\frac{D_{\phi\phi}}{r^2 \sin^2\theta} g_m\right) + 2\frac{\partial^2}{\partial r \partial \phi}\left(\frac{D_{r\phi}}{r\sin\theta} g_m\right) \\
&- \frac{\partial}{\partial r}\left(\left[\frac{\partial D_{rr}}{\partial r} + \frac{2}{r} D_{rr} + \cos\psi\right] g_m\right) \\
&- \frac{\partial}{\partial \theta}\left(\left[\frac{\partial}{\partial \theta}\left(\frac{D_{\theta\theta}}{r^2}\right) + \frac{D_{\theta\theta}}{r^2}\cot\theta\right] g_m\right) \\
&- \frac{\partial}{\partial \phi}\left(\left[\frac{D_{\phi r}}{r^2\sin\theta} + \frac{1}{r\sin\theta}\frac{\partial D_{\phi r}}{\partial r} - \frac{\Omega}{v_{sw}}\cos\psi\right] g_m\right)
\end{aligned}
\tag{3.28}
$$

where $g_m = f_m r^2 \sin\theta$. Consequently, the tensor $\mathbf{C}$ stays the same, which means that $\mathbf{b}$ remains unchanged as well, while

$$
\begin{aligned}
a_r &= -\left[\frac{\partial}{\partial r}\left(D_\perp \sin^2\psi\right) + \frac{2}{r} D_\perp \sin^2\psi + \cos\psi\right] \\
a_\theta &= -\left[\frac{1}{r^2}\frac{\partial}{\partial \theta}(D_\perp) + \frac{D_\perp}{r^2}\cot\theta\right] \\
a_\phi &= -\left[\frac{D_\perp \cos\psi \sin\psi}{r^2\sin\theta} + \frac{1}{r\sin\theta}\frac{\partial}{\partial r}(D_\perp \cos\psi\sin\psi) - \frac{\Omega}{v_{sw}}\cos\psi\right].
\end{aligned}
$$

Seeing that the second method used to obtain the time-forwards equation yields a result free of a linear term containing diffusion coefficients, it should be much simpler to use in the simulations. The set of SDEs therefore becomes

$$
\begin{aligned}
dr &= a_r \cdot ds + b_{r\phi} \cdot dW_\phi \\
d\theta &= a_\theta \cdot ds + b_{\theta\theta} \cdot dW_\theta \\
d\phi &= a_\phi \cdot ds + b_{\phi\phi} \cdot dW_\phi,
\end{aligned}
$$

considering that equation 3.28 is without a linear term it, follows that the trajectory density at each point needs to be divided by $r^2 \sin\theta$ to then obtain the trajectory weight. More often than not, cosmic ray modulation models assume a boundary condition for small values of r, due to the fact that some of the heliospheric parameters, such as the HMF, are undefined at $r = 0$ or behave differently within certain boundaries such as the source surface. Therefore a reflecting inner boundary condition is needed at $r_{min} \ll 1$AU, which means that any trajectory moving past the inner boundary is reflected back by returning the trajectory to the computational domain. The reflecting inner boundary condition used in the simulation is given by

$$r < r_{min} : r \to 2r_{min} - r.$$

Furthermore, the angular position of the trajectories has to be renormalized such that $\phi \in [0, 2\pi]$ and $\theta \in [0, \pi]$, therefore the following conditions are needed

$$\begin{aligned}
\phi < 0 &: \phi \to \phi + 2\pi \\
\phi > 2\pi &: \phi \to \phi - 2\pi \\
\theta < 0 &: \theta \to |\theta|\,; \phi \to \phi \pm \pi \\
\theta > 0 &: \theta \to 2\pi - \theta; \phi \to \phi \pm \pi.
\end{aligned}$$

Diffusion coefficient

Finally all that is needed to finalise the FLRW model is to determine the diffusion coefficient $D_\perp$. For the purpose of this study it is assumed that $D_\perp = K_{FL}$, the field-line diffusion coefficient, is given by

$$K_{FL} = \frac{\sqrt{\frac{\delta B^2}{2}}}{B}\lambda_u, \tag{3.29}$$

as defined by Matthaeus et al. (1995, 2007). $\delta B^2 = 12.5\left(\frac{r}{r_e}\right)^{-2.4}$ (nT^2) denotes the variance (see, e.g. Smith et al., 2006a) and B the magnetic field intensity given by equation 3.14. The ultrascale is given by

$$\lambda_u = \sqrt{\frac{K_{out}^{-2}(\frac{q+1}{2q-2}) + K_{2D}^{-2}(\frac{1-\nu}{2\nu+2})}{\frac{1}{q+1} + \ln(\frac{K_{2D}}{K_{out}}) + \frac{1}{\nu-1}}}.$$

Here $\nu = \frac{5}{3}$ and $q = 3$ represent the spectral indices of the inertial and dissipation ranges of the 2D turbulence spectrum respectively, $K_{out} = \frac{1}{12.5(0.0074)}\left(\frac{r_e}{r}\right)^{1/2}$ (AU^{-1}) is given by one over the outerscale and $K_{2D} = \frac{1}{0.0074}\left(\frac{r_e}{r}\right)^{1/2}$ (AU^{-1}) is given by one over the turnover scale (Smith et al., 2001; Matthaeus et al., 2007; Weygand et al., 2011; Engelbrecht and Burger, 2015; Cuesta et al., 2022). Substituting δB^2, B, λ_u, K_{out} and K_{2D} into equation

3.29 and then deriving equation 3.29 in terms of radius yields

$$\begin{aligned}
\frac{\partial}{\partial r}K_{FL} &= \lambda_u \frac{\partial}{\partial r}\frac{\sqrt{\frac{\delta B^2}{2}}}{B} + \frac{\sqrt{\frac{\delta B^2}{2}}}{B}\frac{\partial}{\partial r}\lambda_u \\
&= \lambda_u \left[\frac{1}{B}\frac{\partial}{\partial r}\sqrt{\frac{\delta B^2}{2}} + \sqrt{\frac{\delta B^2}{2}}\frac{\partial}{\partial r}\frac{1}{B}\right] + \frac{\sqrt{\frac{\delta B^2}{2}}}{B}\frac{\partial}{\partial r}\sqrt{\frac{K_{out}^{-2}(\frac{q+1}{2q-2}) + K_{2D}^{-2}(\frac{1-\nu}{2\nu+2})}{\frac{1}{q+1} + \ln(\frac{K_{2D}}{K_{out}}) + \frac{1}{\nu-1}}} \\
&= \lambda_u \left[-\frac{3r_e^{1.2}}{Br^{2.2}} + \sqrt{\frac{\delta B^2}{2}}\frac{2+\tan^2\psi}{Br\left[1+\tan^2\psi\right]}\right] + \frac{1}{2r}\frac{\sqrt{\frac{\delta B^2}{2}}}{B}\lambda_u \\
&= -K_{FL}\left[\frac{3r_e^{1.2}}{r^{2.2}}\left[\frac{\delta B^2}{2}\right]^{-1/2} - \frac{2+\tan^2\psi}{r\left[1+\tan^2\psi\right]}\right] + \frac{K_{FL}}{2r}.
\end{aligned}$$

Similarly, the derivative of equation 3.29 with respect to θ is calculated as

$$\begin{aligned}
\frac{\partial}{\partial\theta}K_{FL} &= \frac{\partial}{\partial\theta}\lambda_u\frac{\sqrt{\frac{\delta B^2}{2}}}{B} \\
&= \lambda_u\sqrt{\frac{\delta B^2}{2}}\frac{\partial}{\partial\theta}B^{-1} \\
&= -\frac{\lambda_u}{B}\sqrt{\frac{\delta B^2}{2}}\sin^2\psi\cot\theta \\
&= -K_{FL}\sin^2\psi\cot\theta.
\end{aligned}$$

3.3 Summary

Section 3.1.2 introduced stochastic differential equations (SDEs) as a method with which to solve the Fokker-Planck type equations. It was shown that Fokker-Planck type equations are equivalent to SDEs and that each n-dimensional Fokker-Planck equation can be transformed into a set of $n-1$ first order SDE equations by using either the forward or backward Kolmogorov equation, in such a way that the field-line diffusion can be modelled by either the Fokker-Planck or SDE formulation. The relevant set of SDEs describing the field-line diffusion was derived from the focused transport equation (FTE) and the numerical implementation of the resulting SDE-based field-line random walk model was discussed. The results obtained from time-forwards model with the added diffusion and the implications thereof will be discussed in the following chapter.

Chapter 4

A Random Walk Model for the Heliospheric Magnetic Field

The purpose of chapter 4 is to apply the stochastic field-line random walk model, derived in chapter 3, to the Parker HMF by comparing the simulation results with analytical approximations as well as published numerical models. First, a reference scenario, which utilizes the diffusion coefficient used in section 3.2.3, is established by determining the paths along which the probability distribution is calculated. The density of the paths throughout a specified grid is then calculated. The calculated probability distributions as functions of the azimuthal and polar angles, obtained at different radial distance values, are compared to a Gaussian fit. The standard deviations of the probability distribution as functions of the azimuthal and polar angles are compared to a theoretical approximation, while the mean values of the probability distribution in terms of the azimuthal and polar angles are compared to that of the Parker spiral in the equatorial plane. The probability distribution mean values in terms of the azimuthal and polar angles are then used to determine the most likely path a magnetic field-line would follow. After a reference scenario has been established, the most likely path is estimated for both larger and smaller diffusion coefficients respectively and then once again compared to the Parker spiral.

4.1 Construction of a Reference Scenario

For the construction of a reference scenario, the simulation is performed with a solar wind speed of $400\,\mathrm{km/s}$ and a solar rotation rate of $14.1844^\circ/\mathrm{day}$ (Mumford et al., 2025). The diffusion coefficient, given by equation 3.29 in section 3.2.3, was additionally utilized. The simulation ran for 10000 random walks, where the radial distance (r), azimuthal angle (ϕ), polar angle (θ) and probability distribution were calculated for every step along the corresponding random walk. A single random walk consists of 10000 steps with a step size of $0.0005\,\mathrm{AU}$. A value of $5\,\mathrm{nT}$ was used for the magnetic field intensity at the Earth, or at $1\,\mathrm{AU}$. Substituting this magnetic field intensity and the radial distances of $r = 1\,\mathrm{AU}$ and

$r_0 = 0.04\,\mathrm{AU}$ into

$$B = B_0 \left(\frac{r_0}{r}\right)^2 \sqrt{1 + \tan^2\psi}$$

yielded the starting magnetic field intensity, B_0, at the point of origin, r_0. The approximate value for B_0 was calculated to be $\sim 2132\,\mathrm{nT}$. The red line in figure 4.1 shows the Parker spiral for a single field-line which starts at an azimuthal angle of $\phi = \pi$, a polar angle of $\theta = \frac{\pi}{2}$ and radius of $r_0 = 0.04\,\mathrm{AU}$. A starting radius of 0.04 AU is used since it is the theoretical lower bound of the source surface (Smith and Bieber, 1991; Chhiber et al., 2024). Also shown in figure 4.1 are the simulated results for the first 100 random walks.

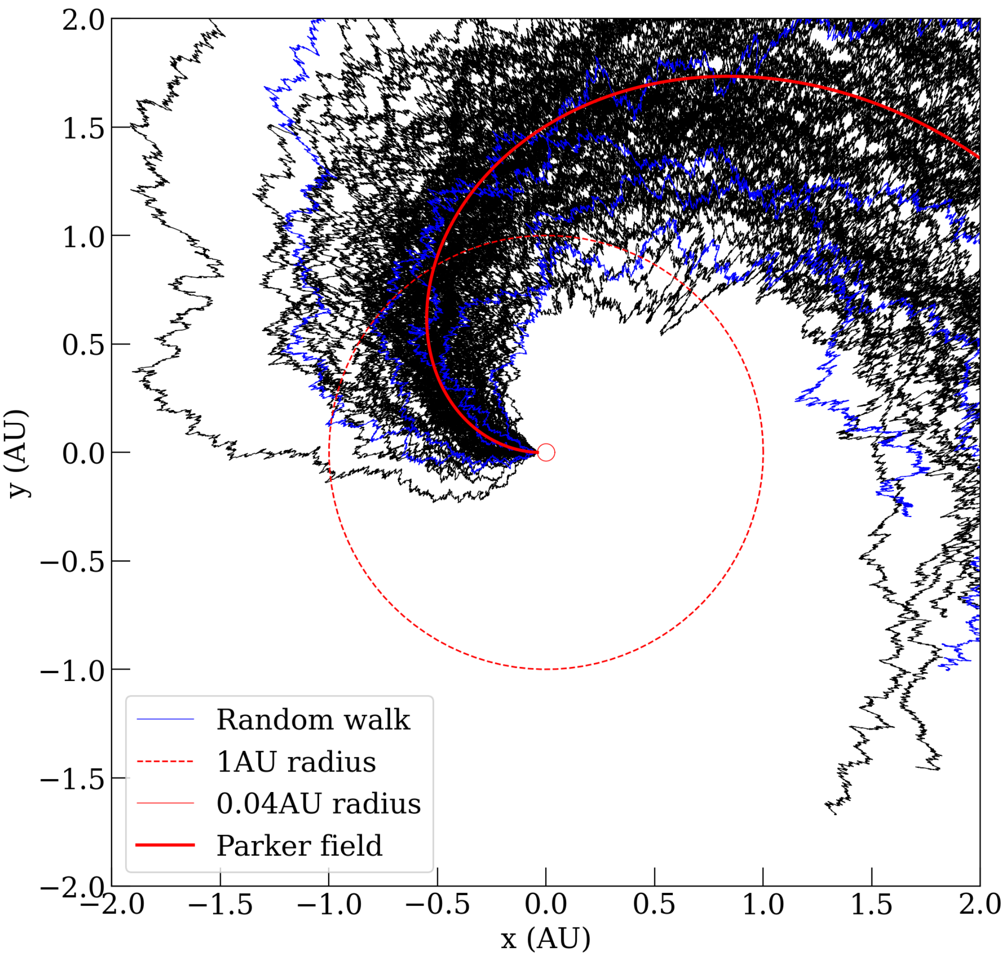

Figure 4.1: 2D profile for 100 FISC-lines (solid black and blue lines), along with the Parker spiral (thick solid red line), the 1 AU radius (dashed red line) and the theoretical lower bound of the source surface (thin solid red line).

Studying figure 4.1, it is clear that the results obtained from the simulation are not magnetic field-lines, since a magnetic field has to be a solenoidal vector field according to Gauss' law for magnetism, and none of the displayed lines meet this criteria. In this turbulence description, the magnetic field-lines are stochastic curves, meaning these lines need to be described through the use of methods employed in statistical physics. For this reason, it is not possible to compute singular field-lines from the statistical description here (Shalchi, 2019). The computed lines are rather solution curves along which the probability distribution is calculated. For simplification, these solution curves will be referred to as field intensity solution curve lines from now on, or FISC-lines for short. The reason for displaying only the first 100 simulated FISC-lines in figure 4.1 is to better depict the stochastic nature of each line. Five of the FISC-lines are shown using blue instead of black to highlight the variation in the paths. The FISC-lines, all starting at the same point of origin as the Parker spiral, immediately start to spread out and diffuse away from the Parker spiral as the radial distance away from the Sun increases. While most FISC-lines remain relatively close to and around the Parker spiral, or start with a large deviation but later return to the area around the Parker spiral, there are lines which tend to drift away more and more as the FISC-line length grows larger. Upon closer inspection of figure 4.1 it can be noted that the jumps in the FISC-lines stay relatively small while close to the point of origin and become larger as the radial distance increases. This is to be expected since the diffusion coefficient is given by

$$D_\perp = \lambda_u \sqrt{\frac{\delta B^2}{2}} \Big/ B,$$

where the HMF intensity (B), the variance ($\sqrt{\frac{\delta B^2}{2}}$) and the ultrascale ($\lambda_u$) are functions of radial distance, leading to a perpendicular diffusion coefficient ($D_\perp$) that has a radial dependence, as can be seen from figures 4.2 and 4.3.

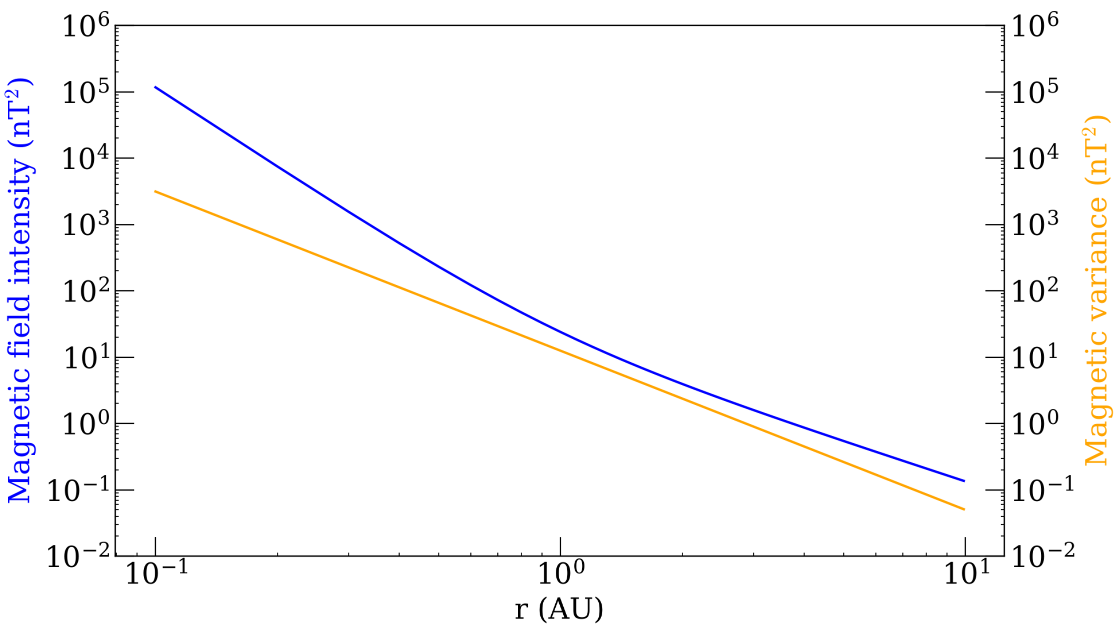

Figure 4.2: The square of the magnetic field intensity (left-hand y-axis) and the magnetic variance (right-hand y-axis) displayed as a function of radial distance.

Figure 4.2 depicts both the square of the HMF intensity and the magnetic variance on opposite y-axes as functions of radial distance. From the figure it can be seen that the magnetic variance decreases as a power law with a spectral index of -2.4, while the HMF intensity decreases with a greater spectral index value while the radial distance is less than 1 AU and with a lesser spectral index value for radial distance values greater than 1 AU. Figure 4.3 shows the ultrascale and the perpendicular diffusion coefficient on opposite y-axes as functions of radial distance. The ultrascale increases increases as a power law with a spectral index of $\frac{1}{2}$ with the increase of radial distance, while the perpendicular diffusion coefficient has a power law decrease.

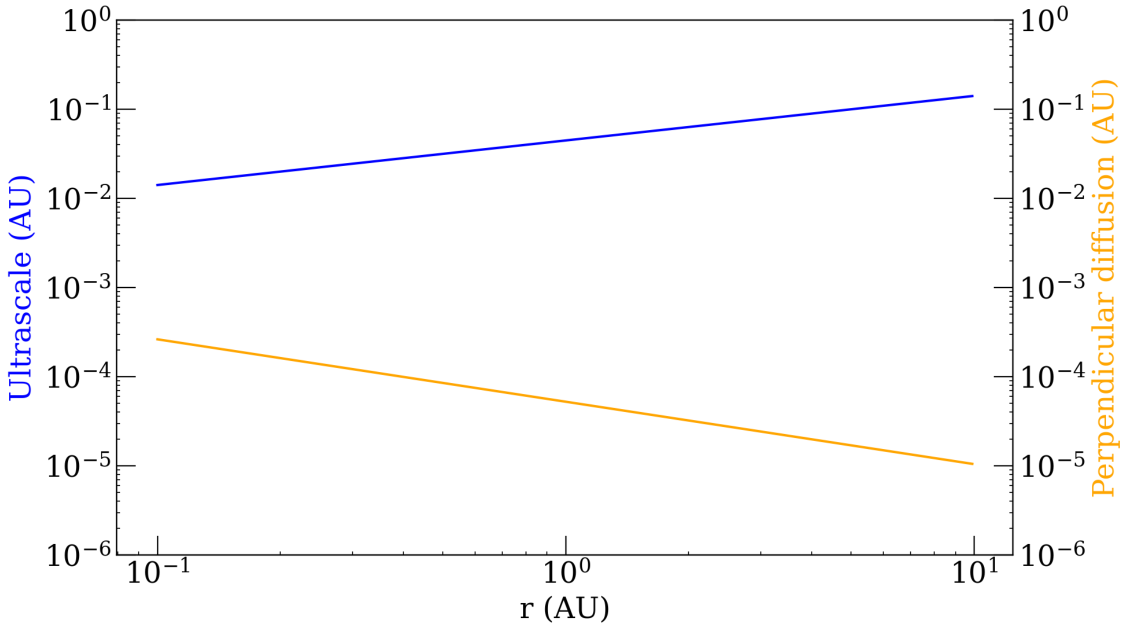

Figure 4.3: The ultrascale (left-hand y-axis) and the perpendicular diffusion coefficient (right-hand y-axis) dipicted as a function of radial distance.

Figure 4.4 displays the first 50 random walks, which were also shown in figure 4.1, in a 3D-environment. The purpose of figure 4.4 is to highlight that there is a change in the θ component of the FISC-lines as well and not only in the ϕ component, meaning that the FISC-lines will move around in the z-axis as well and not just remain within the equatorial plane the way the Parker spiral does. Along with the FISC-lines, the starting radius of 0.04 AU, the 1 AU radius and the Parker spiral are displayed as well. The FISC-lines once again vary between staying close to the Parker spiral and straying away from the spiral, similar to the deviations of the FISC-lines along the ϕ direction. According to the top down view in figure 4.1 the FISC-lines appear to be constantly moving to larger radial distances, figure 4.4 shows this not to be the case. Within figure 4.4 there are FISC-lines which possess little to no movement in the x- and y-directions, while showing movements mostly in the z-direction. Another feature not shown in 4.1 are areas where the FISC-lines continuously jump around the same point for several steps, causing them to cluster together. This type of clustering can vary between only a few jumps to a great number of jumps. A small clustering event can be seen at the top of figure 4.4, at about $x = 0$, $y = 3$ and $z = 2$.

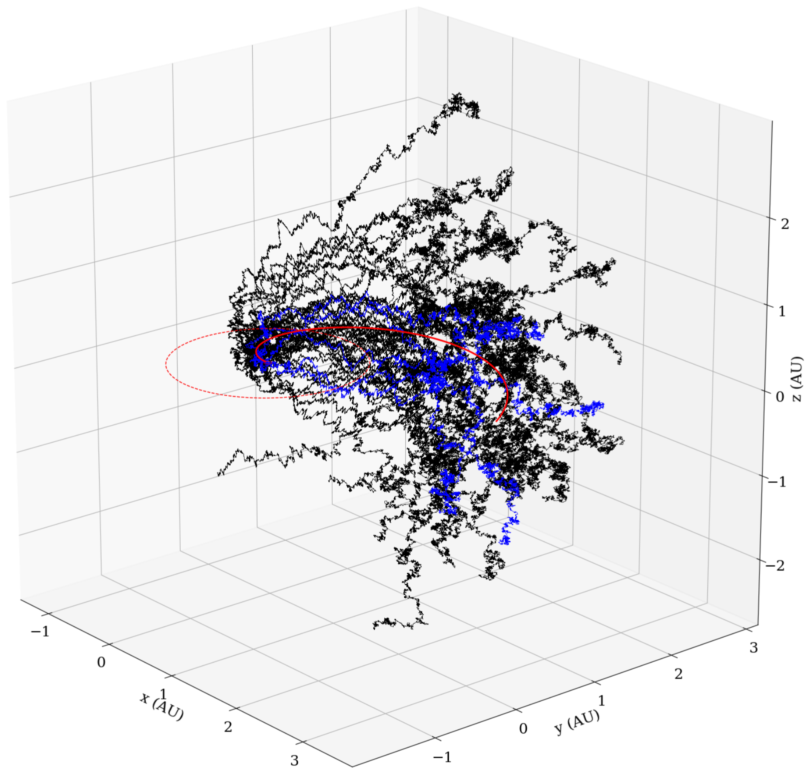

Figure 4.4: 50 FISC-lines (solid black and blue lines) compared to the Parker spiral (thick solid red line) in a 3D projection; the 1 AU radius (dashed red line) and theoretical lower bound of the source surface (solid thin red line) are shown as well.

For figure 4.5 the respective x- and y-coordinates of each individual FISC-line are established for every step along the FISC-line, these coordinates are then used to determine the position of the FISC-lines on a 2D grid. The grid ranges from -2 AU to 2 AU with intervals of 0.02 AU along both the x- and y-axes. If a FISC-line is found to be passing through any given interval within the grid, it is noted, tallied up along with the rest of the curves passing through the interval and then displayed in figure 4.5 using a density map. Here the particle weight is not considered and each FISC-line contributes equally to the distribution. The colour of an interval represents the density of FISC-lines within said interval, with blue representing a lower density and red a higher density. If there is no FISC-line to be found in an interval, the interval remains colourless. Shown in the figure once more is the Parker spiral and the 1 AU and 0.04 AU radii. In comparison to figure 4.1, figure 4.5 distinctly illustrates that the density of FISC-lines is higher around the Parker spiral and decreases further from Parker spiral. Moreover, the density around the Parker spiral decreases as the radial distance increases due to the evolution and spreading of the FISC-lines with radial distance. By observing the displayed density of FISC-lines, it can be assumed that the probability distribution will form Gaussian distribution if correctly sampled. It can also be speculated that the Gaussian distribution will be quite narrow close to the point of origin, and wider at greater distances.

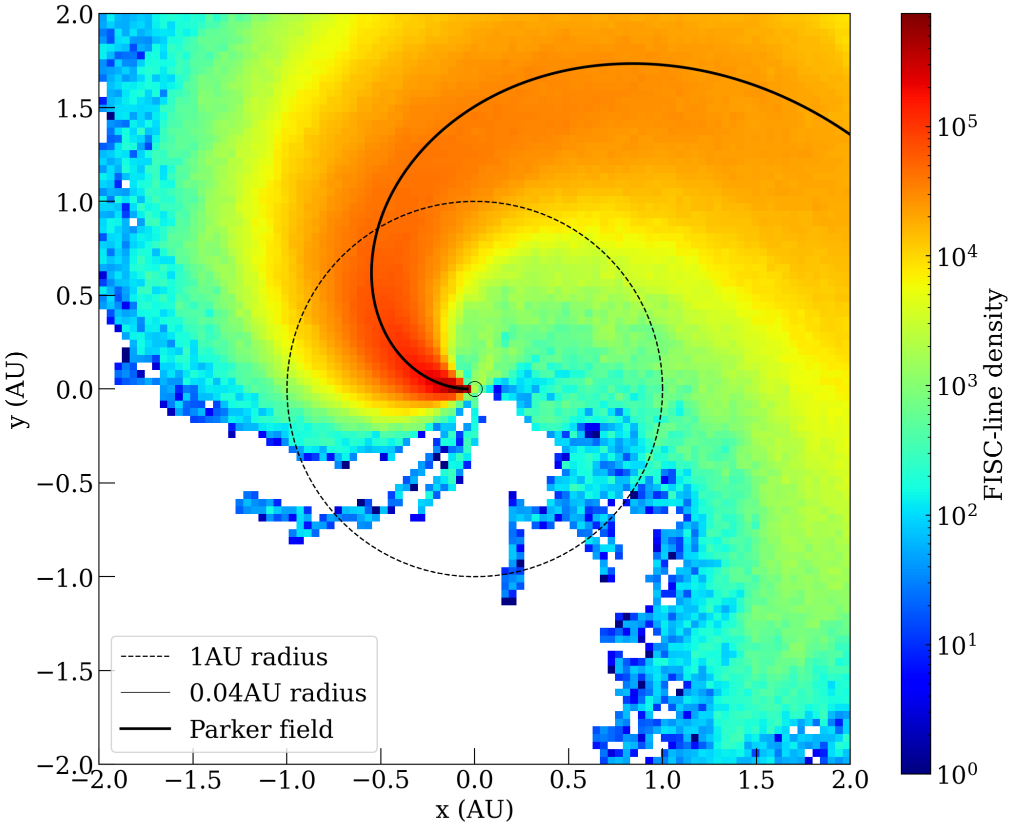

Figure 4.5: Density map of the 2D profile of the FISC-lines, alongside the Parker spiral (thicker solid black line), the 1 AU radius (dashed black line) and the theoretical lower bound of the source surface (thin solid black line).

Figures 4.6a and 4.6b show the probability distribution in terms of ϕ and θ values, determined from the SDE solution, compared to Gaussian fits of the probability distribution as a function of ϕ and θ respectively. The Gaussian fits are created through the use of the SciPy python library and the programming function *scipy.optimize.curve_fit* (Virtanen et al., 2020), which in turn utilizes non-linear least squares to fit a mathematical function, f, to data. The programming function takes a mathematical function, the independent variable and dependent variable data set and finally an initial guess for the parameters used in f. For this particular instance the mathematical function is given by

$$f = a \cdot e^{-(x-x_0)^2/2\sigma^2}$$

where x is the independent variable over which the data set is measured, x_0 is the average x-value, σ is the standard deviation and a is the probability distribution at x_0. The initial guess value for x_0 is given by the mean of the probability distribution, which is calculated using

$$\bar{x} = \frac{\sum_i^N (\rho_i \cdot x)}{\sum_i^N \rho_i}$$

with N being the number of bins, x the bin value and ρ_i the probability distribution. The initial guess for the standard deviation of $\overline{x}$ is calculated using

$$\sigma = \sqrt{\frac{\sum_{i}^{N} \rho_i \cdot (x - \overline{x})^2}{\sum_{i}^{N} \rho_i}}$$

and the initial guess for a is the maximum ρ value. For simplification the mean value for the probability distribution as a function of ϕ and θ is denoted as $\overline{\rho}_\phi$ and $\overline{\rho}_\theta$ respectively, while the standard deviation on the mean value of the probability distribution will be denoted by σ_ϕ for the distribution as a function of ϕ and by σ_θ for the distribution as a function of θ.

A distribution is created by determining where each individual FISC-line crosses the specified radius. Then, instead of counting the amount of FISC-lines in each interval of figure 4.5, the calculated probability distribution at that point is summed together for FISC-lines which possess similar ϕ values for figure 4.6a and similar θ values for figure 4.6b and then displayed as histograms. Each figure shows three distributions obtained at different radial distances. The first distribution is obtained at a radial distance of 0.1 AU, the second at a radial distance of 0.5 AU and the third at a radial distance of 1 AU. Evidently, the SDE solution possesses a very clear Gaussian shape. From the figures it can be inferred that the probability distribution is narrower while close to the Sun and spreads out as the radial distance increases; additionally, the probability distribution spreads out faster at smaller radial distances, but the rate of increase slows down as the radial distance increases. Furthermore, σ increases with increasing radial distance, which means that the corresponding ranges for the ϕ and θ values also increase with increasing radial distance. An obvious difference between figures 4.6a and 4.6b is that the distributions in figure 4.6b remain around the same $\overline{\rho}_\theta$ value, while the $\overline{\rho}_\phi$ value for the distributions in figure 4.6a shifts towards the left as the radial distance increases. This is due to way each data set is sampled which causes the $\overline{\rho}_\phi$ values to roughly follow the Parker spiral curve. As stated previously, each data set is sampled at set radial distances, meaning that the unit vector $\hat{e}_b$, which denotes the direction of the Parker spiral, slowly starts to point away from the direction in which $\hat{e}_r$, the radial component unit vector, points. At small enough radial distances both $\hat{e}_b$ and $\hat{e}_r$ point in the same direction, which means that the obtained $\overline{\rho}_\phi$ will be similar to the starting ϕ value. However, as the radial distance increases the $\overline{\rho}_\phi$ values tend to shift away from the starting ϕ value. As shown in section 3.2.1, there is no change in the θ values of the Parker spiral; clearly this implies that whatever the radial distance, the θ values obtained from the FISC-lines will always show a symmetrical diffusion. Consequently all of the θ distributions will have a $\overline{\rho}_\theta$ value near the starting polar angle.

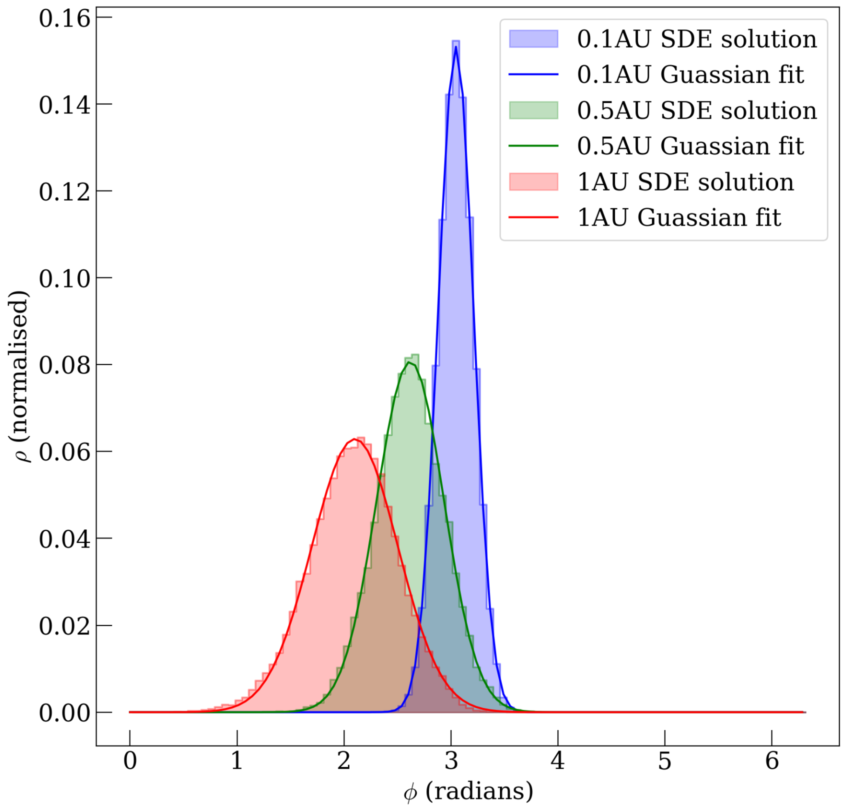

(a)

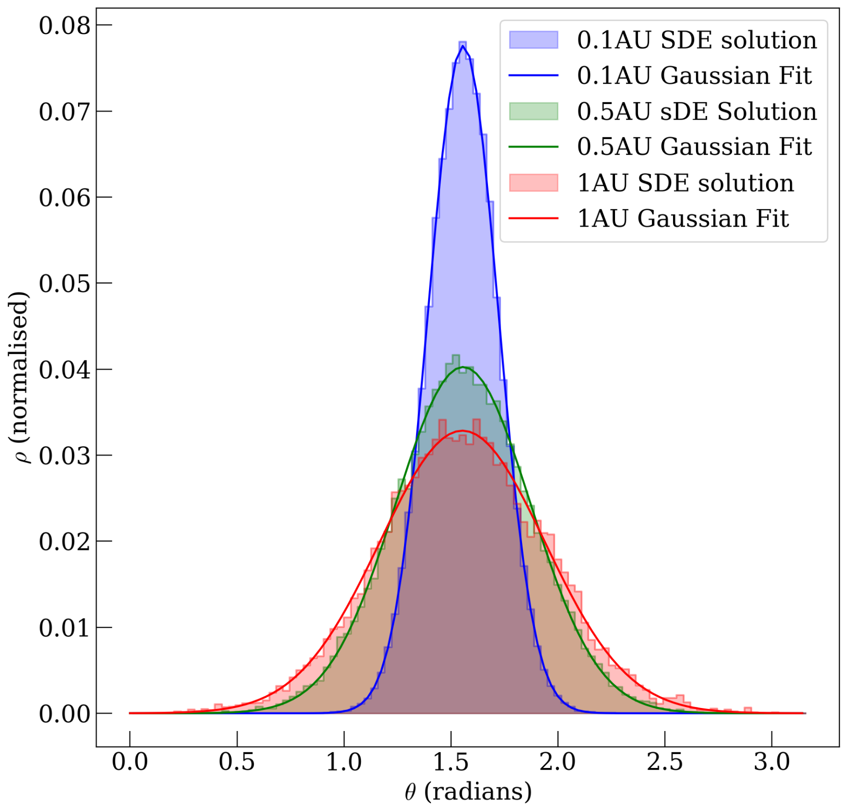

(b)

Figure 4.6: Distribution of the probability distribution as a function of ϕ (panel a) and θ (panel b) values compared to a Gaussian fit at radial distances 0.1 AU (blue), 0.5 AU (green) and 1 AU (red) from the Sun.

By calculating $\overline{\rho}_\phi$ and $\overline{\rho}_\theta$ at regular radial distance intervals, it becomes possible to estimate a path which a magnetic field-line is most likely to follow. The top panel in figure 4.7 portrays the σ_ϕ and σ_θ values, as calculated by the Gaussian fits, at every 0.1 AU interval up to 1.2 AU, compared to a theoretical solution for the standard deviation obtained from Bian et al. (2024). The theoretical solution is given by

$$\sigma^2(r) = \sigma^2(r_0) + 2\int_{r_0}^{r} D_{ma}(r')dr'$$

where $D_{ma}(r)$, the field-line longitudinal diffusivity, is numerically integrated. Note that

$$D_{ma}(r,\theta) = \frac{D_{\phi\phi}(r,\theta)}{r^2}$$

for σ_ϕ and

$$D_{ma}(r) = \frac{D_{\theta\theta}(r)}{r^2}$$

for σ_θ. Both the theoretical solution and the Gaussian fit show a similar behaviour for the σ_ϕ and σ_θ values, where the σ increases quickly in the beginning before the rate of increase slows down until the σ values almost reach a plateau. The most significant difference between the Gaussian fit and the theoretical solution is that the Gaussian fit shows a larger increase for σ_ϕ, causing the values obtained from the fit to deviate from the theoretical solution. The σ_θ values, however, remain close to the theoretical solution. In addition to the deviation of the σ_ϕ values, the Gaussian fit also shows a larger increase in the σ_ϕ values than the σ_θ values, while the theoretical solution shows the opposite. The fittings seem to match the theoretical solution reasonably well for σ_θ, while failing to match the theoretical solution with regard to σ_ϕ. This is once again due to the method used for sampling the data.

The bottom panel in figure 4.7 shows the $\overline{\rho}_\phi$ along with the $\overline{\rho}_\theta$ values calculated by the Gaussian fit at intervals of 0.1 AU up to 1.2 AU. These values are compared to the ϕ and θ values of the Parker spiral. Both the $\overline{\rho}_\phi$ and the $\overline{\rho}_\theta$ values are nearly identical to the Parker spiral values. The $\overline{\rho}_\theta$ values belonging to the Gaussian fit and Parker spiral θ values remain near the starting θ value of $\frac{\pi}{2}$, although the $\overline{\rho}_\theta$ values are a bit below the Parker spiral θ values and do not remain at a constant value. Despite the fact that the $\overline{\rho}_\theta$ values fluctuate, these fluctuations are small enough to assume that there is no change in θ, similar to the Parker spiral. Similarly, the $\overline{\rho}_\phi$ values decrease at a constant rate while remaining near the Parker spiral ϕ values, though the $\overline{\rho}_\phi$ values show a slower decline than those of the Parker spiral ϕ values. This difference in slope could imply that the most likely path obtained through the simulation is underwound, since most of the $\overline{\rho}_\phi$ values possess a value either equal to or greater than the Parker spiral ϕ values. Both the top and bottom panels of figure 4.7 possess small error margins for the dependent values which increase with the radial distance, while the error in radial distance remains constant. The error margins for the respective dependent values are obtained from the Gaussian fits and are so small due to the amount of FISC-lines used. The error margins would grow larger if less lines were analysed and would shrink further if more lines were analysed. Conversely, the error margin for the radial distance is obtained by dividing by two the interval size, in this case 0.1 AU, between the observed points. As a result, the error margin will remain constant.

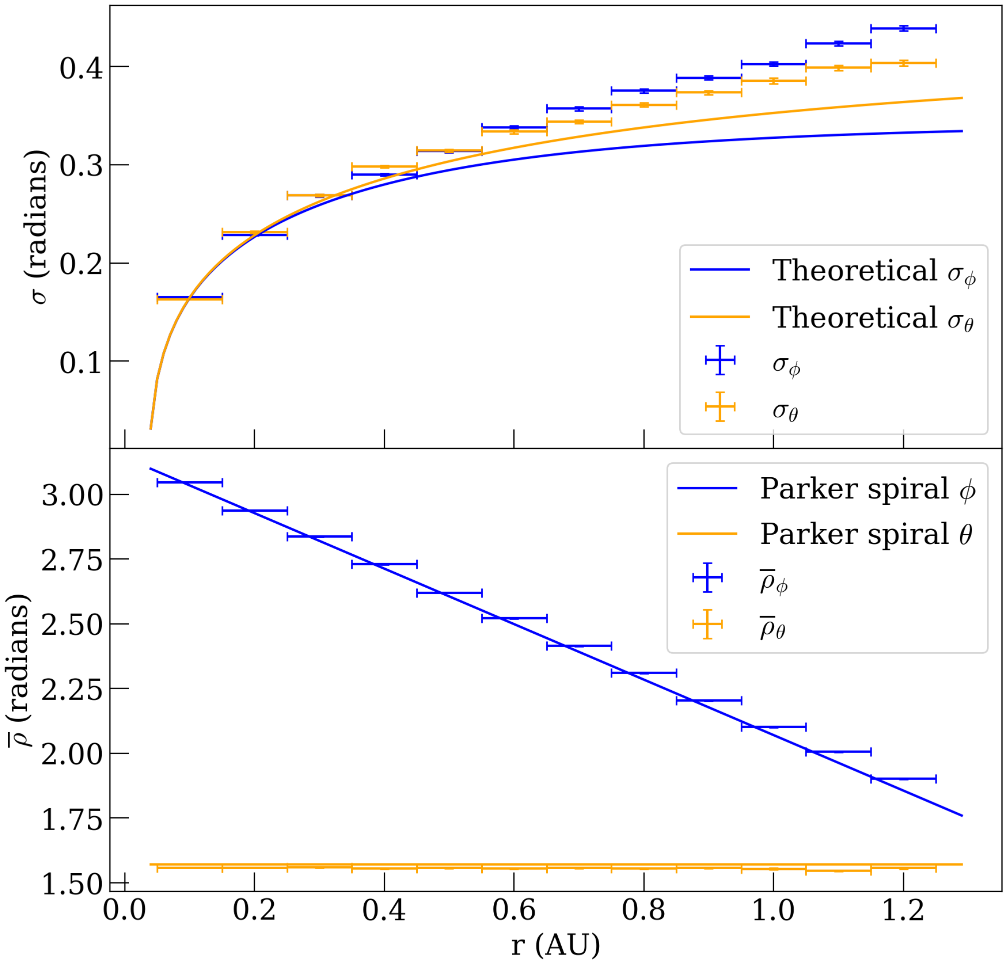

Figure 4.7: *Top*: σ_ϕ (blue crosses) and σ_θ (orange crosses) determined using a Gaussian fit compared to the theoretical solution for σ_ϕ (solid blue line) and σ_θ (solid orange line) as a function of radial distance from the Sun. *Bottom*: $\overline{\rho}_\phi$ values (blue crosses) and $\overline{\rho}_\theta$ values (orange crosses) compared to the Parker spiral ϕ (solid blue line) and θ (solid orange line) values at interval distances of 0.1AU from the Sun.

Similar to figure 4.5, the positions of the FISC-lines are determined for figure 4.8. However, instead of calculating the number of lines within each interval, the total normalized probability distribution found in every interval is determined by also taking the weight of each FISC-line into account. When comparing figures 4.5 and 4.8 with each other it is quite obvious that the two figures possess the same shape, although the corresponding intensity values differ. Within figure 4.8 the intensity decreases a lot faster than that of 4.5, which is expected. In addition, the $\overline{\rho}$ values determined using the Gaussian fits are illustrated in figure 4.8 at every 0.1 AU interval to better compare the $\overline{\rho}$ values, and therefore the most likely path which a magnetic field-line would follow, to the Parker spiral. The $\overline{\rho}$ are displayed using crosses; these crosses represent the margin of error for the radial distance and the azimuthal angle. It should also be mentioned that white dots were added to the crosses to better show the centre of each cross. This comparison shows that the $\overline{\rho}$ values remain near the Parker spiral, with most being on top of the spiral. The average difference between the most likely path and the Parker spiral is 1.1%. By obtaining an estimated magnetic field-line path, the most likely behaviour of said magnetic field-line under specific conditions, such as more or less diffusion (discussed later in this chapter) or a change in SW speed, can be determined. It should also be mentioned that while the estimated path is the most likely path which a magnetic filed-line would follow, it is still possible that the field-line can take an entirely different path than the estimated one, though with a lower probability.

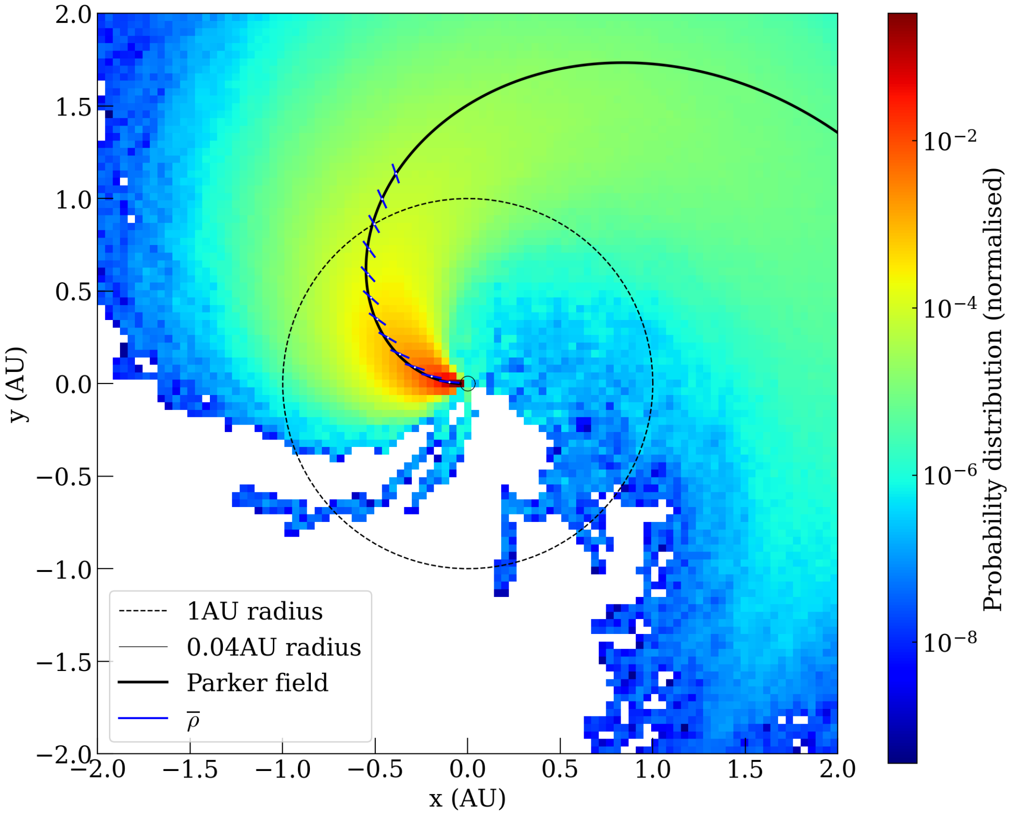

Figure 4.8: Density map of the 2D profile showing the normalized probability distribution calculated along the FISC-lines, the $\overline{\rho}$ values (blue crosses) compared to the Parker spiral (thick solid black line), the 1 AU radius (dashed black line) and the starting radius (thin solid black line).

Figure 4.9 shows a Mollweide projection of a theoretical sphere with a radius of 1 AU around the Sun. Similar to figure 4.8, the normalized probability distribution for each interval on the surface of the sphere is determined and displayed using a density map, where blue once again indicates a lower intensity and red indicates a higher intensity. It is important to note that the Mollweide projection uses a geodetic coordinate system, meaning that the equatorial plane is located at $\theta = 0$ instead of at $\theta = \frac{\pi}{2}$ as with most of the previous figures. Along with the density map, the location of the maximum probability value on the sphere surface in addition to the locations of where the Parker spiral and the most likely path pass through the sphere are shown as well. Finally the standard deviation on the $\overline{\rho}$ value at 1 AU is shown as a blue area; within this area about 68% of the FISC-lines can be found. It is apparent from figure 4.9 that the Parker spiral, the most likely path, and the maximum probability are all located incredibly close to one another, with the most likely path being closest to the Parker spiral. Furthermore, these values are all located within one standard deviation. Due to the virtually similar locations of the Parker spiral and the most likely path, the close proximity of the maximum probability value and the fact that all three are located within one standard deviation, it can be argued that if a magnetic field-line is not located along the most likely path, then it will still in all likelihood be found within one standard deviation from the Parker spiral. Similar to figure 4.8, figure 4.9 shows that the probability distribution is greater nearer to the Parker spiral and decreases with the increase of distance from the spiral, although figure 4.9 shows that this is true for areas both above and below the Parker spiral and not just to the left and right of the spiral.

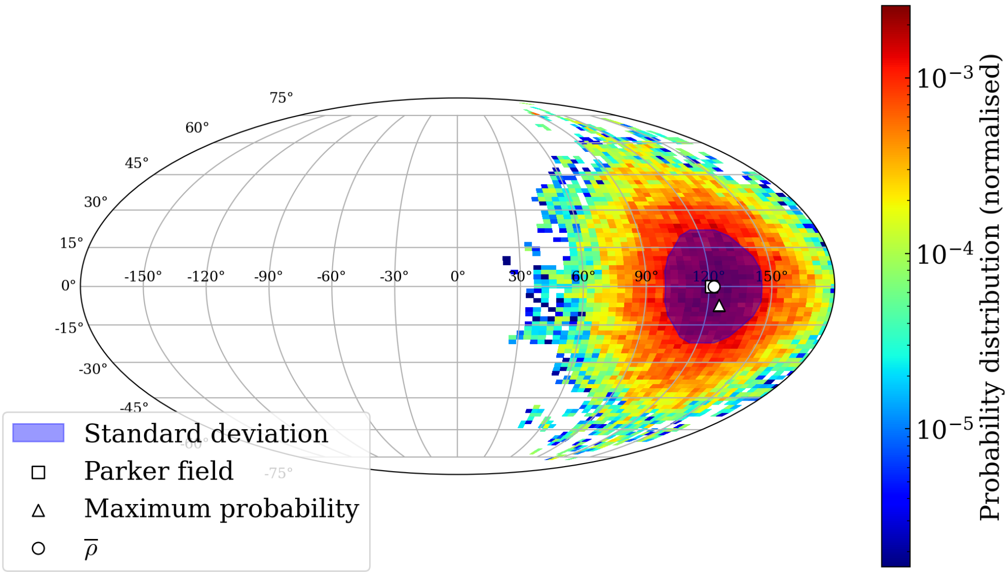

Figure 4.9: Mollweide projection depicting the probability distribution at a radial distance of 1 AU around the Sun as an intensity map. The position of the $\overline{\rho}$ value (white circle), along with σ (blue area), is compared with the position of the Parker spiral (white square), as well as the maximum probability value (white triangle).

Zooming in on the area around the Parker spiral yields figure 4.10, although in figure 4.10 the equatorial plane is once more located at $\theta = \frac{\pi}{2}$ and not at $\theta = 0$. Figure 4.10 reiterates the fact that σ_ϕ is larger than σ_θ at a radius of 1 AU, as was concluded from figures 4.6a and 4.6b. Moreover a better perspective of how close the most likely path and Parker spiral are to one another is shown; this new perspective shows that the most likely path is even closer to the Parker spiral than what figure 4.9 leads to believe. Figure 4.10 further shows that the FISC-lines, and as a consequence the probability distribution, are not perfectly symmetrical around the Parker spiral. Rather, the FISC-lines lean more towards the left side of the graph, leading to the graph being more rounded along the left-hand side, while the right-hand side is more vertically aligned. Despite the fact that all of the FISC-lines originate from the same point of origin and that most FISC-lines remain near the Parker spiral, there are still FISC-lines which deviate to such a degree that they end up around or close to the polar regions of the 1 AU sphere, as seen in figure 4.4. For this reason, it is theoretically possible, although highly unlikely, for a magnetic field-line starting at the equatorial plane to diffuse to such an extent as to reach the polar angles. Due to the most likely path being so similar to the Parker spiral, it can be reasoned that the reference scenario is a suitable simulation of the HMF if the purpose of the simulation is to determine the fundamental change in behavior of the HMF caused by turbulence.

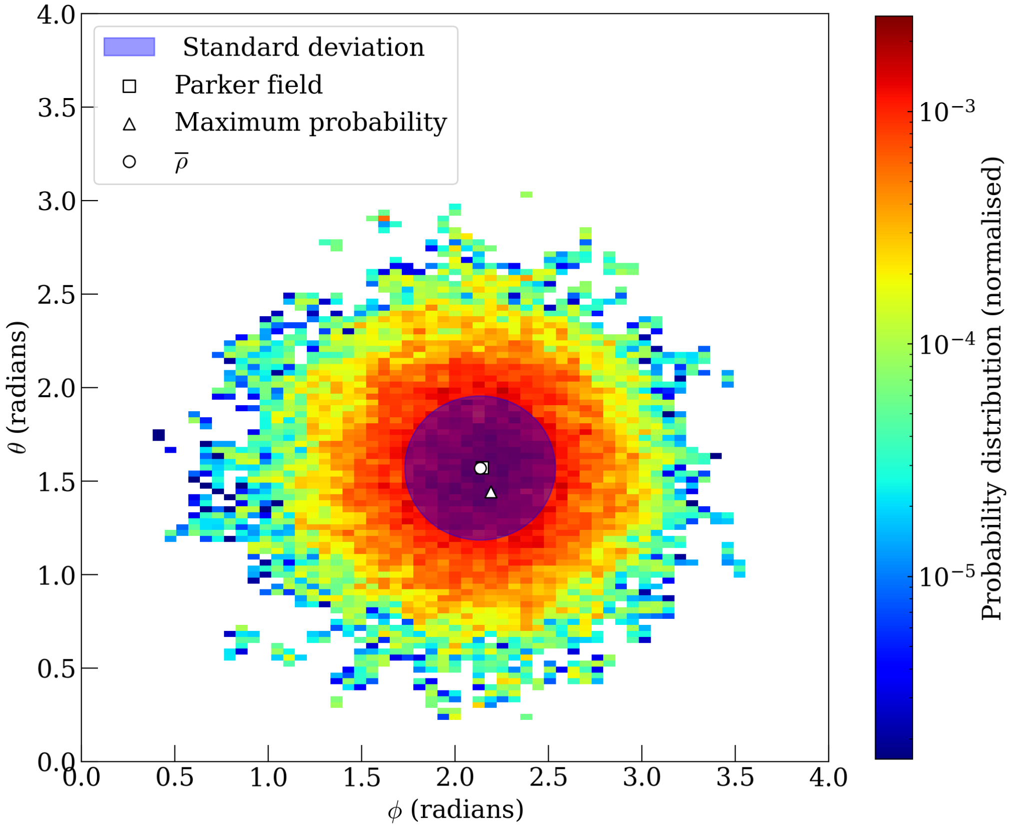

Figure 4.10: The zoomed-in view of the intensity map around the Parker spiral (white square), the $\overline{\rho}$ value (white circle), the maximum probability (white triangle) and σ (blue area) on the Mollweide projection is now shown in Cartesian coordinates.

4.2 Increased and Reduced Diffusion Values

With a reference scenario established, the effect of greater and lesser diffusion on the HMF structure can be investigated. To determine the dependence of the HMF on the diffusion coefficient, the simulation is run four more times. For these runs the point of origin for the FISC-lines is once again at a radial distance of 0.04 AU, a polar angle of $\theta = \frac{\pi}{2}$ and an azimuthal angle of $\phi = \pi$. The SW speed, solar rotation rate and the initial magnetic field intensity values are all identical to the reference scenario as well. The only difference between the reference scenarios and the following simulations is the change in diffusion coefficients. For simplification, the different simulations will be referred to as simulations 1 to 4. For simulation 1 the diffusion coefficient utilized in the reference scenario is assumed to be ten times smaller; for simulation 2 the diffusion coefficient is two times smaller; simulation 3 implements a diffusion coefficient two times greater than that of the reference scenario, and finally simulation 4 uses a four times greater diffusion coefficient.

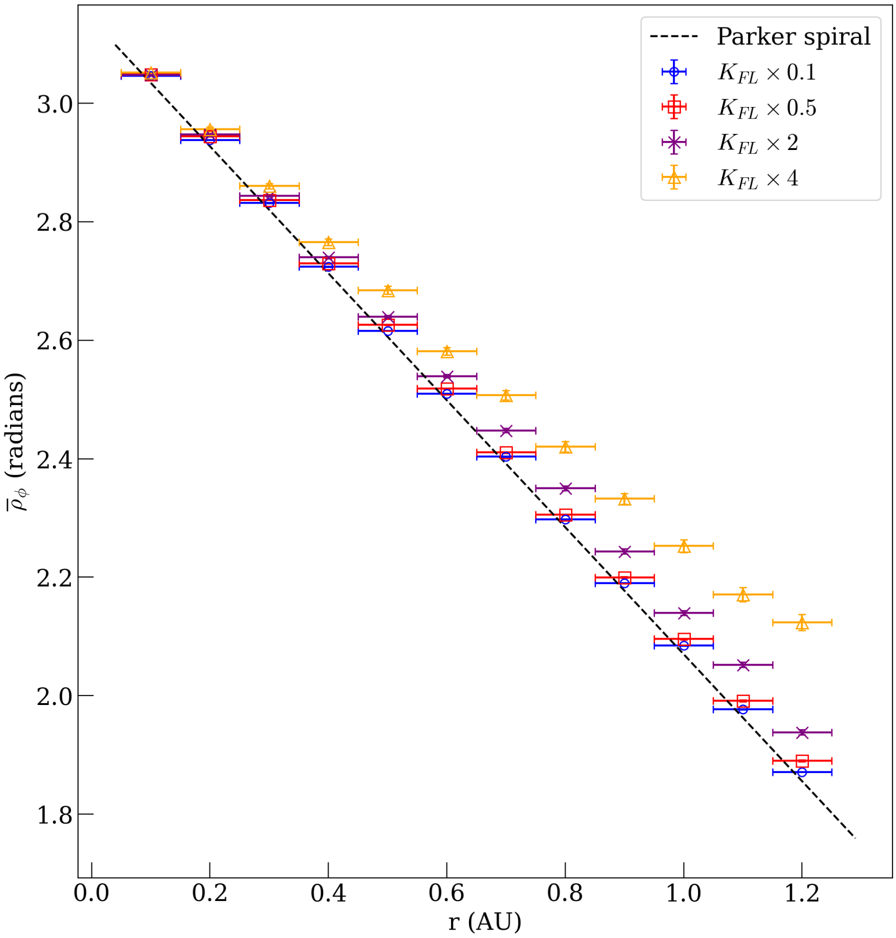

Figure 4.11: $\overline{\rho}_\phi$ values as a function of radial distance for $K_{FL} \times 4$ (orange with triangle), $K_{FL} \times 2$ (purple with cross), $K_{FL} \times 0.5$ (red with square) and $K_{FL} \times 0.1$ (blue circle). Included as well are the ϕ values of the ideal Parker spiral (dashed black line) as a function of radial distance.

As with figure 4.7, the $\overline{\rho}_\phi$ values obtained from the four simulations are displayed at every 0.1 AU interval and compared to the ϕ values of the Parker spiral in figure 4.11. For simulations 1 and 2 the $\overline{\rho}_\phi$ values remain near the Parker spiral ϕ values, similar to that of figure 4.7. The $\overline{\rho}_\phi$ values for these simulations in figure 4.11 are even closer to the Parker spiral than those of the reference scenario, with simulation 1 being the closest, and deviating less with the increase of radial distance. The only inconsistency between the $\overline{\rho}_\phi$ values of the two simulations is that the $\overline{\rho}_\phi$ values of simulation 1 remain near the Parker spiral ϕ values, while the simulation 2 $\overline{\rho}_\phi$ values deviate slightly more than that of simulation 1. Simulation 3 shows the same straight line behaviour in the $\overline{\rho}_\phi$ values as simulations 1 and 2, although these values deviate to a greater degree than that of simulations 1 and 2. Finally, simulation 4 shows the largest deviation in the $\overline{\rho}_\phi$ values out of the four simulations. Similar to the previous simulations, simulation 4 starts with a linear decrease in the $\overline{\rho}_\phi$ values, but at around 1 AU the $\overline{\rho}_\phi$ values begin to decrease at a slower rate. Another difference between the respective $\overline{\rho}_\phi$ values of the four simulations is the margin of error. For a small diffusion coefficient the margin of error for each point remains small for greater distances, while large diffusion coefficients cause the error margins to grow larger much more quickly. At a cursory glance it would appear that all of the simulations will produce an underwound magnetic field-line, assuming the magnetic field-line perfectly follows the most likely path, since each of the $\overline{\rho}_\phi$ values are located above that of the Parker spiral, with the magnetic field-line produced by simulation 4 being the most overwound.

Figure 4.12 shows the normalized probability distribution for simulations 1 to 4 as density maps, where the colour red indicates a higher intensity and the colour blue a lower intensity. If there is no intensity to be found in an area, the area remains colourless once more. The Parker spiral is depicted on each of the graphs as well, along with the 1 AU and point of origin radii. Finally the most likely path for each simulation is indicated on the respective graphs as blue crosses. The crosses used to show the most likely path also depict the margin of error for both the radial distance and the azimuthal angle ϕ. The most noticeable difference between each graph in figure 4.12 is the change in area of where the FISC-lines, and hence the HMF intensities, can be found. For simulations 1 and 2, which have lower diffusion coefficient values, the FISC-lines remain closer to the Parker spiral for greater distances. On the other hand, simulations 3 and 4 produce a much larger area as a result of the larger diffusion coefficient values. For large enough diffusion coefficient values the FISC-lines, which usually show the same tendency as the Parker spiral, will be dispersed throughout the entire area around the Sun as seen in the top graph of figure 4.12.

Upon closer examination of figure 4.12, it becomes evident that it is not just the FISC-line trajectories and the area in which the HMF can be found which are changed, but the most likely path as well. The most likely path yielded by simulation 1 possesses close to the same curvature as the Parker spiral with an average difference of 0.5%, although it shows a hint of being overwound. The overwinding is most likely caused by the Gaussian fits, since the most likely path should approach the path of the Parker spiral as was shown in section 3.2.1. Simulation 2 produces a most likely path almost identical to the Parker spiral, with an average difference of 0.9%. In contrast, simulations 3 and 4 show most likely paths which are obviously underwound, with simulation 4 showing the greatest change in the most likely path, with an average difference of 2.2% and 5.3% respectively. Whereas simulations 1, 2 and 3 yield most likely paths which seem to show a similar curvature to that of the Parker spiral, simulation 4 only starts out with a similar curvature; after about 0.9 AU the most likely path seems to almost straighten out. An additional observation which can be made from the various most likely paths is that the margin of error for the azimuthal angle ϕ grows larger at an increased rate as the diffusion coefficient increases. Consequently, the most likely path, and hence the HMF, will be similar to the Parker spiral for lesser diffusion, while overwound for greater diffusion. This corresponds with the winding angle analysis done by Van Der Merwe and Engelbrecht (2025).

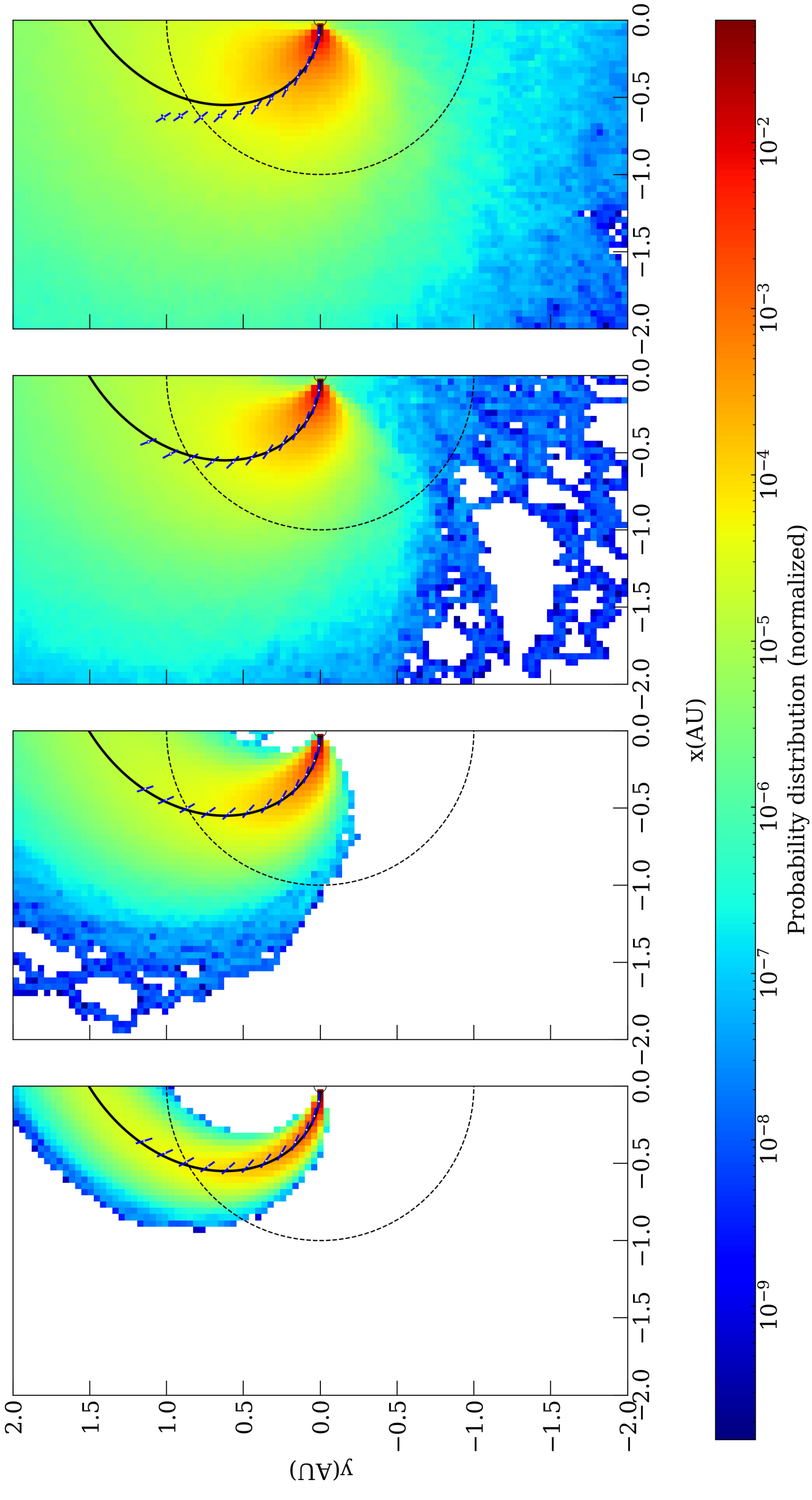

Figure 4.12: Probability distribution shown as intensity maps for $K_{FL} \times 4$ (top), $K_{FL} \times 2$ (second), $K_{FL} \times 0.5$ (third) and $K_{FL} \times 0.1$ (bottom). All of the graphs show the starting radius (solid black line), the 1 AU radius (black dashed line), the ideal Parker spiral (thick black line) and the most likely path (blue crosses) for each simulation.

4.3 Summary

This chapter applied the stochastic field-line random walk model which was introduced in chapter 3 by comparing the model to analytical approximations and published numerical models. It was found that the density of FISC-lines is highest around the Parker spiral and that it decreases as the distance from the Parker spiral increases. It was seen that the distribution of the probability distribution at various radii, ϕ and θ values yielded similar results to the Gaussian fits. The comparison of the σ_ϕ and σ_θ values to the theoretical solution obtained from Bian et al. (2024) showed similar results at small radial distance, but started to differ at larger distances, especially with regards to σ_ϕ. For the reference scenario, the calculated $\overline{\rho}_\phi$ and $\overline{\rho}_\theta$ values showed similar results to the Parker spiral ϕ and θ values. It was found that a larger diffusion coefficient leads to the most likely path being underwound, which corresponds with observational data. For a smaller diffusion coefficient the most likely path is similar to the Parker spiral, with the most likely path matching the Parker spiral for a diffusion coefficient equal to zero.

Chapter 5

Summary and Conclusions

This study summarised the fundamental physics encapsulating the meandering of magnetic field-lines due to turbulence within the SW and introduced an SDE-based model with which to model the turbulent HMF.

Chapter 2 introduced the dynamic nature of the Sun, which is caused by the increase and decrease of solar activity, and how this nature affects various structures within the heliosphere, including the SW and the HMF. The SW is the continuous outward expansion of solar matter produced by the high coronal temperatures and consists mainly of protons, electrons, and alpha particles. During solar minimum the SW possesses relatively slow speeds within the ecliptic and fast speeds over the polar coronal holes. During solar maximum the heliographic latitudinal dependency disappears causing the slow and fast SW to be observable over all latitudes. Furthermore, the SW carries out the frozen-in magnetic field-lines into the rest of the heliosphere, thereby forming the HMF. During solar minimum the HMF possesses an almost dipole structure, while during solar maximum the structure becomes much more complex. The chapter also introduced the HMF model as derived by Parker (1958), which describes the form of the HMF as Archimedian spirals. The HMF derivations of Gleeson and Webb (1980) and Steenkamp (1995), which yield similar results, were also discussed.

The chapter concluded with the introduction of the basic concepts of turbulence theory relevant to this study. These concepts include the correlation tensor, which describes the evolution of the magnetic field within homogeneous turbulence, and the cascade of energy, known as the turbulence power spectrum. The power spectrum consists of several subranges. The subranges discussed were the energy containing scales, which provide most of the energy for the turbulent cascade and have a k^{-1} wavenumber dependence, the inertial range, which has a spectral index of $-\frac{5}{3}$, and the dissipation range, which has a spectral index of -3. The related lengthscales mentioned were the outerscale, the ultrascale and the correlation length. The outerscale describes the energy cascade within the energy containing scales; the ultrascale is associated with curvature of the correlation function and is often used in the 2D turbulence model, and the correlation is associated with the area under the correlation tensor. The 2D turbulence model is often used to simulate the transverse fluctuations within a magnetic field. While not utilised within this study, the slab turbulence model, which simulates Alfvén type fluctuations, was discussed as well. The radial dependence of the turbulence quantities were also discussed. Finally, a brief introduction on the FLRW, a process which directly influences the transport of particles within the heliosphere, was given.

In **chapter 3** SDEs were introduced as a method with which to solve Fokker-Planck type equations. It was shown that for each n-dimensional Fokker-Plank equation, an equivalent set of $n-1$ SDEs exists through the use of Brownian motion. Following the discussion on SDEs, the convection-diffusion equation for field-line diffusion was first derived from the FTE for particles and then transformed into the relevant set of SDEs using both the time-forwards and the time-backwards formulation, although only the time-forwards formulation was implemented within the construction of the SDE-based FLRW model.

In **chapter 4** the SDE-based FLRW model was applied to the Parker HMF model, assuming solar minimum conditions. It was found that the FISC-lines, the lines which track the magnetic field-line probability distribution, are most dense around the Parker spiral, but spread out as the radial distance increases. This is expected from a diffusion process. The distribution of the probability distribution calculated by the FISC-lines yielded similar results to Gaussian fits for several radii, ϕ-, and θ-values, although the σ_ϕ and σ_θ values calculated from the Gaussian fits only correspond with the theoretical solution, obtained from Bian et al. (2024), at small radial values. From the reference scenario it was found that the calculated $\bar{\rho}_\phi$ and $\bar{\rho}_\theta$ values are similar to the turbulence-free Parker HMF model, although the $\bar{\rho}_\phi$ values seemed to imply an underwound most likely path. Simulations 1 to 4 determined that for lesser diffusion the most likely path would be similar to the ideal Parker spiral, while for greater diffusion the most likely path would become increasingly underwound. This is a consequence of the non-cartesian HMF geometry and radial dependent (non-homogeneous) turbulence assumed in this study.

Further research related to this study includes:

- Constructing a similar model by using the time-backwards formulation instead of the time-forwards formulation and comparing the results to that of the time-forwards formulation model.

- Utilizing different or more realistic turbulence transport models to calculate the input values for the FLRW model to simulate the heliospheric magnetic field under the effects of a more realistic turbulent solar wind with which to observe the meandering of field-lines.

- Studying the connection between FLRW diffusion coefficient of field-lines and FLRW coefficient for particles, as well as the effect of the remaining free parameters which determine how closely the particles follow meandering field-lines.

Bibliography

Alanko-Huotari, K., Usoskin, I., Mursula, K., and Kovaltsov, G. (2007). Cyclic variations of the heliospheric tilt angle and cosmic ray modulation. *Advances in Space Research*, 40(7):1064–1069.

Balogh, A., Lanzerotti, L. J., and Suess, S. T. (2008). *The Heliosphere through the Solar Activity Cycle*. Springer Berlin Heidelberg, Berlin.

Batchelor, G. K. (1953). *The theory of homogeneous turbulence*. Cambridge monographs on mechanics and applied mathematics. University Press, Cambridge.

Bian, N. H., Strauss, R. D., Li, G., and Engelbrecht, N. E. (2024). Heliospheric Diffusion of Stochastic Parker Spirals in Radially Evolving Solar Wind Turbulence. *The Astrophysical Journal*, 962(2):186.

Biermann, L. (1957). Solar corpuscular radiation and the interplanetary gas. *The Observatory*, 77:109–110.

Bobik, P., Boschini, M. J., Della Torre, S., Gervasi, M., Grandi, D., La Vacca, G., Pensotti, S., et al. (2016). On the forward-backward-in-time approach for Monte Carlo solution of Parker's transport equation: One-dimensional case. *Journal of Geophysical Research: Space Physics*, 121(5):3920–3930.

Breech, B., Matthaeus, W. H., Minnie, J., Bieber, J. W., Oughton, S., Smith, C. W., and Isenberg, P. A. (2008). Turbulence transport throughout the heliosphere. *Journal of Geophysical Research: Space Physics*, 113(A8):2007JA012711.

Burger, R. and McKee, S. (2023). Evaluation and analysis of Voyager 1 48-s resolution magnetic field data. *Advances in Space Research*, 71(11):4916–4922.

Burlaga, L. F. (1991). Intermittent turbulence in the solar wind. *Journal of Geophysical Research: Space Physics*, 96(A4):5847–5851.

Chhiber, R., Matthaeus, W. H., Cohen, C. M. S., Ruffolo, D., Sonsrettee, W., Tooprakai, P., Seripienlert, A., et al. (2021). Magnetic field line random walk and solar energetic particle path lengths: Stochastic theory and PSP/IS⊙IS observations. *Astronomy & Astrophysics*, 650:A26.

Chhiber, R., Pecora, F., Usmanov, A. V., Matthaeus, W. H., Goldstein, M. L., Roy, S., Wang, J., et al. (2024). The Alfvén transition zone observed by the Parker Solar

Probe in young solar wind – global properties and model comparisons. *Monthly Notices of the Royal Astronomical Society: Letters*, 533(1):L70–L75.

Chhiber, R., Usmanov, A. V., DeForest, C. E., Matthaeus, W. H., Parashar, T. N., and Goldstein, M. L. (2018a). Weakened Magnetization and Onset of Large-scale Turbulence in the Young Solar Wind—Comparisons of Remote Sensing Observations with Simulation. *The Astrophysical Journal Letters*, 856(2):L39.

Chhiber, R., Usmanov, A. V., Matthaeus, W. H., and Goldstein, M. L. (2018b). Contextual Predictions for Parker Solar Probe I: Critical Surfaces and Regions. *The Astrophysical Journal Supplement Series*, 241(1):11.

Choudhuri, A. R. (1998). *The Physics of Fluids and Plasmas: An Introduction for Astrophysicists*. Cambridge University Press, Cambridge, 1st edition.

Chuychai, P., Ruffolo, D., Matthaeus, W. H., and Meechai, J. (2007). Trapping and Diffusive Escape of Field Lines in Two-Component Magnetic Turbulence. *The Astrophysical Journal*, 659(2):1761–1776.

Coleman, Jr., P. J. (1968). Turbulence, Viscosity, and Dissipation in the Solar-Wind Plasma. *The Astrophysical Journal*, 153:371.

Cranmer, S. R. (2009). Coronal Holes. *Living Reviews in Solar Physics*, 6.

Cranmer, S. R., Gibson, S. E., and Riley, P. (2017). Origins of the Ambient Solar Wind: Implications for Space Weather. *Space Science Reviews*, 212(3-4):1345–1384.

Cuesta, M. E., Chhiber, R., Roy, S., Goodwill, J., Pecora, F., Jarosik, J., Matthaeus, W. H., et al. (2022). Isotropization and Evolution of Energy-containing Eddies in Solar Wind Turbulence: Parker Solar Probe, Helios 1, ACE, WIND, and Voyager 1. *The Astrophysical Journal Letters*, 932(1):L11.

Davidson, 1957, P. A. (2004). *Turbulence : an introduction for scientists and engineers*. Oxford University Press, Oxford.

Einstein, A. (1905). Über die von der molekularkinetischen Theorie der Wärme geforderte Bewegung von in ruhenden Flüssigkeiten suspendierten Teilchen. *Annalen der Physik*, 322(8):549–560.

Engelbrecht, N. (2013). *On the development and applications of a three-dimensional ab initio cosmic-ray modulation model*. PhD thesis.

Engelbrecht, N. E. and Burger, R. A. (2015). Sensitivity of cosmic-ray proton spectra to the low-wavenumber behavior of the 2D turbulence power spectrum. *The Astrophysical Journal*, 814(2):152.

Erdős, G. and Balogh, A. (2005). In situ observations of magnetic field fluctuations. *Advances in Space Research*, 35(4):625–635.

Fisk, L. A. (1996). Motion of the footpoints of heliospheric magnetic field lines at the Sun: Implications for recurrent energetic particle events at high heliographic latitudes. *Journal of Geophysical Research: Space Physics*, 101(A7):15547–15553.

Frisch, U. and Kolmogorov, A. N. (1995). *Turbulence : the legacy of A.N. Kolmogorov*. Cambridge University Press, Cambridge.

Gardiner, C. W. (1985). *Handbook of stochastic methods: for physics, chemistry, and the natural sciences*. Springer-Verlag, Berlin, 2nd edition.

Gleeson, L. J. and Webb, G. M. (1980). The Propagation of Cosmic-Rays in the Interplanetary Region (The Theory). *Fundamentals of Cosmic Physics*, 6:187–312.

Goldstein, M. L. and Roberts, D. A. (1999). Magnetohydrodynamic turbulence in the solar wind. *Physics of Plasmas*, 6(11):4154–4160.

Goldstein, M. L., Roberts, D. A., and Matthaeus, W. H. (1995). Magnetohydrodynamic Turbulence in the Solar Wind. *Annual Review of Astronomy and Astrophysics*, 33(1):283–325.

Hathaway, D. H. and Suess, S. T. (2008). Solar cycle 23. In *The Heliosphere through the Solar Activity Cycle*, pages 21–39. Springer Berlin Heidelberg, Berlin.

Hedgecock, P. C. (1975). Measurements of the interplanetary magnetic field in relation to the modulation of cosmic rays. *Solar Physics*, 42(2):497–527.

Hoeksema, J. T. (1992). Large-scale structure of the heliospheric magnetic field - 1976-1991. pages 191–196.

Jokipii, J. R. (1966). Cosmic-Ray Propagation. I. Charged Particles in a Random Magnetic Field. *The Astrophysical Journal*, 146:480.

Jokipii, J. R. (1973). The Rate of Separation of Magnetic Lines of Force in a Random Magnetic Field. *The Astrophysical Journal*, 183:1029.

Jokipii, J. R. and Kóta, J. (1989). The polar heliospheric magnetic field. *Geophysical Research Letters*, 16(1):1–4.

Jokipii, J. R. and Parker, E. N. (1969). Stochastic Aspects of Magnetic Lines of Force with Application to Cosmic-Ray Propagation. *The Astrophysical Journal*, 155:777.

Jokipii, J. R. and Thomas, B. (1981). Effects of drift on the transport of cosmic rays. IV - Modulation by a wavy interplanetary current sheet. *The Astrophysical Journal*, 243:1115.

Kloeden, P. E. and Platen, E. (1999). *Numerical solution of stochastic differential equations*. Applications of mathematics; 23. Springer, Berlin, corr. 3rd print edition.

Kloeden, P. E., Platen, E., and Schurz, H. (1994). *Numerical solution of SDE through computer experiments*. Universitext. Springer-Verlag, Berlin.

Kolmogorov, A. (1941). The Local Structure of Turbulence in Incompressible Viscous Fluid for Very Large Reynolds' Numbers. *Akademiia Nauk SSSR Doklady*, 30:301–305.

Kopp, A., Büsching, I., Strauss, R., and Potgieter, M. (2012). A stochastic differential equation code for multidimensional Fokker–Planck type problems. *Computer Physics Communications*, 183(3):530–542.

Leamon, R. J., Smith, C. W., Ness, N. F., Matthaeus, W. H., and Wong, H. K. (1998). Observational constraints on the dynamics of the interplanetary magnetic field dissipation range. *Journal of Geophysical Research: Space Physics*, 103(A3):4775–4787.

Lemons, D. S. (2002). *An introduction to stochastic processes in physics*. Johns Hopkins University Press, Baltimore.

Marsch, E. (1991). MHD Turbulence in the Solar Wind. In Huber, M. C. E., Lanzerotti, L. J., Stöffler, D., Schwenn, R., and Marsch, E., editors, *Physics of the Inner Heliosphere II*, volume 21, pages 159–241. Springer Berlin Heidelberg, Berlin, Heidelberg.

Maruyama, G. (1955). Continuous Markov processes and stochastic equations. *Rendiconti del Circolo Matematico di Palermo*, 4(1):48–90.

Matthaeus, W. H., Bieber, J. W., Ruffolo, D., Chuychai, P., and Minnie, J. (2007). Spectral Properties and Length Scales of Two-dimensional Magnetic Field Models. *The Astrophysical Journal*, 667(2):956–962.

Matthaeus, W. H., Goldstein, M. L., and Roberts, D. A. (1990). Evidence for the presence of quasi-two-dimensional nearly incompressible fluctuations in the solar wind. *Journal of Geophysical Research*, 95:20673–20683. ADS Bibcode: 1990JGR....9520673M.

Matthaeus, W. H., Gray, P. C., Pontius, Jr., D. H., and Bieber, J. W. (1995). Spatial Structure and Field-Line Diffusion in Transverse Magnetic Turbulence. *Physical Review Letters*, 75(11):2136–2139.

Matthaeus, W. H., Qin, G., Bieber, J. W., and Zank, G. P. (2003). Nonlinear Collisionless Perpendicular Diffusion of Charged Particles. *The Astrophysical Journal*, 590(1):L53–L56.

McComas, D. J., Bame, S. J., Barraclough, B. L., Feldman, W. C., Funsten, H. O., Gosling, J. T., Riley, P., et al. (1998). Ulysses' return to the slow solar wind. *Geophysical Research Letters*, 25(1):1–4.

McComas, D. J., Elliott, H. A., Schwadron, N. A., Gosling, J. T., Skoug, R. M., and Goldstein, B. E. (2003). The three-dimensional solar wind around solar maximum. *Geophysical Research Letters*, 30(10).

Montgomery, D. (1983). Theory of hydromagnetic turbulence. *JPL Solar Wind Five*.

Mumford, S. J., Freij, N., Stansby, D., Christe, S., Shih, A. Y., Ireland, J., Mayer, F., et al. (2025). sunpy: A Core Package for Solar Physics.

Øksendal, B. K. (2000). *Stochastic differential equations : an introduction with applications*. Springer-Verlag, Verlag, 5th edition.

Osman, K. T. and Horbury, T. S. (2007). Multispacecraft Measurement of Anisotropic Correlation Functions in Solar Wind Turbulence. *The Astrophysical Journal*, 654(1):L103–L106.

Owens, M. J. and Forsyth, R. J. (2013). The Heliospheric Magnetic Field. *Living Reviews in Solar Physics*, 10.

Parker, E. N. (1958). Dynamics of the Interplanetary Gas and Magnetic Fields. *The Astrophysical Journal*, 128:664.

Petrosyan, A., Balogh, A., Goldstein, M. L., Léorat, J., Marsch, E., Petrovay, K., Roberts, B., et al. (2010). Turbulence in the Solar Atmosphere and Solar Wind. *Space Science Reviews*, 156(1-4):135–238.

Phillips, J. L., Bame, S. J., Barnes, A., Barraclough, B. L., Feldman, W. C., Goldstein, B. E., Gosling, J. T., et al. (1995). Ulysses solar wind plasma observations from pole to pole. *Geophysical Research Letters*, 22(23):3301–3304.

Ruffolo, D., Matthaeus, W. H., and Chuychai, P. (2004). Separation of Magnetic Field Lines in Two-Component Turbulence. *The Astrophysical Journal*, 614(1):420–434.

Shalchi, A. (2019). Field line random walk, field line separation, and particle transport in turbulence with weak transverse complexity. *Advances in Space Research*, 64(12):2426–2438.

Shalchi, A. and Kourakis, I. (2007). A new theory for perpendicular transport of cosmic rays. *Astronomy & Astrophysics*, 470(2):405–409.

Shalchi, A. and Weinhorst, B. (2009). Random walk of magnetic field lines: Subdiffusive, diffusive, and superdiffusive regimes. *Advances in Space Research*, 43(9):1429–1435.

Skilling, J. (1971). Cosmic Rays in the Galaxy: Convection or Diffusion? *The Astrophysical Journal*, 170:265.

Smith, C. W. and Bieber, J. W. (1991). Solar cycle variation of the interplanetary magnetic field spiral. *The Astrophysical Journal*, 370:435.

Smith, C. W., Hamilton, K., Vasquez, B. J., and Leamon, R. J. (2006a). Dependence of the Dissipation Range Spectrum of Interplanetary Magnetic Fluctuationson the Rate of Energy Cascade. *The Astrophysical Journal*, 645(1):L85–L88.

Smith, C. W., Isenberg, P. A., Matthaeus, W. H., and Richardson, J. D. (2006b). Turbulent Heating of the Solar Wind by Newborn Interstellar Pickup Protons. *The Astrophysical Journal*, 638(1):508–517.

Smith, C. W., Matthaeus, W. H., Zank, G. P., Ness, N. F., Oughton, S., and Richardson, J. D. (2001). Heating of the low-latitude solar wind by dissipation of turbulent magnetic fluctuations. *Journal of Geophysical Research: Space Physics*, 106(A5):8253–8272.

Smith, E. J. (2008). The global heliospheric magnetic field. In *The Heliosphere through the Solar Activity Cycle*, pages 79–150. Springer Berlin Heidelberg, Berlin.

Steenkamp, R. (1995). *Shock acceleration as source of the anomalous component of cosmic rays in the heliosphere*. PhD thesis.

Stix, M. (2004). *The sun : an introduction*. Astronomy and astrophysics library, 0941-7834. Springer, Berlin, 2nd edition.

Strauss, R. D. T. and Effenberger, F. (2017). A Hitch-hiker's Guide to Stochastic Differential Equations: Solution Methods for Energetic Particle Transport in Space Physics and Astrophysics. *Space Science Reviews*, 212(1-2):151–192.

Tennekes, H. and Lumley, J. L. (1972). *A first course in turbulence*. The MIT Press, Cambridge.

van Kampen, N. G. (2007). *Stochastic processes in physics and chemistry*. North-Holland personal library. Elsevier, Amsterdam, 3rd edition.

Van Der Merwe, F. H. and Engelbrecht, N. E. (2025). Revisiting the Winding Angle of the Heliospheric Magnetic Field: Investigating the Influence of Turbulence. *Solar Physics*, 300(6):80.

Virtanen, P., Gommers, R., Oliphant, T. E., Haberland, M., Reddy, T., Cournapeau, D., Burovski, E., et al. (2020). SciPy 1.0: fundamental algorithms for scientific computing in Python. *Nature Methods*, 17(3):261–272.

Weber, E. J. and Davis, Jr., L. (1967). The Angular Momentum of the Solar Wind. *The Astrophysical Journal*, 148:217.

Weinhorst, B., Shalchi, A., and Fichtner, H. (2008). The Cosmic-Ray Diffusion Tensor in Nonaxisymmetric Turbulence. *The Astrophysical Journal*, 677(1):671–675.

Weygand, J. M., Matthaeus, W. H., Dasso, S., and Kivelson, M. G. (2011). Correlation and Taylor scale variability in the interplanetary magnetic field fluctuations as a function of solar wind speed. *Journal of Geophysical Research: Space Physics*, 116(A8).

Zank, G. P., Matthaeus, W. H., and Smith, C. W. (1996). Evolution of turbulent magnetic fluctuation power with heliospheric distance. *Journal of Geophysical Research: Space Physics*, 101(A8):17093–17107.

Acknowledgements

Above all, I would like to thank God and Jesus Christ, for blessing me with the mind and mental ability to not only understand physics and mathematics, but to research them as well.

I would also like to thank the following persons and institutions for their support:

- My supervisor, Prof. R.D.T. Strauss, for his excellent guidance, stimulating discussions, and thorough explanations, as well as his immense patience.
- Dr J Light, my co-supervisor, for double checking my math and for always being willing to lend a helping hand.
- Prof. N.E. Engelbrecht, for the discussions and help with all things turbulence.
- The National Astrophysics and Space Science Program (NASSP), the Centre for Space Research (CSR), and the North-West University (NWU) for financial and infrastructure support throughout my studies.
- My friends and colleagues, for the interesting discussions and for the memorable laughs.
- Mr L. Fransman, Ms E. van Rooyen, Ms L. van Wyk, and Ms E. van Schalkwyk for their help with administration.
- Hettie Sieberhagen, for the language editing of this dissertation.
- Finally and most importantly, my parents and family, for supporting me in whatever it is I do, big or small.

Johan van Amstel Joubert

Centre for Space Research, North-West University